POLITECNICO
MILANO 1863

SCUOLA DI INGEGNERIA INDUSTRIALE
E DELL'INFORMAZIONE

Eclipse-Free Station-Keeping for Quasi-Halo Orbits with Application to the LUMIO Mission

Tesi di Laurea Magistrale in
Space Engineering - Ingegneria Spaziale

Author: **Giovanni Dalone**

Student ID: 252526
Advisor: Dr. Carmine Giordano
Co-advisors: Prof. Francesco Topputo, Alessandro Martinelli
Academic Year: 2025-26

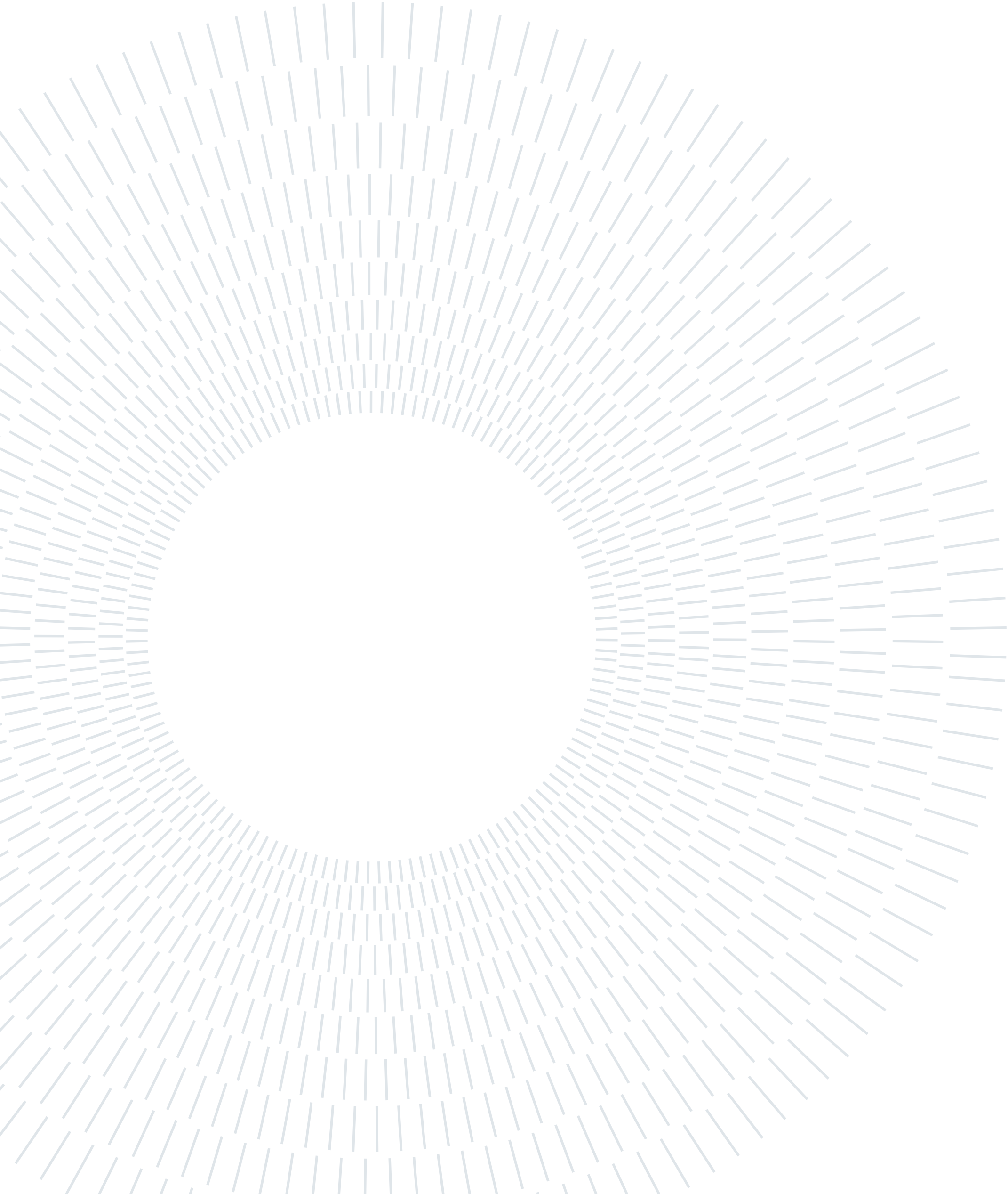

"Your mind is limitless.

You are worth more than you could believe.

All you have to do is dream... and all you have to do is want to fulfill that dream, and have the strength to fulfill that dream."

— Jahseh Onfroy a.k.a. XXXTENTACION

Abstract

CubeSats are increasingly extending their applicability from low-Earth orbit to more challenging cislunar and deep-space missions. In this context, eclipse events represent a critical operational constraint, particularly for those spacecrafts whose electrical and propulsion resources are limited. For missions operating on quasi-periodic orbits at the libration points of the Earth-Moon system, the eclipse events are highly sensitive to the orbit injection epoch and may impact mission feasibility because of their length.

This thesis investigates how active eclipse avoidance can be integrated into station-keeping strategies for Quasi-Halo orbits, maintaining robustness and assessing the propellant expenditure. The LUMIO Mission, a 12U CubeSat developed for lunar meteoroid impact observations, is adopted as test case.

A constraint-based analytical framework is developed to actively mitigate eclipse events without relying on global optimization procedures. Eclipse avoidance and recovery maneuvers are formulated as linearized control problems and are solved using Karush-Kuhn-Tucker conditions, yielding computational efficient closed-form solutions.

The eclipse avoidance constraint is formulated by the means of the continuous and differentiable formulated shadow function, which quantifies the spacecraft proximity to the eclipse regions generated by Earth and Moon. To manage the deviations introduced by the eclipse avoidance, a recovery strategy is formulated based on a linearity tube constraint, which ensures the validity of subsequent station-keeping maneuvers under linearized dynamics. The complete strategy is applied to multiple Quasi-Halo reference trajectories, and its performance is assessed through high-fidelity numerical simulations.

While the results demonstrate the effectiveness and robustness of the methodology, the associated cost in terms of ΔV is shown to be significant for the LUMIO Mission in several cases, highlighting the conservative character of the strategy and the stringent nature of the enforced constraints.

Keywords: Eclipse-Avoidance · LUMIO · Station-Keeping · Quasi-Halo Orbit · Cislunar CubeSat Mission · Karush-Kuhn-Tucker

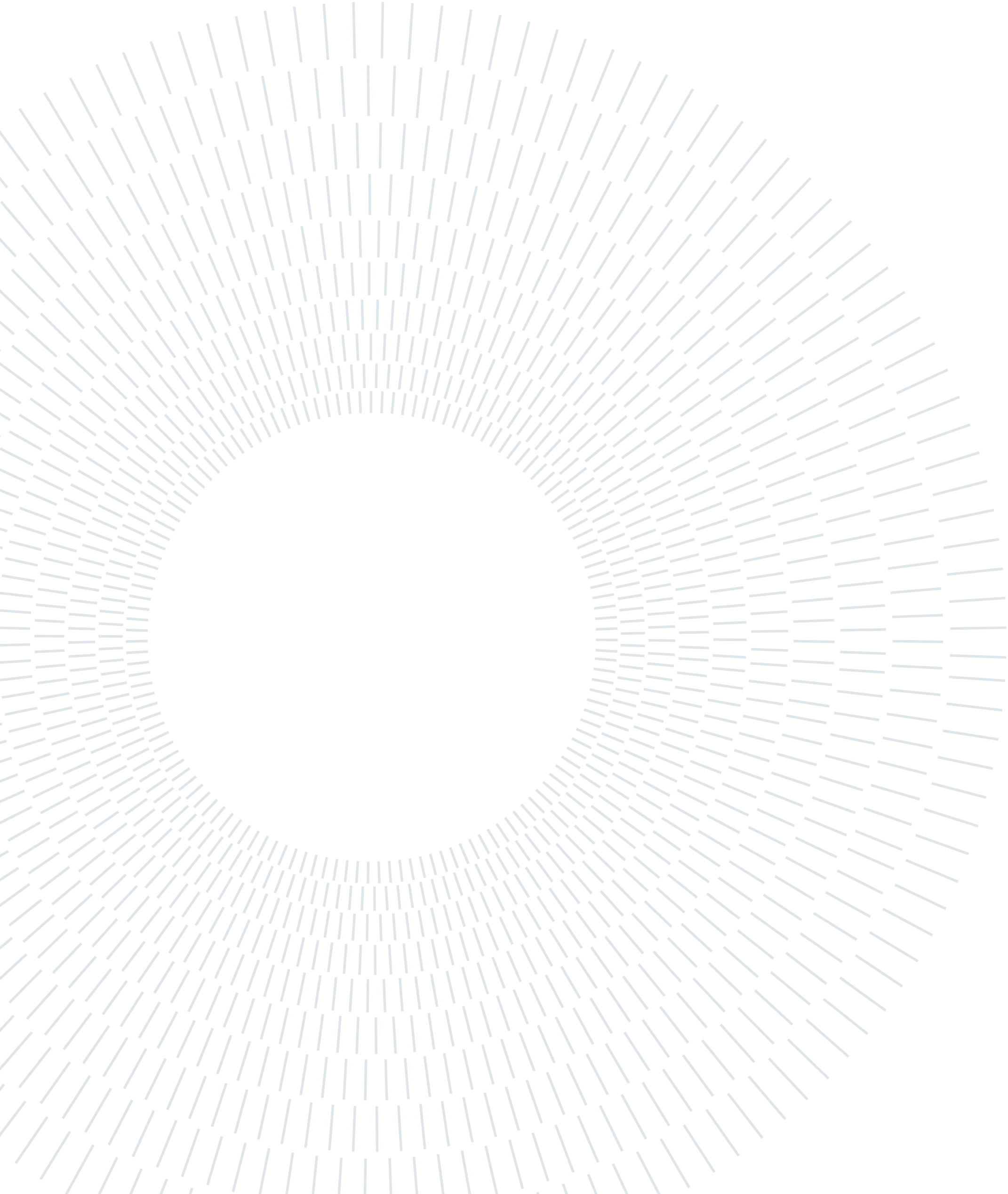

Sommario

I CubeSat stanno progressivamente estendendo il proprio ambito applicativo dalle basse orbite terrestri alle missioni cislunari e di spazio profondo, caratterizzate da condizioni operative più complesse. In questo contesto, gli eventi di eclissi rappresentano un vincolo operativo critico, soprattutto per satelliti con risorse elettriche e propulsive limitate. Per missioni su orbite quasi-periodiche in prossimità dei punti Lagrangiani del sistema Terra–Luna, la presenza e la durata delle eclissi risultano fortemente sensibili all'epoca di iniezione orbitale, incidendo in modo significativo sulla fattibilità della missione.

Questa tesi analizza l'integrazione di strategie di evitamento attivo delle eclissi nel mantenimento d'orbita per orbite Quasi-Halo, valutandone la robustezza del controllo e l'impatto in termini di consumo di propellente. La missione LUMIO, un CubeSat 12U dedicato all'osservazione degli impatti meteoritici lunari, è adottata come caso di studio.

Viene sviluppata una struttura analitica basata su vincoli per la mitigazione attiva delle eclissi, senza ricorrere a procedure di ottimizzazione globale. Le manovre di evitamento e recupero sono formulate come problemi di controllo linearizzati e risolte mediante le condizioni di Karush–Kuhn–Tucker, ottenendo soluzioni in forma chiusa computazionalmente efficienti.

Il vincolo di evitamento è modellato tramite una funzione d'ombra continua e differenziabile, che misura la prossimità del satellite alle regioni di eclissi generate da Terra e Luna. Le deviazioni introdotte dalle manovre di evitamento sono gestite mediante una strategia di recupero basata su un vincolo di tubo di linearità, che garantisce la validità della dinamica linearizzata e di conseguenza delle successive manovre di mantenimento d'orbita. La metodologia è applicata a diverse traiettorie di riferimento Quasi-Halo e valutata tramite simulazioni numeriche ad alta fedeltà.

I risultati mostrano l'efficacia e la robustezza dell'approccio proposto; tuttavia, il costo in termini di ΔV risulta significativo per la missione LUMIO in diversi scenari, evidenziando il carattere conservativo della strategia e la natura stringente dei vincoli adottati.

Parole chiave: Evitamento delle eclissi · LUMIO · Mantenimento d'orbita · Orbita Quasi-Halo · Missione CubeSat cislunare · Karush-Kuhn-Tucker

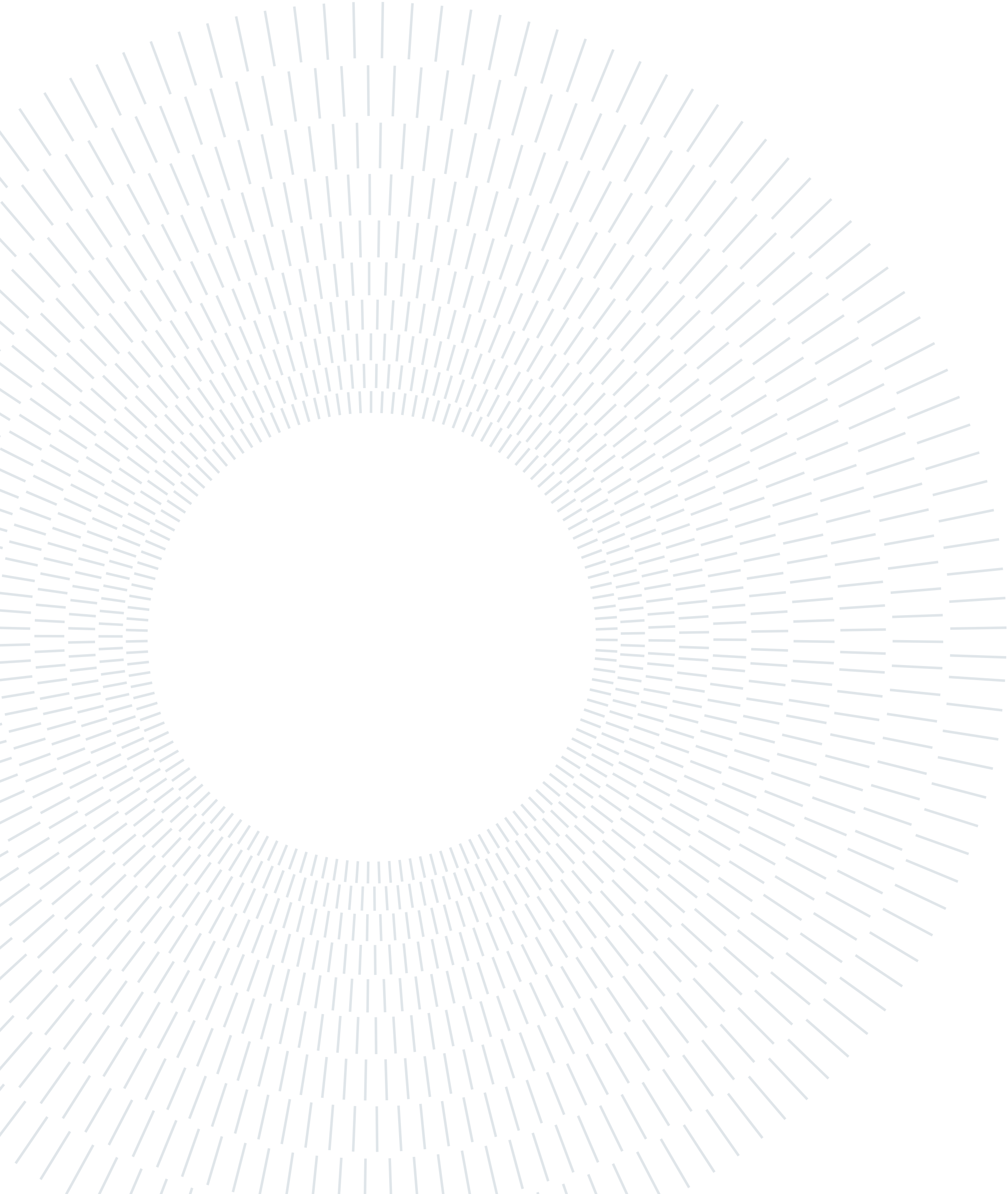

Contents

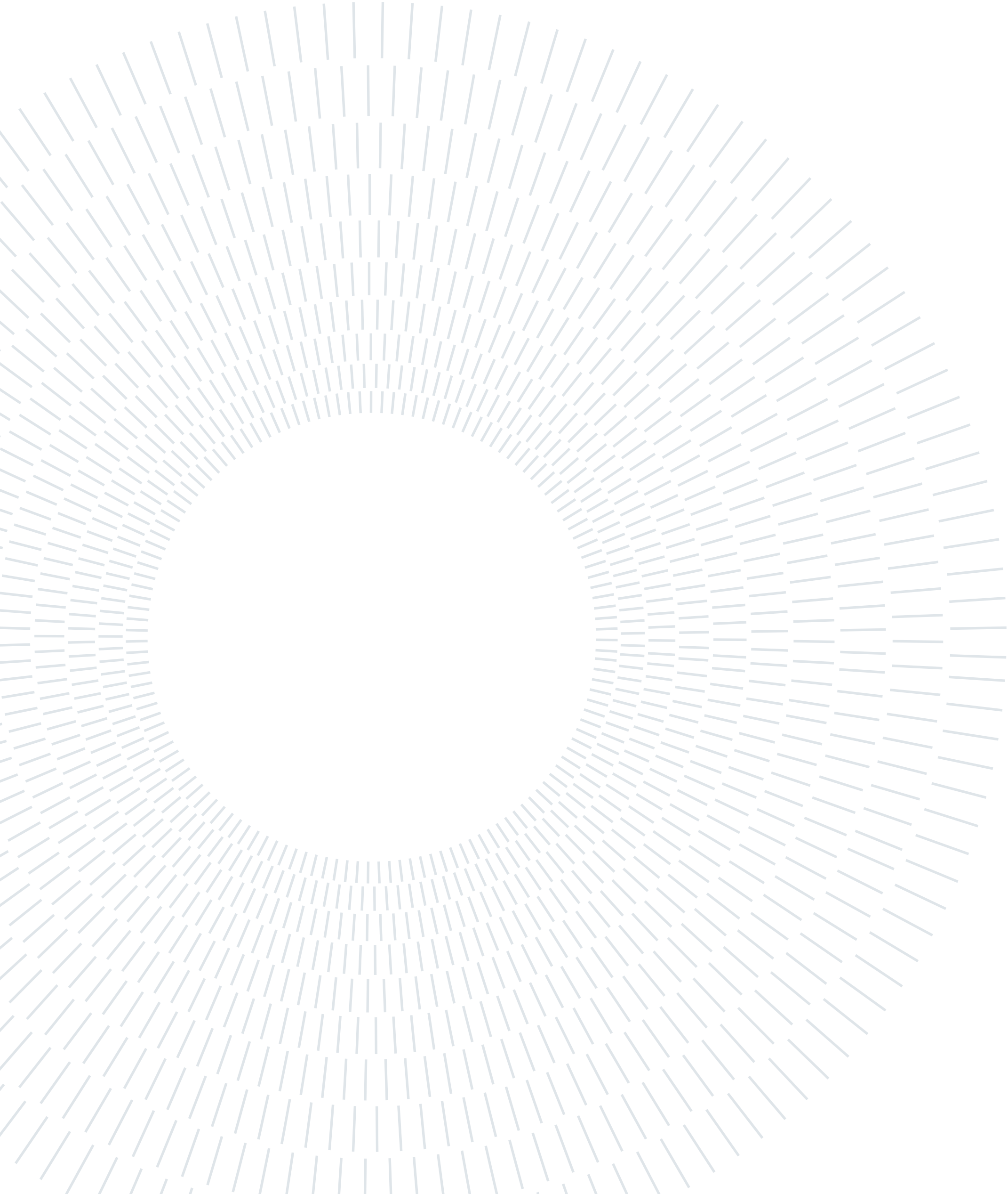

List of Figures

List of Tables

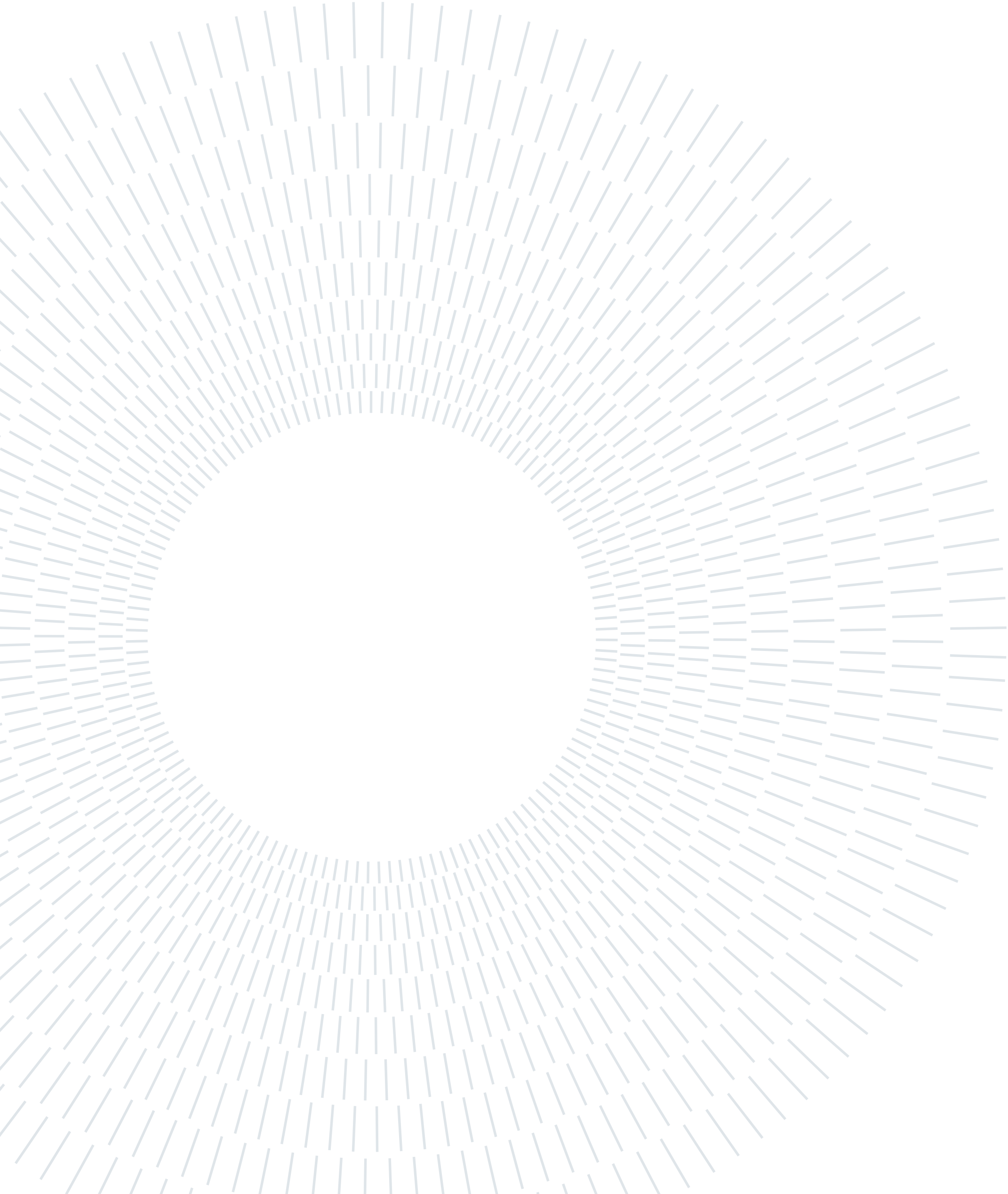

List of Acronyms

BCP	Bicircular Four-Body Problem
CCP	Concentric Circular Four-Body Problem
CRTBP	Circular Restricted Three Body Problem
DRO	Distant Retrograde Orbit
DSM	Deep Space Maneuver
ECSER	Earth-Centered Sun–Earth Rotating
EMB	Earth–Moon Barycenter
ERTBP	Elliptic Restricted Three Body Problem
HIM	Halo Injection Maneuver
KKT	Karush–Kuhn–Tucker
LEO	Low Earth Orbit
LQR	Linear Quadratic Regulator
LUMIO	Lunar Meteoroid Impacts Observer
MCSMR	Moon-Centered Sun–Moon Rotating
NLP	Non-Linear Programming
NRHO	Near Rectilinear Halo Orbit
OD	Orbit Determination
OI	Orbit Injection

RPRnBP	Roto-Pulsating Restricted n-Body Problem
S/C	Spacecraft
S/K	Station-Keeping
SPICE	Spacecraft Planet Instrument C-matrix Events
SRP	Solar Radiation Pressure
SSB	Solar System Barycenter
STM	State Transition Matrix
TAT	Turn-Around Time
TLI	Trans-Lunar Injection
TPA	Target Point Approach
TPBVP	Two-Point Boundary Value Problem
WSB	Weak Stability Boundary

1 | Introduction

CubeSats, in recent years, have emerged as a versatile and cost-effective class of spacecrafts, enabling access to space for commercial, technological and scientific missions that would otherwise be constrained by the costs and complexities of traditional satellites. They are characterized by a standard modular architecture (one unit corresponds to $10 \times 10 \times 10$ cm) which allows rapid development cycles, increased launch opportunities as secondary payloads and a high degree of scalability in mission design. Modern CubeSats are increasingly capable of accomplishing sophisticated mission objectives. Owing to the rapid evolution of miniaturized avionics, propulsion units, and communication systems, these platforms can now support navigation, communication, and scientific observation tasks even in complex dynamical environments beyond Low Earth Orbit (LEO). Representative examples include NASA's MarCO mission [40], which demonstrated interplanetary cruise and deep-space communication capabilities during the InSight Mars landing, and CAPSTONE [8], which successfully validated navigation and operations in the cislunar environment.

Operating CubeSats in these conditions introduces challenges that are significantly more demanding than those encountered in LEO. First, the intrinsic size limitations of CubeSat platforms restrict the available surface area for solar arrays and the volume allocated to onboard batteries, thus constraining the overall power budget and directly affecting other subsystems such as communications, attitude control, and payload operations. In particular, communication links require high transmission power and sufficiently large antenna systems to maintain reliable connectivity with Earth-based ground stations over vast distances, further stressing an already limited energy availability. Moreover, deep-space missions typically demand a non-negligible expenditure of propellant for trajectory corrections, orbit insertion, and long-term maintenance.

Concerning the cislunar environment, a further critical aspect from a resource perspective is represented by prolonged eclipse periods generated by the primary bodies. Depending on launch conditions and injection epochs, the spacecraft may experience shadow events that vary in number, duration, and depth, potentially exceeding the sustainable discharge capability of the onboard batteries and thereby threatening mission continuity.

In this framework, Halo orbits around the collinear libration points of the Earth–Moon system have gained particular relevance for operational missions. These trajectories provide advantageous geometrical configurations, including continuous visibility of the lunar far side and favorable communication conditions with Earth.
However, such trajectories are intrinsically unstable due to the underlying multi-body gravitational dynamics. Small deviations from the nominal solution grow over time, making active control indispensable to maintain the spacecraft within a prescribed neighborhood of the reference orbit. This operational activity, commonly referred to as Station-Keeping (S/K), consists of periodic corrective maneuvers designed to counteract the natural divergence of the trajectory. Since S/K maneuvers inherently modify the spacecraft's state along the orbit, they provide a mechanism to locally reshape the trajectory: in this perspective, corrective actions that are primarily intended to suppress dynamical instability may also be exploited to influence geometrical properties of the orbit, such as its relative configuration with respect to the shadow regions generated by the primary bodies. Consequently, station-keeping does not represent solely a stabilization tool, but may become an operational lever through which eclipse events can be mitigated.

1.1. Motivations

The coexistence of geometric shadow constraints and control requirements gives rise to an operational problem that cannot be addressed by treating trajectory design and guidance strategies as independent tasks. In realistic mission scenarios, initial conditions are often dictated by external constraints, limiting the possibility of selecting injection epochs that naturally avoid unfavorable configurations. As a result, mitigation strategies may operate within the existing dynamical framework rather than relying solely on a priori design choices. This context motivates the development of correction methodologies capable of embedding additional operational constraints directly into the maneuver design process. The objective is not merely to preserve the nominal motion, but to shape corrective actions in a way that accounts for mission-level requirements while maintaining computational tractability and deterministic behavior.

1.1.1. Research Question

Given the motivations, the objective of this work is to define a general methodology capable of diminishing the length of the most critical eclipse events at a level allowed by the power constraints while still ensuring compliance with the station-keeping requirements. A key advantage of the proposed approach lies in its ability to address the non-arbitrary nature of the initial orbital epoch. On the other hand, relying on an active eclipse avoidance logic, this approach inevitably leads to an increased maneuver scheduling complexity and a higher ΔV expenditure.

The research question at the basis of this thesis is:

Research Question:

To what extent can eclipse avoidance constraints be integrated into station-keeping strategies for Quasi-Halo orbits to improve robustness and operational feasibility, while minimizing the impact on the ΔV *budget?*

1.2. Case Study: LUMIO

The Lunar Meteoroid Impacts Observer (LUMIO)[1] spacecraft is a 12U-XL CubeSat mission of the European Space Agency (ESA) led by the DART Group at Politecnico di Milano and part of the ESA GSTP (General Support Technology Programme)[2]. The mission objective is to monitor the hidden face of the Moon in order to detect and characterize the flashes produced by the meteoroid impact on the surface. Complementing Earth-based observations, it helps to improve the knowledge of the Lunar Meteoroid Environment and contributes to Lunar Situational Awareness.

Figure 1.1: LUMIO CubeSat 12U-XL platform [59].

---

[1] Politecnico di Milano – LUMIO mission page, accessed 11th January 2026

[2] ESA – LUMIO mission page, accessed 11th January 2026

The satellite is designed to be launched as a piggy-back payload on a launch vehicle carrying a primary spacecraft injected onto a Weak Stability Boundary (WSB) trajectory. As a consequence, the injection conditions of LUMIO will coincide with those of the main passenger. After a transfer of several months it will reach the Moon and will operate on a Quasi-Halo orbit around the Lagrangian point L_2 of the Earth–Moon system.

In the present work, LUMIO is selected as the representative mission scenario on which the proposed methodology is formulated, implemented, and assessed.

1.3. State of the Art

Among the simplest models capable of capturing the features of multi-body gravitational dynamics, the Circular Restricted Three Body Problem (CRTBP) has played a fundamental role in the history of astrodynamics. Since the eighteenth century the CRTBP has been investigated by some of the world's most accomplished mathematicians and astronomers such as Newton, Euler and Lagrange, which demonstrated the existence of five equilibrium points, the so called libration points [19, 43]. A great contribution was carried out by Carl Gustav Jacob Jacobi, who introduced an integral of the motion in the rotating frame, the Jacobi constant [38]. One particular use of the constant was exploited by George William Hill with his work on zero-velocity curves [34]. Following these contributions, some of the most influential work on the Three-Body Problem originates with Henri Poincaré in the late 1800s [48] which was the basis for further analysis by George Darwin, whose paper in 1897 was the first to include a systematic, computational search for periodic orbits [13]. A detailed analysis and summary of the CRTBP is carried out by Szebehely in his book *Theory of Orbits* [56].

Since the late 1970s, bounded orbit at libration points have gained interest because of the practical applications that they offer. As a consequence of the unstable dynamics, effective methods of station-keeping became of primary importance to keep a spacecraft within the vicinity of libration points. The first contributions were done by Breakwell [5, 6] and Farquahr [20, 26], which dedicated their works to the ISEE-3 mission. A few surveys related to the station-keeping problem such as Gordon [32] and Shirobokov [51] compare the most relevant techniques that can be divided in two families:

- The first category comprises methods that explicitly exploit the underlying three-body dynamical properties, primarily through the application of Floquet theory;
- The second category consists of advanced control-theory techniques, specifically adapted to the station-keeping problem.

In both families a further division can be done in continuous and impulsive control: the first one uses small, continuously applied forces to regulate the trajectory, whereas the second one models maneuvers as instantaneous velocity changes applied at discrete times. For the purposes of this thesis (CubeSats orbiting L_2 point in Quasi-Halo orbits) only impulsive control is appropriate.

Regarding the first category, the Floquet Mode Approach represents one of the most relevant methods. It was originally introduced in the works of Simó et al. [52, 53], Kogan [41], and Wiesel and Shelton [63], and is based on the identification of unstable directions in phase space along a periodic orbit. This information can be exploited to compute impulsive corrections that locally suppress the growth of instability in a linear approximation of the dynamics. However, as shown in [68], this technique alone is not sufficient to ensure station-keeping over the entire expected mission lifetime of CubeSats in Quasi-Halo trajectories. This limitation is mainly due to the fact that the computation of the State Transition Matrix (STM) over long time spans along periodic orbits leads to significant numerical errors.
With regard to the second category, targeting strategies are among the most widely used and reliable approaches, and are primarily based on the so-called Target Point Approach (TPA). First introduced in the work of Howell [35, 36] in the 90s, it is a method based on the computation of correction maneuvers by the minimization of a weighted cost function defined in terms of $\boldsymbol{\Delta v}$, position and velocity deviations from the nominal trajectory.It is a linearized, computationally efficient, STM-based technique that has been successfully implemented and tested in various mission contexts. Among its applications, it has also been adopted as the baseline station-keeping strategy for the LUMIO mission [10, 15].

However, it is less common in the literature to find works addressing eclipse-free station-keeping. Eclipses have become a relevant issue in recent years, as the operational range of CubeSats has progressively expanded toward the cislunar environment. To this aim, the majority of existing studies adopt mission-analysis approaches that ensure trajectories naturally free from eclipse events; this category can be labeled as passive avoidance. The most significant contributions are due to Wishnek et al. [64], who implemented an epoch-based grid search to identify suitable launch or injection epochs, ensuring eclipse-free operation. Davis et al. [14] exploit the resonant properties of NRHO, combined with appropriate epoch selection, to avoid eclipses. Another approach is investigated in [11], where naturally eclipse-free operational Quasi-Halo orbits are identified through high-fidelity refinements of baseline trajectories at different injection epochs.

The work of Yang Sun et al. [49] instead addresses active avoidance, proposing a three-burn strategy for Distant Retrograde Orbit (DRO), based on time- and cost-optimized maneuvers designed to avoid the umbra generated by the primary bodies.

In this thesis, passive avoidance methods are not considered, as they rely exclusively on mission analysis and trajectory design. An active avoidance method is therefore formulated and tested on the LUMIO mission.

1.4. Workflow

In this section, the workflow used to formulate the problem and achieve the results presented in the following chapters is concisely outlined.
The work starts from the reference Halo orbit of LUMIO with Jacobi constant $C_j = 3.09$ [61], obtained with a differential correction scheme, a common technique employed for periodic orbits in the context of CRTBP. Such procedures are well documented in the literature [44] and are not reported here, as they are outside the scope of the present work. This baseline Halo orbit in CRTBP is subsequently used as an initial guess for a high-fidelity refinement, following the methodology proposed by D. A. Dei Tos and F. Topputo [16, 17]. The procedure yields a reference trajectory in the Roto-Pulsating Restricted n-Body Problem (RPRnBP) adimensional frame, which extends the classical three-body formulation by accounting for the non-circular motion of the primaries and incorporating additional perturbations, such as the gravitational influence of other celestial bodies and the effects of Solar Radiation Pressure (SRP).
Then, a computationally efficient way to detect eclipses is needed. In particular, together with the implementation of the Conical Shadow Method [54, 57], a transformation of the trajectory into two convenient reference frames is employed: the ECSER and the MCSMR. In these frames, the umbra and penumbra cones generated by the primaries are fixed along the positive x-axis, allowing eclipse periods to be easily identified. This method is validated through the comparison of its results with the ones provided by the SPICE[3] toolkit, the NASA's standard information system providing core data (ephemeris, orientation, shape) and software to calculate observation geometry for space missions.
The Target Point Approach, as a nominal station-keeping technique, is implemented and tested. On this basis, a closed-form avoidance methodology is sought. Solutions that require optimization procedures are not allowed, as computational times and convergence problems, in a realistic mission control scenario, could be critical and dangerous for the mission accomplishment.

---

[3] `https://naif.jpl.nasa.gov/naif/toolkit.html`

The core problem is approached by adopting an active avoidance strategy formulated as a constrained linearized optimization problem, solved using Karush–Kuhn–Tucker (KKT) conditions. Two linearized constraints are formulated to avoid the umbra-penumbra region, and to come back close to the reference orbit. An explicit active-set implementation of the KKT conditions is used to select the optimal solution ensuring the constraints satisfaction. This approach guarantees deterministic and computationally efficient solutions within the validity region of the linear model.
Eventually, the method's cost in terms of ΔV is addressed and discussed.

1.5. Thesis outline

This work is organized in different chapters, here presented:

- **Chapter 1: Introduction.** Provides an overview of the state of the art for the station-keeping problem in cislunar environment. After the statement of the research objective, the case study of this work, LUMIO, is briefly introduced and the workflow is presented.
- **Chapter 2: Dynamical Models.** Aims to give a concise yet precise description of the theoretical astrodynamical models and the laws that are implemented in the algorithm: from the CRTBP to the RPRnBP. Lastly, the procedure to obtain Quasi-Halo reference trajectories in high-fidelity dynamics is presented.
- **Chapter 3: Station-Keeping Techniques.** Presents and describe exhaustively the impulsive strategies that are relevant in the context of CubeSats, and gives a review of the already existing eclipse-avoidance strategies.
- **Chapter 4: LUMIO Mission.** Introduces details and mission constraints that drive the formulation of the problem such as the eclipse avoidance one. It is presented the method for shadow modeling.
- **Chapter 5: Methodology.** This is the core of this research. The KKT approach is formalized together with the definition of the eclipse constraint and the linearity tube constraint. This chapter includes the maneuver scheduling assumptions, giving a comprehensive outline of the method.
- **Chapter 6: Results.** The numerical outcomes are presented and discussed. Considerations on LUMIO Mission together with general ones are carried out.
- **Chapter 7: Conclusions.** A summary of the work and some final thoughts are given. Future ways to improve the methodology close the thesis' contents.

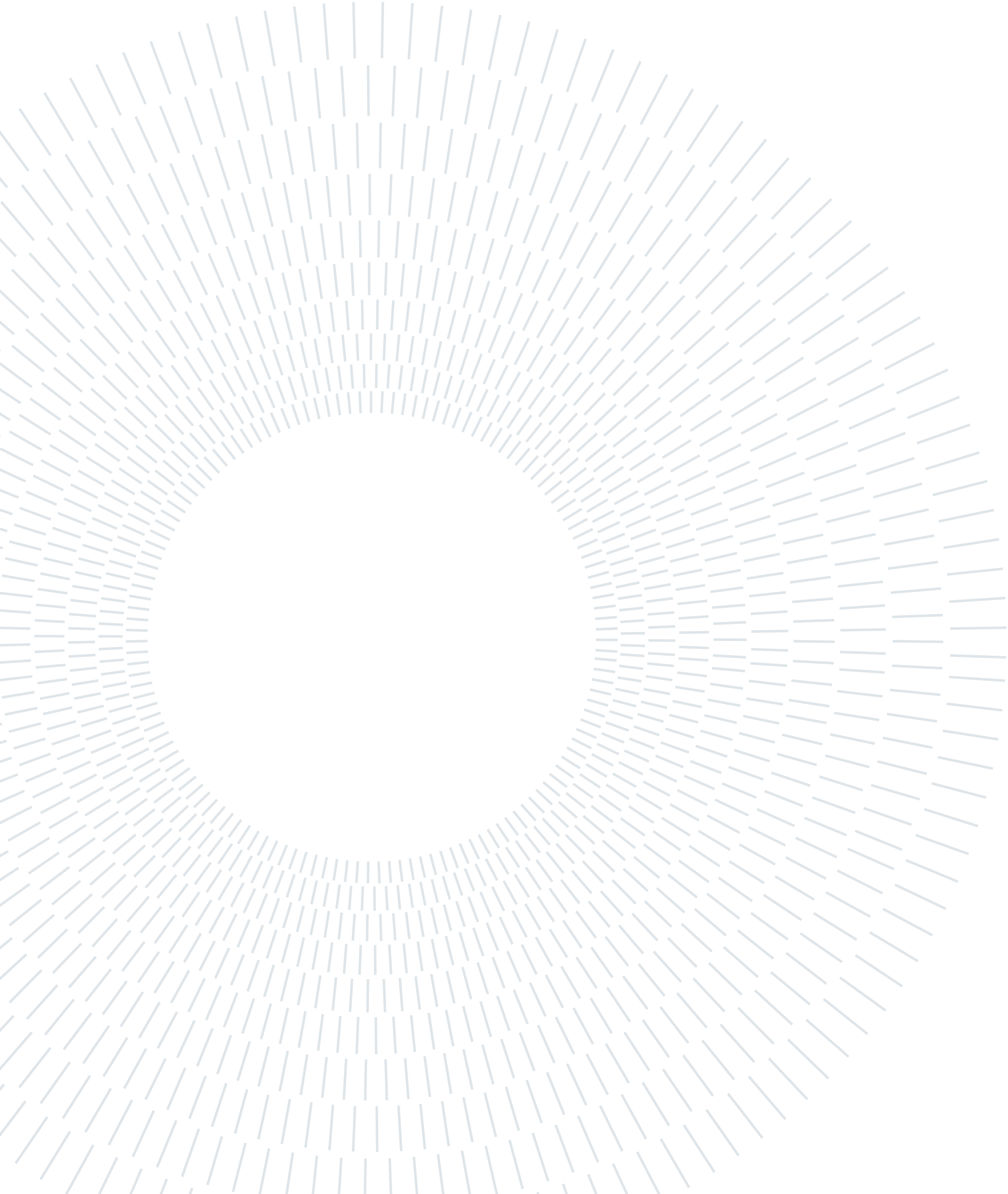

2 | Dynamical Models

The motion of any body in a gravitational field is governed by the laws of classical mechanics, as stated in the Newton's universal law of gravitation and the consequent equations of motion. With m representing the mass, $\boldsymbol{r}$ the position vector, and G the universal gravitation constant:

$$m_i \ddot{\boldsymbol{r}}_i = \boldsymbol{F}_{ji}, \qquad \text{with} \qquad \boldsymbol{F}_{ji} = -G \sum_{\substack{j=1 \\ j \neq i}}^{n} \frac{m_i m_j}{r_{ji}^3} \boldsymbol{r}_{ji}, \qquad i = 1, \ldots, n. \tag{2.1}$$

When multiple celestial bodies interact between each other, the resulting dynamics can become highly complex and, in general, not analytically tractable. To enable a meaningful analysis of spacecraft motion in multi-body environments, simplified dynamical models are commonly adopted. In this chapter, the dynamical framework adopted throughout this work is introduced. Particular attention is first devoted to the CRTBP, within which several concepts of paramount importance are defined. Subsequently, the need for a high-fidelity representation of the real motion leads to the introduction of the RPRnBP.

2.1. The Circular Restricted Three Body Problem

The problem is defined as follows: two bodies revolve around their center of mass in circular orbits under the influence of their mutual gravitational attraction and a third body (attracted by the previous two, but not influencing their motion, which remains Keplerian around their barycenter) moves in the plane defined by their relative motion; the two revolving bodies are called primaries and their mass is much bigger than the third one: m_1, $m_2 \gg m_3$. The restricted problem of three bodies is to describe the motion of the third body. Despite its simplifying hypotheses, the CRTBP provides a convenient framework for studying equilibrium points, periodic orbits, and invariant manifolds which are detailed in the next sections. Throughout this work, distances are expressed in nondimensional form by normalizing them with the characteristic distance unit DU. In the Earth–Moon system, this unit corresponds to the mean Earth–Moon distance, equal to $DU = 3.84405 \times 10^5$ km.

2.1.1. Equations of Motion

The equations of motion can be written by adopting a uniformly rotating reference frame with origin at the barycenter of the system and angular velocity equal to that of the primaries. The geometry can be visualized in Fig. 2.1.

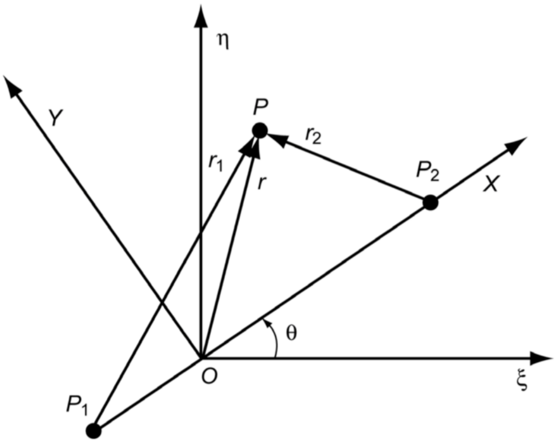

Figure 2.1: Geometry of the Circular Restricted Three Body Problem [1].

In this frame, the primaries remain fixed along the x-axis, and the dynamics of the third body can be expressed as a set of second-order differential equations that include gravitational, Coriolis and centrifugal terms, respectively, in the following equation:

$$\frac{d^2\mathbf{r}}{dt^2} = -G\left(\frac{m_1}{r_1^3}\mathbf{r_1} + \frac{m_2}{r_2^3}\mathbf{r_2}\right) - 2\boldsymbol{\omega} \times \frac{d\mathbf{r}}{dt} - \boldsymbol{\omega} \times (\boldsymbol{\omega} \times \mathbf{r}) \tag{2.2}$$

Introducing the non-dimensional mass parameter μ and the effective scalar potential function U:

$$\mu = \frac{m_2}{m_1 + m_2}, \qquad \text{with} \quad m_1 > m_2 \tag{2.3}$$

$$U = \frac{1}{2}(x^2 + y^2) + \frac{1-\mu}{r_1} + \frac{\mu}{r_2}, \tag{2.4}$$

the equations of motion can be re-written as a function of these terms. In particular, since:

$$\begin{cases} \dfrac{\partial U}{\partial x} = x - \dfrac{1-\mu}{r_1^3}(\mu + x) + \dfrac{\mu}{r_2^3}(1 - \mu - x) \\ \dfrac{\partial U}{\partial y} = y - \dfrac{1-\mu}{r_1^3}y - \dfrac{\mu}{r_2^3}y \\ \dfrac{\partial U}{\partial z} = -\dfrac{1-\mu}{r_1^3}z - \dfrac{\mu}{r_2^3}z \end{cases} \tag{2.5}$$

The normalized equations of motion are:

$$\ddot{x} - 2\dot{y} = \frac{\partial U}{\partial x}, \qquad \ddot{y} + 2\dot{x} = \frac{\partial U}{\partial y}, \qquad \ddot{z} = \frac{\partial U}{\partial z}. \tag{2.6}$$

The equations of motion written in this form admit a conserved quantity, known as the Jacobi integral, which constitutes the only known integral of motion of the CRTBP:

$$C_j = 2\Omega^{(3)} - (\dot{x}^2 + \dot{y}^2 + \dot{z}^2) \quad \text{with} \quad \Omega^{(3)} = U + \frac{1}{2}\mu(1-\mu), \tag{2.7}$$

where $\Omega^{(3)}$ is the 3-body pseudo potential function.

2.1.2. Definition of the libration Points

The CRTBP allows five equilibrium points where the gravitational and centrifugal forces balance out. For an equilibrium point $\boldsymbol{x}_{eq}$ the rate of change of the state must be null. Hence, from Eq. (2.6), the conditions for equilibrium are:

$$\begin{cases} \dot{x} = \dot{y} = \dot{z} = 0 \\ \dfrac{\partial U}{\partial x} = \dfrac{\partial U}{\partial y} = \dfrac{\partial U}{\partial z} = 0 \end{cases} \tag{2.8}$$

It follows directly that all libration points lie in the plane of motion of the primaries. The triangular equilibrium points, denoted L_4, L_5, are obtained by enforcing equal distances from the two primaries, which leads to two symmetric configurations forming equilateral triangles with them. The remaining equilibrium points, L_1, L_2, L_3, are collinear with the primaries and are determined by restricting the motion to the line connecting the two massive bodies and solving the corresponding one-dimensional equilibrium condition.

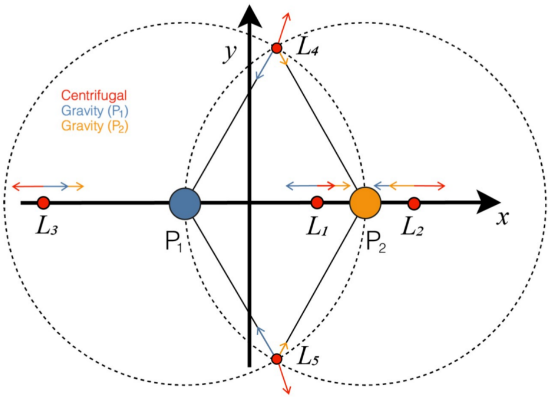

Figure 2.2: Libration points position [11].

	L_1	L_2	L_3	L_4	L_5
x	$+0.8369180073$	$+1.1556799131$	-1.0050624018	$+0.4878500000$	$+0.4878500000$
y	0	0	0	$+0.8660254038$	-0.8660254038

Table 2.1: Earth–Moon libration points' coordinates @ Earth-Moon Barycenter (EMB) centered adimensional rotating frame.

In the neighborhood of the libration points, the dynamics of the CRTBP admits several families of open, periodic and quasi-periodic orbits, whose existence is governed by the local stability properties of the equilibrium points.

2.1.3. Hill's Regions

Hill's regions provide a fundamental geometrical interpretation of the motion of a spacecraft in the CRTBP. For a given value of the Jacobi constant, the motion is restricted to specific regions of space, while other regions are dynamically forbidden. The boundaries of Hill's regions are defined by the so-called zero-velocity curves, which correspond to configurations where the kinetic energy of the particle vanishes: in the allowed regions the kinetic energy is positive while, in the forbidden ones, it is negative.
By varying the value of the Jacobi constant, the topology of Hill's regions changes, leading to the opening or closing of narrow passages near the collinear libration points.

For a given μ there exist five configurations of the Hill's regions, represented in Fig. 2.3. The five possible intervals of energy are [42]:

- **Case 1:** $E < E_1$. If the energy of the particle is below E_1, the spacecraft cannot move between the realms around m_1 and m_2.
- **Case 2:** $E_1 < E < E_2$. If the energy is just above E_1 a "bridge" opens up between the two realms, with L_1 being the "neck". The spacecraft is still not able to extend beyond infinity.
- **Case 3:** $E_2 < E < E_3$. This is the most significant case in the context of the thesis. The spacecraft can move between the vicinity of the bodies and the exterior realm through the L_2 neck.
- **Case 4:** $E_3 < E < -\frac{3}{2} = E_4 = E_5$. The spacecraft can directly go through the vicinity of m_1 to the exterior realm.
- **Case 5:** $-\frac{3}{2} < E$. The forbidden regions disappears: the spacecraft is free to move in the entire plane. This case is not represented in the following Fig. 2.3, since no Hill's regions would be present.

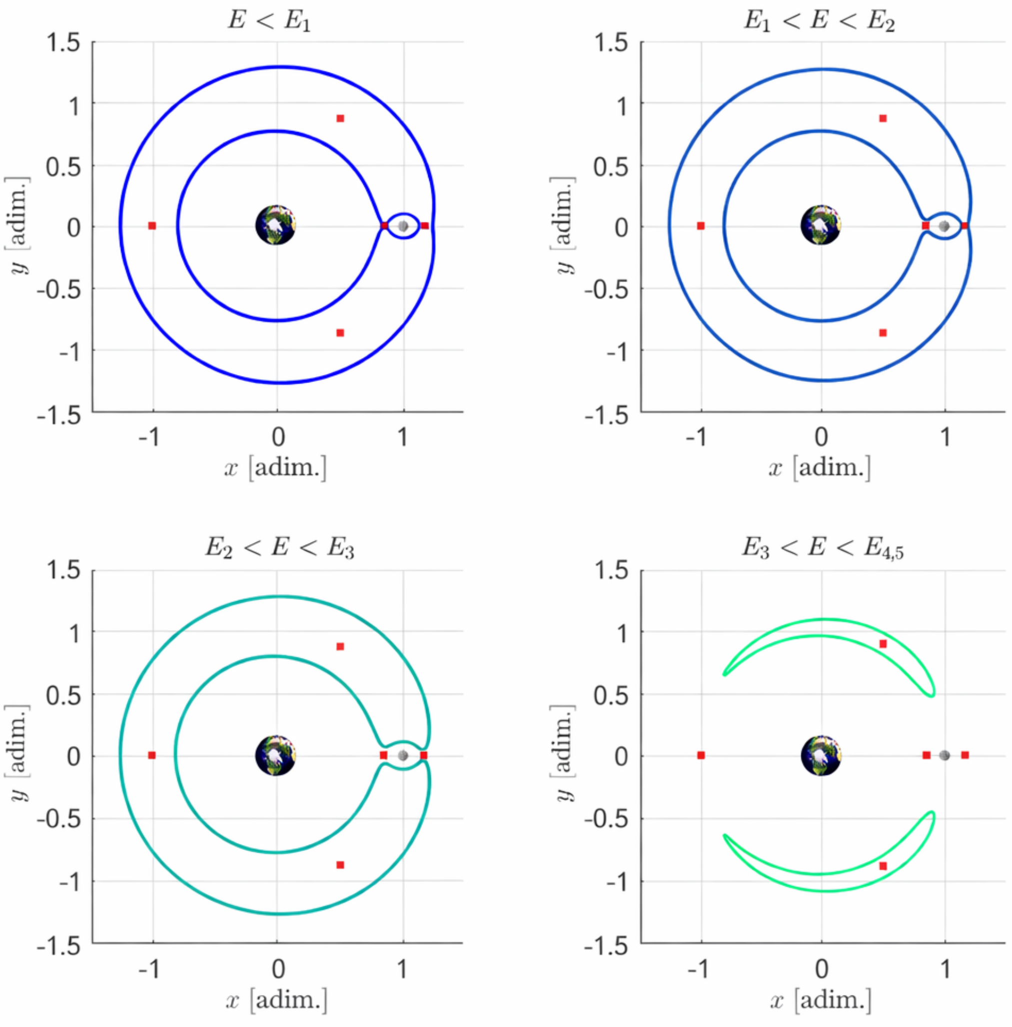

Figure 2.3: Hill's Regions @ EMB centered adimensional rotating frame. Inside the bounded contours the motion is forbidden. The red dots mark the position of libration points. Bodies not to scale.

The third region gains high value for the practical applications it offers, particularly because of the closed orbits that can be obtained by exploiting the peculiarities of the gravitational field near the L_1 and L_2 Lagrangian points. Modern applications are related to deep space observation missions, such as the James Webb Space Telescope [67], which is positioned near the L_2 point for optimal observational conditions, free from Earth's interference. Other key examples are the ESA's LISA[1] (Laser Interferometer Space Antenna) mission, the Gateway Mission [14] and LUMIO mission, which also will benefit of the L_1 and L_2 points.

---

[1] ESA – LISA mission page, accessed 11th January 2026

2.1.4. Motion and Stability

To describe the existing orbit families, the equations of motion of the CRTBP are linearized in the vicinity of the Lagrangian points. For the interested reader the full derivation of the linearized equations of motion is available at [1, 42, 56]. Through a first order Taylor expansion it is obtained:

$$\delta \dot{\boldsymbol{x}} = \boldsymbol{A} \delta \boldsymbol{x}, \qquad \boldsymbol{A} = \left(\frac{\partial \boldsymbol{f}}{\partial \boldsymbol{x}} \right)_{x=x_L} = \begin{pmatrix} \boldsymbol{0}_{3\times3} & \boldsymbol{I}_{3\times3} \\ U_{rr} & -2\boldsymbol{\Omega}_{3\times3} \end{pmatrix}_{x=x_L}, \tag{2.9}$$

where U_{rr} is the square matrix of the second-order partial derivatives of the effective potential U with respect to the position variables x, y, z, and $\boldsymbol{\Omega}_{3\times3}$ is the cross product matrix for the angular velocity of the rotating system $\boldsymbol{\omega} = (0, 0, 1)^T$:

$$\boldsymbol{\Omega}_{3\times3} = \begin{pmatrix} 0 & -1 & 0 \\ 1 & 0 & 0 \\ 0 & 0 & 0 \end{pmatrix} \tag{2.10}$$

It is then possible to study the eigenvalues of $\boldsymbol{A}$ and write the linearized equations of motion:

$$\begin{cases} \delta x(t) = A \cos(\omega_p t + \phi_1) + Ce^{\lambda t} + De^{-\lambda t}, \\ \delta y(t) = -k_2 \sin(\omega_p t + \phi_1) + k_1 \left(Ce^{\lambda t} - De^{-\lambda t} \right), \\ \delta z(t) = B \cos(\omega_v t + \phi_2). \end{cases} \tag{2.11}$$

Here k_1 and k_2 are constants depending on the system primaries, while A, B, C, D, ϕ_1 and ϕ_2 are the constants of integration determined by the initial conditions, and ω_p and ω_v are called the in-plane and the out-plane frequencies, respectively [51]. It follows that in the linear approximation, periodic trajectories exist around the collinear libration points in the xy-plane and along a line parallel to the z-axis, with corresponding frequencies ω_p and ω_v, respectively.

Depending on the parameters mentioned before, the motion near an equilibrium point can be [1, 11]:

- **Saddle Motion**: The motion of the spacecraft is hyperbolic. Depending on the asymptote direction, it can approach the libration point through the stable one or it can escape from it through the unstable one.
- **Lissajous orbits**: These open orbits oscillate in the out-plane direction with a different frequency with respect to the in-plane direction giving them the characteristic

of quasi-periodicity.

- **Halo orbits**: Are special Lissajous orbit which are closed loop with fixed geometry and size. They are characterized by the equal out-plane and in-plane period.
- **Lyapunov orbits**: These 2D orbits are a consequence of no out-plane oscillation of the Lissajous. The shape is a closed ellipse and they are present in all libration points.
- **Trojan orbits**: Exist only at L_4 and L_5 and are of particular interest when dealing with the asteroid belts.

Each solution of Eq. (2.9) can be written in the form:

$$\delta \boldsymbol{x}(t) = \boldsymbol{\Phi}(t_0, t)\delta \boldsymbol{x}(t_0), \tag{2.12}$$

where $\boldsymbol{\Phi}(t, t_0)$ is the STM as solution to the first-order variational equation:

$$\dot{\boldsymbol{\Phi}}(t_0, t) = \boldsymbol{A}(t)\boldsymbol{\Phi}(t_0, t), \qquad \text{with} \qquad \boldsymbol{\Phi}(t_0, t_0) = \boldsymbol{I}_{6\times 6}. \tag{2.13}$$

The STM is a linear operator that relates the initial state deviation vector, with respect to the theoretical reference trajectory, to the final state error vector. Its validity relies on the accuracy of the linear approximation, therefore, large deviations or long time spans may compromise its precision.

To study the local stability of a solution, the concept of monodromy matrix is introduced. From the Floquet theory [12, 51], the monodromy matrix is defined as:

$$\boldsymbol{M} = \boldsymbol{\Phi}(0, T), \qquad \text{where } T \text{ is the period of the orbit.} \tag{2.14}$$

For the stability analysis, the eigenvalues of $\boldsymbol{M}$, the so-called Floquet multipliers, are studied. The stability of the system can be determined by examining the magnitude of these eigenvalues. In the case of Halo orbits, object of study of this work, the eigenvalues can be grouped in the following configuration and geometrical meaning [42]:

- λ_1, λ_2 are real and inverse with respect to each other: $\lambda_1\lambda_2 = 1$, $\lambda_1 \gg 1$. They are associated with the hyperbolic character of the orbit and their related eigenvectors are a description of the unstable and stable direction of the variational flow. These are of primary importance when defining the stable and unstable manifolds for a

Halo orbit. The submatrix for these two eigenvalues is:

$$M_{(\lambda_1,\lambda_2)} = \begin{bmatrix} \lambda_1 & 0 \\ 0 & \lambda_2 \end{bmatrix}. \tag{2.15}$$

- The second eigenvalue pair $(\lambda_3, \lambda_4) = (1, 1)$ is linked to neutral variables. The first eigenvector corresponds to a shift in time (or phase) along the orbit, while the second eigenvector is associated with energy changes within the family of Halo orbits. The restricted monodromy matrix is:

$$M_{(\lambda_3,\lambda_4)} = \begin{bmatrix} 1 & \epsilon \\ 0 & 1 \end{bmatrix}. \tag{2.16}$$

- The third pair (λ_5, λ_6) is composed by two complex conjugated eigenvalues of unitary modulus. They are associated with the existence of quasi-periodic orbits. The restricted monodromy matrix is:

$$M_{(\lambda_5,\lambda_6)} = \begin{bmatrix} \cos\theta & -\sin\theta \\ \sin\theta & \cos\theta \end{bmatrix}. \tag{2.17}$$

Invariant manifolds are spatial structures that govern the motion of particles within a three-body system. They are closely linked to the periodic orbits around the system's equilibrium points, aiding in controlling the flow of trajectories between different regions of the phase space.

A first guess for the invariant manifolds computation can be performed exploiting the eigenvalues of the monodromy matrix. In particular, the eigenvector with eigenvalue grater than one (λ_1) is the unstable one, while the other (λ_2) is the stable one.
Let $\boldsymbol{y}^s(\boldsymbol{x}_0)$ be the normalized stable eigenvector and $\boldsymbol{y}^u(\boldsymbol{x}_0)$ the unstable one. It is then possible to obtain the manifolds by considering:

$$\boldsymbol{x}^s(\boldsymbol{x}_0) = \boldsymbol{x}_0 + \epsilon \boldsymbol{y}^s(\boldsymbol{x}_0), \tag{2.18}$$

$$\boldsymbol{x}^u(\boldsymbol{x}_0) = \boldsymbol{x}_0 + \epsilon \boldsymbol{y}^u(\boldsymbol{x}_0). \tag{2.19}$$

Here ϵ is a small displacement from $\boldsymbol{x}_0$ and its magnitude should be small enough to be within the validity of the linear approximation, yet not so small that the manifold triggering takes too long to begin. By integrating the unstable perturbed initial state forward and the stable one backward for a discretized number of points along the periodic orbit, the manifolds are obtained [42].

In conclusion, the local stability analysis, aided by the monodromy matrix, determines whether perturbations will grow or decay over time. Together, the manifolds regulate the transition of the particles from the interior and exterior realms. These manifolds can also be leveraged by mission designers to optimize transfers, combining their effects to efficiently reach specific regions with minimal fuel consumption.

In the following Fig. 2.4, a visual representation of them is given for the particular case of LUMIO, the test-bed for this work:

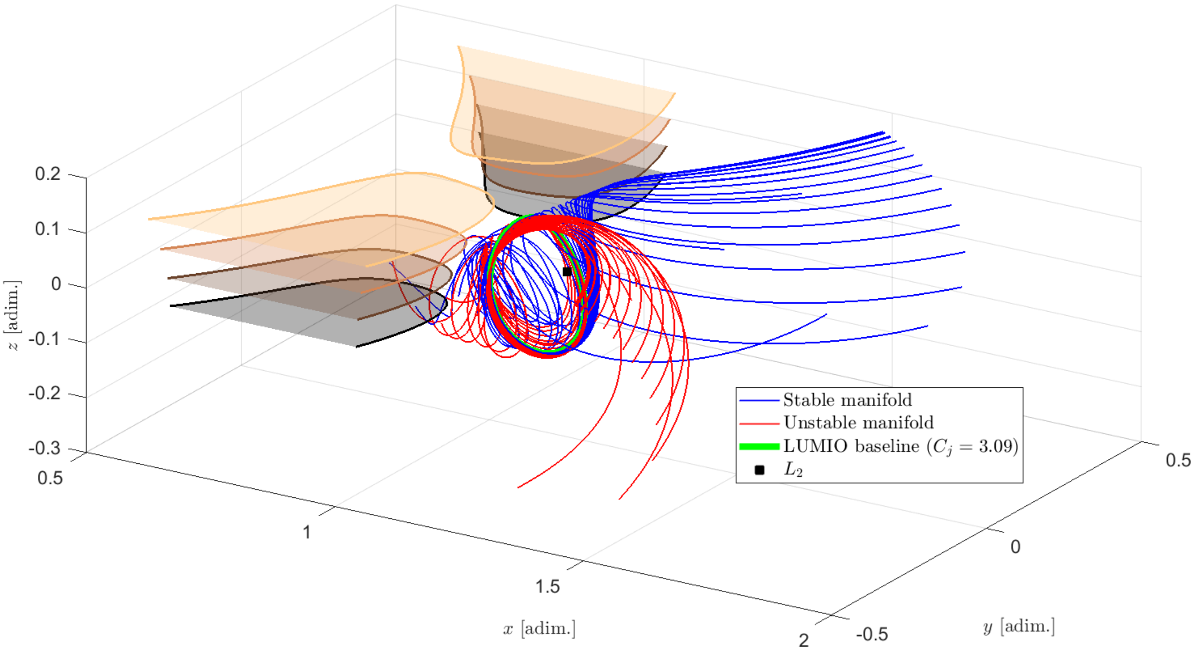

Figure 2.4: Invariant manifolds @ EMB centered adimensional rotating frame. The shaded areas represents the Hill's forbidden regions at different z values.

2.2. The High-Fidelity Roto-Pulsating Restricted n-Body Problem

When the three-body solutions are reproduced in more accurate gravitational models big deviations from the expected behavior are found. Employing a high-fidelity model during the design phase is then crucial to accurately capture the realistic behavior of the system. The model employed in this work is the Roto-Pulsating Restricted n-Body Problem (RPRnBP).

The equations of motion can be written as a perturbation of the CRTBP, as it considers additional dynamical influences, such as the gravitational attraction of all the other solar system bodies, and the SRP. Moreover, the motion of the two primaries is ephemerid-based, relaxing the circular assumption. The restricted assumption is retained, since the spacecraft mass is several orders of magnitude smaller and therefore does not influence the system dynamics [16]. In the following section, a hierarchical development of the astrodynamical models will be presented, culminating in the equations of motion for the most accurate model, the RPRnBP.

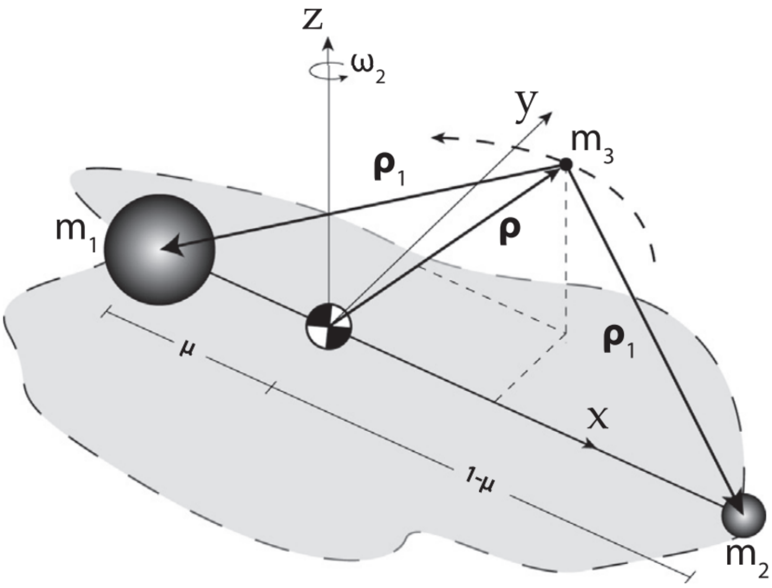

Figure 2.5: Geometry of the RPRnBP [16].

2.2.1. From the CRTBP to the RPRnBP

The CRTBP, being the lower level in the hierarchic ladder, is the ideal model to design unique solutions and to study the neighborhood dynamics of the collinear libration points, which possess properties that make them valuable candidates for practical applications.

Elliptic Restricted Three Body Problem

The next step in the hierarchy is the Elliptic Restricted Three Body Problem (ERTBP), in which the mutual motion of the two primaries is no longer circular but elliptic.
By introducing the true anomaly f as the new independent variable, which plays the role of time, the elliptic problem becomes non-autonomous. The equations of motion become:

$$x'' - 2y' = \omega_{/x}, \qquad y'' + 2x' = \omega_{/y}, \qquad z'' = \omega_z. \tag{2.20}$$

$$\omega(x,y,z,f) = \frac{\Omega^{(3)} - \frac{1}{2}z^2 e_p \cos(f)}{1 + e_p \cos(f)}, \tag{2.21}$$

where e_p is the the eccentricity of the ellipses.

Restricted Four Body Model

Including an additional massive body in the system the dynamical behavior and the geometry becomes more complex. Two main models are available and they differs on the perspective with which the equations are written. In particular:

- **Bicircular Four-Body Problem (BCP)**: A system of two bodies revolves about a massive celestial body. A representation is given in Fig. 2.6, left.
- **Concentric Circular Four-Body Problem (CCP)**: Two bodies revolve in a similar way around the more massive primary in a concentric model. A representation is given in Fig. 2.6, right.

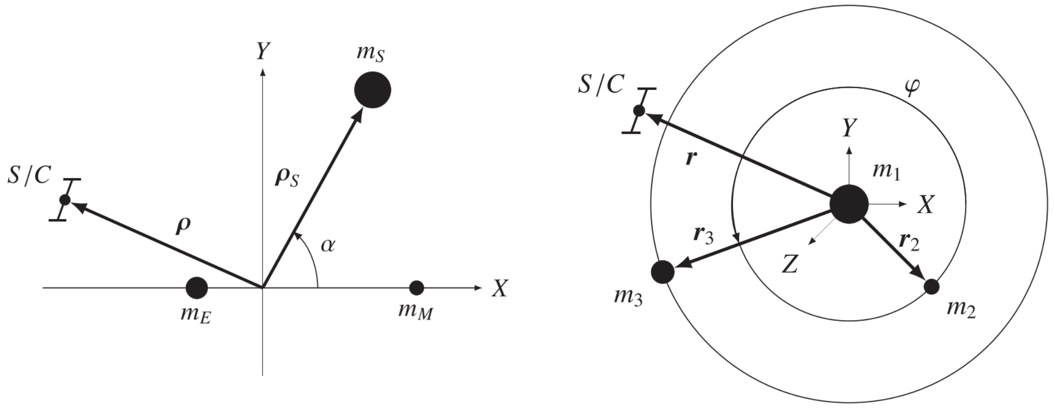

Figure 2.6: Geometries of the BCP (left) and CCP (right) [16].

The **BCP** assumes circular motion of the two primaries about their barycenter, which moves in a circular fashion around the center of mass of the whole system. Moreover, all bodies lie on the same plane [16].

For the Earth-Moon system, without losing generality, the same adimensionalization procedure of the CRTBP can be assumed together with the following new adimensional parameters:

$$\omega_s = n_s - 1, \qquad a_s^3 n_s^3 = 1 + m_s, \qquad \alpha = \omega_s t. \tag{2.22}$$

Where ω_s and n_s are the mean angular velocity of the Sun, in synodic and inertial coordinates respectively; a_s is the scalar distance between the Sun and the EMB; m_s is the mass of the Sun. Hence, the position of the Sun $\boldsymbol{\rho}_s$ can be written as:

$$\boldsymbol{\rho}_s = a_s \left[\cos(\alpha + \alpha_0),\, \sin(\alpha + \alpha_0),\, 0\right]^T, \tag{2.23}$$

with α_0 initial phase angle of the Sun. The equations of motions are then derived [16]:

$$\begin{aligned}\boldsymbol{\rho}'' + C^T(2C'\boldsymbol{\rho}' + C''\boldsymbol{\rho}) = (\mu_2 - 1)\Bigg[&-\frac{\boldsymbol{\rho} - \boldsymbol{\rho}_s}{||\boldsymbol{\rho} - \boldsymbol{\rho}_s||^3} + \\ &-(1-\mu_1)\frac{\mu_1\boldsymbol{r} + \boldsymbol{\rho}_s}{||\mu_1\boldsymbol{r} + \boldsymbol{\rho}_s||^3} + \mu_1\frac{(1-\mu_1)\boldsymbol{r} - \boldsymbol{\rho}_s}{||(1-\mu_1)\boldsymbol{r} - \boldsymbol{\rho}_s||^3}\Bigg] + \\ &-(1-\mu_1)\frac{\boldsymbol{\rho} + \mu_1\boldsymbol{r}}{||\boldsymbol{\rho} + \mu_1\boldsymbol{r}||^3} - \mu_1\frac{\boldsymbol{\rho} - (1-\mu_1)\boldsymbol{r}}{||\boldsymbol{\rho} - (1-\mu_1)\boldsymbol{r}||^3},\end{aligned} \tag{2.24}$$

with $\boldsymbol{\rho}$ being the vector representing the position of the fourth body (the massless particle); $\boldsymbol{r} = (1,0,0)^T$ the distance vector between the Earth and the Moon; C the rotation matrix related to the synodic frame; $\mu_1 = \mu_M/(\mu_E + \mu_M)$ and $\mu_2 = (\mu_E + \mu_M + \mu_S)/(\mu_E + \mu_M)$. This set of equations is similar to that of the CRTBP, with a major difference in the definition of the potential function in with an additional term in the square brackets of Eq. (2.24) that can be considered a perturbation.

The **CCP** is a non-coherent model that considers one primary and two secondary bodies: $m_1 \gg m_2, m_3$. The secondary bodies revolve around the central primary in circular and coplanar orbits. The equations of motion in a m_1, m_2 synodic frame read [16]:

$$x'' - 2y' = \Omega^{(CCP)}_{/x}, \qquad y'' + 2x' = \Omega^{(CCP)}_{/y}, \qquad z'' = \Omega^{(CCP)}_{/z}, \tag{2.25}$$

where the pseudo-potential of the CCP is:

$$\begin{aligned}\Omega^{(CCP)} =& \frac{1}{2}(x^2 + y^2) + \frac{1-\mu_1}{||\boldsymbol{\rho}||} + \\ &+ \mu_1\left(\frac{1}{||\boldsymbol{\rho} - \boldsymbol{\rho}_2||} + \frac{\mu_3}{||\boldsymbol{\rho} - \boldsymbol{\rho}_3||} + \frac{\boldsymbol{\rho}_2 \cdot \boldsymbol{\rho}}{||\boldsymbol{\rho}_2||^3} + \mu_3\frac{\boldsymbol{\rho}_3 \cdot \boldsymbol{\rho}}{||\boldsymbol{\rho}_3||^3}\right),\end{aligned} \tag{2.26}$$

where $\mu_1 = m_2/(m_1 + m_2)$ is the synodic mass parameter and $\mu_3 = m_3/m_2$ is the perturbation mass ratio. The position vector of the two small attractors in the new rotating frame are:

$$\boldsymbol{\rho}_2 = (1,0,0)^T, \qquad \boldsymbol{\rho}_3 = \frac{||\boldsymbol{r}_3||}{||\boldsymbol{r}_2||}(\cos\varphi, \sin\varphi, 0)^T, \tag{2.27}$$

with φ being the term that make the system non-autonomous, the phase angle of the apparent motion of the third primary with respect to the first two. Again, the similarity with the CRTBP is evident, with differences in the potential function.

2.2.2. RPRnBP: Equations of Motion

To correctly present the equations of motion of the RPRnBP, the rotation from the Solar System Barycenter (SSB) to the Roto-Pulsating frame must be defined. Let $\boldsymbol{R}$ and $\boldsymbol{V}$ be the dimensional position and velocity, respectively, of a massless particle P in the inertial SSB-centered frame. Let $\boldsymbol{\rho}$ be its non-dimensional position in the Roto-Pulsating frame with two primaries as in Fig. 2.5. The transformation is defined as follows [16]:

$$\boldsymbol{R} = \boldsymbol{b} + kC\boldsymbol{\rho}, \qquad \boldsymbol{V} = \dot{\boldsymbol{b}} + \dot{k}C\boldsymbol{\rho} + \dot{\tau}kC\boldsymbol{\rho}', \qquad \tau = n(t - t_0), \tag{2.28}$$

where the dots identify derivatives with respect to time while primes identify derivatives with respect to non-dimensional times. Then:

$$\boldsymbol{b}(t) = \frac{m_1\boldsymbol{R}_1 + m_2\boldsymbol{R}_2}{m_1 + m_2}, \qquad k(t) = ||\boldsymbol{R}_2 - \boldsymbol{R}_1||, \qquad C(t) = [\boldsymbol{e}_1, \boldsymbol{e}_2, \boldsymbol{e}_3], \tag{2.29}$$

and

$$\boldsymbol{e}_1 = \frac{\boldsymbol{R}_2 - \boldsymbol{R}_1}{k}, \qquad \boldsymbol{e}_2 = \boldsymbol{e}_3 \times \boldsymbol{e}_1, \qquad \boldsymbol{e}_3 = \frac{(\boldsymbol{V}_2 - \boldsymbol{V}_1) \times (\boldsymbol{R}_2 - \boldsymbol{R}_1)}{||(\boldsymbol{V}_2 - \boldsymbol{V}_1) \times (\boldsymbol{R}_2 - \boldsymbol{R}_1)||}. \tag{2.30}$$

Here $m_i, \boldsymbol{R}_i$ and $\boldsymbol{V}_i$ are the mass, position and velocity of the primaries for $i = 1, 2$.
Thus, the transformation is composed by two parts: the first one, $\boldsymbol{b}$, describes a translation from the SSB to the barycenter of the primaries. The second one describes a rotation through the orthogonal cosine angle matrix C, scaled by the time dependent factor k. Eventually, the primaries are always aligned with the x-axis of the new frame.
The Lagrangian function of the complete gravitational model is [16]:

$$\mathcal{L}(\boldsymbol{R}, \dot{\boldsymbol{R}}, t) = \frac{1}{2}\dot{\boldsymbol{R}} \cdot \dot{\boldsymbol{R}} + \sum_{j\in\mathcal{S}} \frac{Gm_j}{||\boldsymbol{R} - \boldsymbol{R}_j||}, \tag{2.31}$$

where $\mathcal{S}$ is the set of the Solar System planets included in the model which, in the case of this work, are all including Pluto. Position and velocity of them are obtained through ephemeris data through NASA's SPICE toolkit. The other perturbation included in the model is the SRP, which creates an acceleration opposite to the Sun direction on the spacecraft. It can be defined as following [11]:

$$\boldsymbol{a}_{SRP} = SP_0\frac{\boldsymbol{R} - \boldsymbol{R}_s}{||\boldsymbol{R} - \boldsymbol{R}_s||^3}, \qquad SP_0 = (a + c_r)\frac{A}{m}\frac{\Psi_0 d_0^2}{c}, \tag{2.32}$$

with SP_0 being the SRP parameter, c_r the reflectivity coefficient of the spacecraft, Ψ_0 the solar flux intensity and d_0 the distance from the Sun.

Finally, applying the transformation of Eq. (2.28) to the Lagrangian function Eq. (2.31) the equations of motion of the RPRnBP are obtained [11]:

$$\begin{aligned}\boldsymbol{\rho}'' = &-\frac{1}{\dot{\tau}}\left(\frac{2\dot{k}}{k}I + 2C^T\dot{C}\right)\boldsymbol{\rho}' - \frac{1}{\dot{\tau}^2}\left[\left(\frac{\ddot{k}}{k}I + 2\frac{\dot{k}}{k}C^TC + \dot{C}^T\ddot{C}\right)\boldsymbol{\rho} + \frac{C^T\ddot{\boldsymbol{b}}}{k}\right] + \\ &+ \nabla\Omega + \frac{SP_0}{k^3n^2}\frac{\boldsymbol{\rho}-\boldsymbol{\rho}_s}{||\boldsymbol{\rho}-\boldsymbol{\rho}_s||^3},\end{aligned} \tag{2.33}$$

where $\nabla\Omega$ is the gradient of the pseudo-potential of the RPRnBP:

$$\Omega = \sum_{j\in S}\frac{\hat{\mu}_j}{||\boldsymbol{\rho}-\boldsymbol{\rho}_j||}\left[1 + \frac{J_{2,j}R_{b,j}^2}{2k^2||\boldsymbol{\rho}-\boldsymbol{\rho}_j||^2}\left(1 - \frac{3(\boldsymbol{\rho}-\boldsymbol{\rho}_j)C^TI_zC(\boldsymbol{\rho}-\boldsymbol{\rho}_j)}{||\boldsymbol{\rho}-\boldsymbol{\rho}_j||^2}\right)\right], \tag{2.34}$$

and $\hat{\mu}_j = \mu_j/(\mu_1+\mu_2)$.
The vector Eq. (2.33) can be written per components as follows:

$$\begin{cases} x'' = b_1 + b_4x' + b_5y' + b_7x + b_9y + b_8z + b_{13}\Omega_{/x} + a_x, \\ y'' = b_2 - b_5x' + b_4y' + b_6z' - b_9x + b_{10}y + b_{11}z + b_{13}\Omega_{/y} + a_y, \\ z'' = b_3 - b_6y' + b_4z' + b_8x - b_{11}y + b_{12}z + b_{13}\Omega_{/z} + a_z, \end{cases} \tag{2.35}$$

with coefficients:

$$\begin{aligned} b_1 &= -\frac{\ddot{\boldsymbol{b}}\cdot\boldsymbol{e}_1}{kn^2}, & b_8 &= \frac{1}{n^2}\dot{\boldsymbol{e}}_1\cdot\dot{\boldsymbol{e}}_3, \\ b_2 &= -\frac{\ddot{\boldsymbol{b}}\cdot\boldsymbol{e}_2}{kn^2}, & b_9 &= \frac{1}{n^2}\left(2\frac{\dot{k}}{k}\boldsymbol{e}_2\cdot\dot{\boldsymbol{e}}_1 + \boldsymbol{e}_2\cdot\ddot{\boldsymbol{e}}_1\right), \\ b_3 &= -\frac{\ddot{\boldsymbol{b}}\cdot\boldsymbol{e}_3}{kn^2}, & b_{10} &= -\frac{1}{n^2}\left(\frac{\ddot{k}}{k} - \dot{\boldsymbol{e}}_2\cdot\dot{\boldsymbol{e}}_2\right), \\ b_4 &= -\frac{2}{n}\frac{\dot{k}}{k}, & b_{11} &= \frac{1}{n^2}\left(2\frac{\dot{k}}{k}\boldsymbol{e}_3\cdot\dot{\boldsymbol{e}}_2 + \boldsymbol{e}_3\cdot\ddot{\boldsymbol{e}}_2\right), \\ b_5 &= \frac{2}{n}\boldsymbol{e}_2\cdot\dot{\boldsymbol{e}}_1, & b_{12} &= -\frac{1}{n^2}\left(\frac{\ddot{k}}{k} - \dot{\boldsymbol{e}}_3\cdot\dot{\boldsymbol{e}}_3\right), \\ b_6 &= \frac{2}{n}\boldsymbol{e}_3\cdot\dot{\boldsymbol{e}}_2, & b_{13} &= \frac{\mu_1+\mu_2}{k^3n^2}. \\ b_7 &= -\frac{1}{n^2}\left(\frac{\ddot{k}}{k} - \dot{\boldsymbol{e}}_1\cdot\dot{\boldsymbol{e}}_1\right), \end{aligned} \tag{2.36}$$

It is worth noting that the high-fidelity RPRnBP model serves as the general case from which the equations of motion, for all other models lower in the hierarchical ladder, can be derived by appropriately selecting the coefficients.

2.3. High Fidelity Substitutes of Periodic Orbits

2.3.1. Halo orbits in the CRTBP

In the context of the CRTBP, various types of closed periodic orbits can be computed. It is the case of Halo orbits, which are 3D periodic orbits that branch out from the Lyapunov family when the in-plane and out-plane frequencies match. Halo orbits do not appear as solutions of the linearized equations, they indeed require higher-order solutions to enforce the matching of the frequencies [1].

A common practice is to perform a differential correction on a guess initial condition close to the equilibrium point and, once the Halo orbit is obtained, find the sought one through numerical continuation. The full mathematical procedure is not presented here, as it is not part of the purposes of this work.

The guess for the initial condition, considering the geometry of Halo orbits must satisfy the symmetry about the xz-plane, as well as the perpendicular velocity plane crossing:

$$\tilde{\boldsymbol{x}}_0 = (x_0, \quad 0, \quad z_0, \quad 0, \quad \dot{y}_0, \quad 0)^T \tag{2.37}$$

After the first Halo orbit is obtained, it is possible to exploit the numerical continuation to characterize the family. The continuation algorithm involves iterating the previously applied differential correction with varying initial condition guesses. Over a finite number of steps, within specified limits (e.g., the Jacobi constant C_j), the initial conditions are progressively adjusted. Through this process, the entire family of orbits, along with the desired final orbit, is determined. The Halo orbit family can be visualized in Fig. 2.7.

2.3.2. From Halo to Quasi-Halo Orbit

The orbits obtained are purely theoretical in nature. In more detailed environment model, the inherently unstable character of the Halo orbits becomes explicit in matter of days, as they begin to diverge from the theoretical behavior. To maintain the integrity of those orbits over time, methodologies to correct them while preserving their essential characteristics must be developed.

The refinement of CRTBP periodic orbits in RPRnBP quasi-periodic ones is achieved following the technique developed by D. A. Dei Tos and F. Topputo [17].

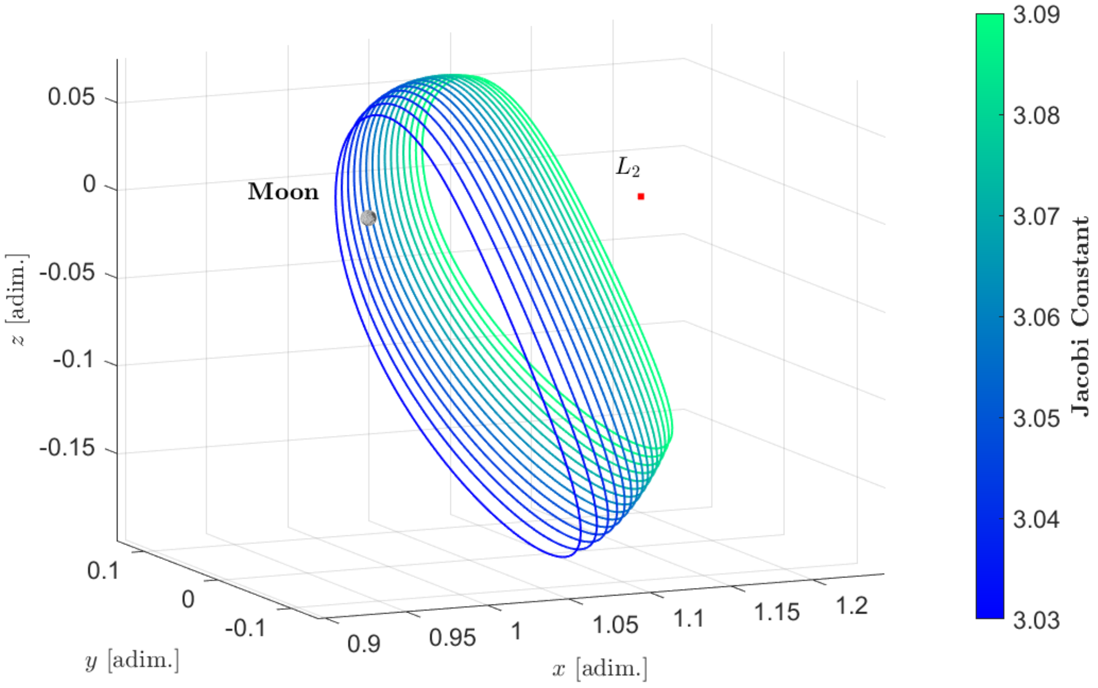

Figure 2.7: Halo orbit family @ EMB centered adimensional rotating frame.

This technique is based on an iterative algorithm that employs a modified multiple-shooting approach. Specifically, an initial seed orbit in the CRTBP is discretized into a set of nodes, and the refinement process aims to generate a piecewise-continuous trajectory that remains as close as possible to the original seed orbit.

The problem can be stated as follows: find a modified initial condition, $\hat{\boldsymbol{x}}_0$, such that $\gamma_{nb}(\hat{\boldsymbol{x}}_0)$ retains the geometrical and dynamical features of $\gamma_{3b}(\boldsymbol{x}_0)$, with $\gamma_{3b}(\boldsymbol{x}_0)$ being a periodic orbit and $\gamma_{nb}(\hat{\boldsymbol{x}}_0)$ a quasi-periodic orbit with similar amplitude and harmonic content with respect to the periodic one [17].

The Modified Multiple Shooting

A Two-Point Boundary Value Problem (TPBVP) consists in finding $\boldsymbol{x}(t)$ such that:

$$\dot{\boldsymbol{x}} = \boldsymbol{f}(\boldsymbol{x}, t), \qquad \boldsymbol{h}(\boldsymbol{x}(t_0), \boldsymbol{x}(t_f)) = \boldsymbol{0}, \tag{2.38}$$

where $\boldsymbol{x}$ is 6-dimensional and $\boldsymbol{h}$ are six boundary conditions. The term "modified" comes from the fact that in this case, since periodicity can not be enforced in the RPRnBP, free boundary conditions at the beginning and end of the trajectory must be adopted.
The solution is discretized in m grid points such that $t_0 = t_1 < t_2 < \cdots < t_m = t_f$, and is

written as $\boldsymbol{s}_k = \boldsymbol{x}(t_k)$, $k = 1, \ldots, m$. This grid defines $m-1$ segments in which a TPBVP is solved guaranteeing continuity of the solution at both ends.
Define the defect vector as:

$$\boldsymbol{\zeta}_k = \boldsymbol{\varphi}_{nb}(\boldsymbol{s}_k, t_k; t_{k+1}) - \boldsymbol{s}_{k+1}, \quad k = 1, \ldots, m-1. \tag{2.39}$$

The problem is to find the states $\boldsymbol{s}_k$ such that:

$$\boldsymbol{h}(\boldsymbol{s}_1, \boldsymbol{s}_m) = \boldsymbol{0}, \qquad \boldsymbol{\zeta}_k = \boldsymbol{0}, \qquad k = 1, \ldots, m-1. \tag{2.40}$$

Where the number of unknowns $\boldsymbol{s}_k$ are $6m$ while the boundary conditions are $6(m-1)$ because of the modified logic that has been implemented to treat the free boundary conditions at both ends. It is evident that, to cope with the missing 6 equations, an optimization procedure must be adopted.

Let

$$\begin{aligned} \boldsymbol{s} =& (\boldsymbol{s}_1, \boldsymbol{s}_2, \ldots, \boldsymbol{s}_m), \\ \boldsymbol{c}(\boldsymbol{s}) =& (\zeta_1(\boldsymbol{s}_1, \boldsymbol{s}_2),\ \zeta_2(\boldsymbol{s}_2, \boldsymbol{s}_3), \ldots, \zeta_{m-1}(\boldsymbol{s}_{m-1}, \boldsymbol{s}_m)), \end{aligned} \tag{2.41}$$

be the unknown vector and the defect vector, respectively. Then, the zeros of the $\boldsymbol{c}(\boldsymbol{s})$ function are sought while simultaneously minimizing a scalar objective function $f(\boldsymbol{s})$ which is:

$$f(\boldsymbol{s}) = \frac{1}{2}\boldsymbol{c} \cdot \mathcal{M}\boldsymbol{c}, \qquad \text{with} \qquad \mathcal{M} = \text{weights} = \boldsymbol{I}_{6\times 6}. \tag{2.42}$$

To improve computational efficiency, the gradients of both the objective function and the constraints are implemented analytically. In particular, the gradient of the objective function is given by:

$$\mathbf{g} = \nabla_s f(\boldsymbol{s}), \tag{2.43}$$

while the Jacobian of the constraint vector $\boldsymbol{c}(\boldsymbol{s})$, denoted as $\mathcal{J}_c(\boldsymbol{s}) = \nabla_{\boldsymbol{s}}\boldsymbol{c}(\boldsymbol{s})$, is assembled exploiting the structured nature of the multiple-shooting formulation [17]. By explicitly constructing these quantities, the need for numerical differentiation is avoided, significantly reducing the computational cost of the technique.
The optimization is performed using MATLAB's built-in function `fmincon`[2], adopting the interior-point algorithm [7]. Due to the high computational cost associated with this approach, the procedure is implemented in a parallel fashion.
Applying this technique to the Halo orbit found in the previous Sec. 2.3.1 for the LUMIO case, the Quasi-Halo counterpart is computed for a few starting epochs. The one that will

---

[2] `https://it.mathworks.com/help/optim/ug/fmincon.html`

be analyzed throughout this thesis is the one with starting epoch *01 Jan 2027 00:00:00 UTC*, while others are reported in Appendix A. The baseline theoretical trajectory is taken for 26 periods, which is the expected lifetime of the LUMIO satellite, while the discretization is performed with $m = 260$ nodes. The resulting Quasi-Halo orbit is presented in the following Fig. 2.8.

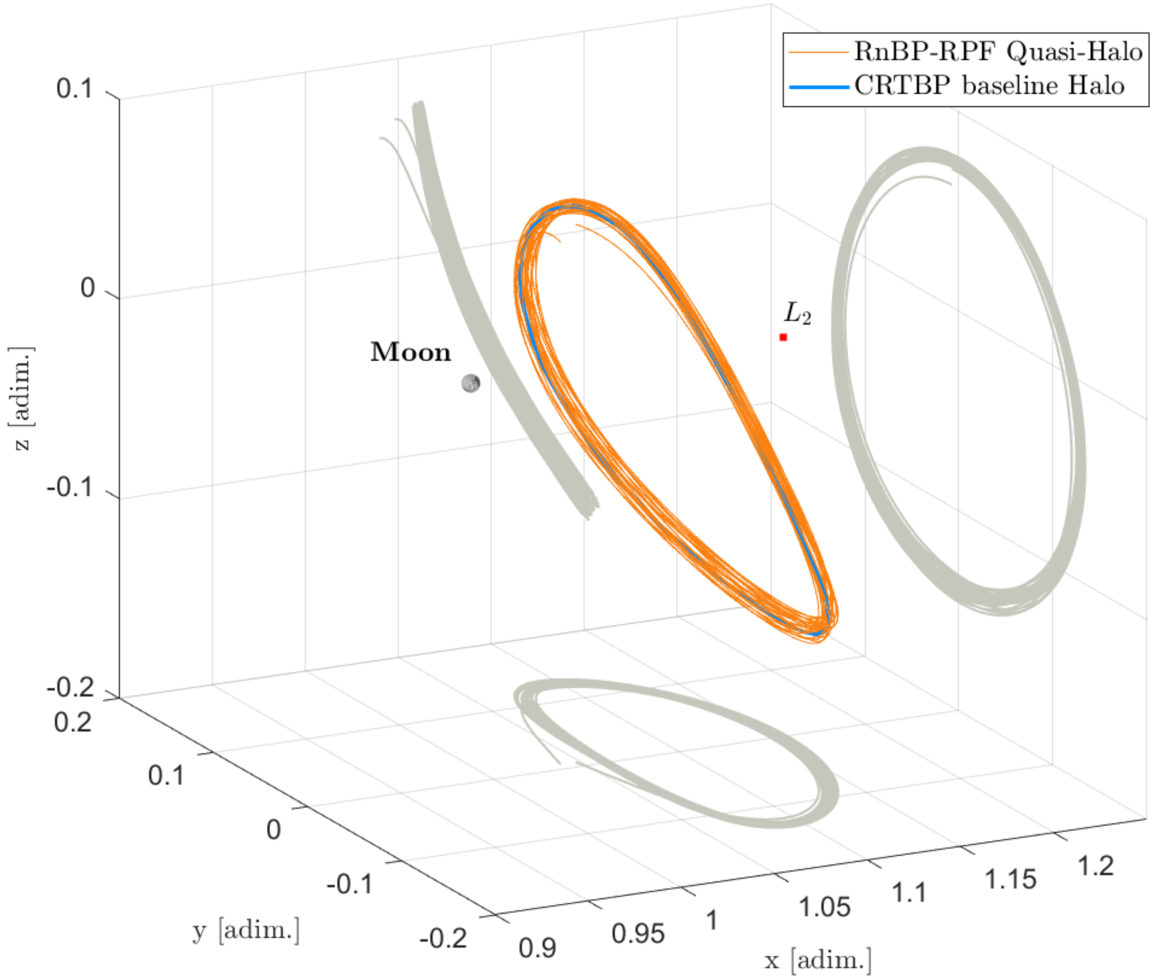

Figure 2.8: LUMIO Quasi-Halo orbit @ EMB centered adimensional rotating frame. Solution obtained from the baseline Halo orbit in CRTBP in blue.

3 | Station Keeping Techniques

The intrinsic instability of the three-body orbits, together with the perturbations that affect the spacecraft at the libration points, yields to a quick divergence from the expected behavior. To ensure long-term operability and mission safety, the spacecraft must actively correct its trajectory to remain close to the theoretical one. Thus, the problem of station-keeping aims to minimize the trajectory deviation, control instability growth and, while accomplishing this, limit the propellant consumption.
As mentioned in the introduction, two main branches of techniques exist. Continuous control, which relies on small and persistent forces produced, for example, by an electrical propulsion unit, is not presented here as it does not concern CubeSats.
The impulsive control is the preferred strategy to follow in the case of small satellites with a chemical propulsion unit. In this chapter, two well known impulsive strategies will be presented: the Floquet Modes Approach and the Target Point Approach. These approaches differ fundamentally in their conceptual framework, as they belong to distinct categories of station-keeping techniques. Particular effort is given in the description of the TPA, which is the baseline for the LUMIO spacecraft [10, 15, 61]. Lastly, the eclipse avoidance strategies are discussed and it is addressed the need for a different technique.

3.1. Floquet Mode Approach

The variational equations for motion in the vicinity of the Halo orbit, or any solution close to it, can be approximated as linear with the use of periodic coefficients. Hence, both qualitative and quantitative information can be obtained about the trend of the nonlinear system. As anticipated in Sec. 2.1.4, the information lies in the eigenspace of the Monodromy matrix: its eigenvalues λ_i and eigenvectors $\boldsymbol{e}_i$ with $i = 1, \dots, 6$. The procedure presented is based on G. Gómez research work [31].

The purpose of the controller is to effectively eliminate the unstable component of the error vector, defined as the difference between the tracked and nominal coordinates:

$$\boldsymbol{\delta}(t) = (\delta x, \delta y, \delta z, \delta \dot{x}, \delta \dot{y}, \delta \dot{z}) \tag{3.1}$$

Instead of relying on the eigenvectors, it is convenient to employ the Floquet modes, recovered as:

$$\bar{\boldsymbol{e}}_i(t) = \boldsymbol{e}_i(t) \cdot \exp\left[-\frac{t}{T}\log\lambda_1\right], \qquad i = 1, \dots, 6. \tag{3.2}$$

where T is the orbital period.
At any epoch t, the error vector can be expressed as:

$$\boldsymbol{\delta}(t) = \sum_{i=1}^{6} \alpha_i \bar{\boldsymbol{e}}_i(t) \tag{3.3}$$

The objective of the controller is to perform a maneuver $\boldsymbol{\Delta} = (0, 0, 0, \Delta_x, \Delta_y, \Delta_z)^T$ such that the magnitude of the component in the unstable direction, α_1, is reduced to zero.
For a practical implementation the projection factor along the unstable direction is exploited. It is defined as the vector $\boldsymbol{\pi}$ such that $\boldsymbol{\delta} \cdot \boldsymbol{\pi} = \alpha_1$. To nullify the unstable projection the following condition must be satisfied:

$$(\boldsymbol{\delta} + \boldsymbol{\Delta}) \cdot \boldsymbol{\pi} = 0 \qquad \rightarrow \qquad \Delta_x \pi_4 + \Delta_y \pi_5 + \Delta_z \pi_6 + \alpha_1 = 0 \tag{3.4}$$

Choosing, without loss in generality, a two axis controller with $\Delta_z = 0$, and minimizing the Euclidean norm of $\boldsymbol{\Delta}$, the following is obtained:

$$\Delta_x = -\frac{\alpha_1 \pi_4}{\pi_4^2 + \pi_5^5}, \qquad \Delta_y = -\frac{\alpha_1 \pi_5}{\pi_4^2 + \pi_5^2}. \tag{3.5}$$

Various constraints must be taken into account when dealing with this technique:

- Without tracking errors, the evolution of α_1 is exponential in time. When instead they are included, a lower bound must be introduced in order to prevent useless maneuvers. The value of $\alpha_{1,min}$ must be selected of the same order of magnitude of the orbit determination accuracy. On the other hand, to avoid expensive maneuvers, an upper bound α_{max} must be defined as well. When $\alpha_{1,min} < \alpha_1 < \alpha_{1,max}$, the maneuver is executed only if the deviation has been growing at an exponential rate.
- The maneuver is executed only if the magnitude of the computed $\boldsymbol{\Delta}$ is greater than a minimum value, which is in the order of magnitude of the thrusters' accuracy, typically 0.5 – 1 cm/s [11].
- A minimum time between two consecutive tracking epochs, and consequently two maneuvers, must be defined.

This strategy has been developed and assessed in [68]. The results indicate that the Floquet Mode Approach may encounter limitations in certain quasi-periodic cislunar trajectories. In particular, since the method relies on the assumption of periodicity to compute corrective maneuvers, deviations from strict periodic behavior can cause the STM to become progressively ill-conditioned, ultimately leading to unreliable long-term station-keeping performance.

3.2. Target Point Approach

The TPA is a well known strategy that optimizes an impulsive maneuver in order to reduce the downstream deviation between the actual trajectory and the reference one at specific target times, the so-called target points. The optimal $\Delta \boldsymbol{v}_{S/K}$ is retrieved as solution of a Linear Quadratic Regulator (LQR) problem that minimizes a weighted sum of the maneuvers cost and the position deviation from a reference trajectory at the targets. The cost function reads [10, 15, 36]:

$$J_{S/K} = \Delta \boldsymbol{v}_{S/K}^T(t_v) Q \Delta \boldsymbol{v}_{S/K}(t_v) + \sum_{i=1}^{N_{pt}} \delta \boldsymbol{r}^T(t_i) R_i \delta \boldsymbol{r}(t_i), \tag{3.6}$$

where N_{pt} is the number of target points (typically 2 or 3), Q is the cost weight matrix, $\delta \boldsymbol{r}(t_i)$ and R_i are the predicted position deviation from the nominal trajectory and the weight matrix of this deviation, respectively, at the $i-$th target point. The position deviation is computed by means of the STM of the reference trajectory:

$$\delta \boldsymbol{r}(t_i) = \boldsymbol{\Phi}_{rr}(t_c, t_i) \delta \boldsymbol{r}(t_c) + \boldsymbol{\Phi}_{rv}(t_c, t_i) \delta \boldsymbol{v}(t_c) + \boldsymbol{\Phi}_{rv}(t_v, t_i) \Delta \boldsymbol{v}_{S/K}(t_c) \tag{3.7}$$

Particular care must be taken in describing Eq. (3.7). In particular, $\boldsymbol{\Phi}_{rr}$ and $\boldsymbol{\Phi}_{rv}$ are 3×3 matrices that map the deviation of position and velocity respectively, to a position deviation at a subsequent epoch, the target point. The prevision is made from the epoch t_c, which is defined as the cut-off time: in the context of station-keeping, the cut-off time is defined as the time instant at which the orbit determination process is stopped. Beyond this time, the estimated spacecraft state is no longer updated through measurements. The typical value of t_c for Quasi-Halo applications is 1-2 days before the maneuver epoch t_v [61]. The last term of Eq. (3.7), propagates the to-be-computed $\Delta \boldsymbol{v}_{S/K}$, considered as a velocity deviation from t_v (maneuver epoch) to the target point, translating it in a position deviation through $\boldsymbol{\Phi}_{rv}$. The solution of the minimization problem yields the analytical expression for the optimal station-keeping maneuver [10]:

$$\Delta \boldsymbol{v}_{S/K} = A \sum_{i=1}^{N_{pt}} \left[\alpha_i \delta \boldsymbol{r}(t_c) + \beta_i \delta \boldsymbol{v}(t_c) \right], \tag{3.8}$$

where A, α_i and β_i are defined as:

$$\begin{aligned} A &= -\left[(Q^T + Q) + \sum_{i=1}^{N_{pt}} \mathbf{\Phi}_{rv}^T(t_v, t_i)(R_i^T + R_i)\mathbf{\Phi}_{rv}(t_v, t_i)\right]^{-1}, \\ \alpha_i &= \mathbf{\Phi}_{rv}^T(t_v, t_i)\left(R_i^T + R_i\right)\mathbf{\Phi}_{rr}(t_c, t_i), \\ \beta_i &= \mathbf{\Phi}_{rv}^T(t_v, t_i)\left(R_i^T + R_i\right)\mathbf{\Phi}_{rv}(t_c, t_i). \end{aligned} \tag{3.9}$$

It must be pointed out that all the STMs in the previous equations are related to the reference orbit. These can be computed a priori and used when needed, since they do not depend on the real trajectory, which is affected by uncertainty and random variables.

Indeed, to precisely simulate a realistic trajectory [15], a possible modeling approach, which will be adopted in this thesis, is:

- The spacecraft's state initial condition is altered to account for Orbit Injection (OI) errors, $\boldsymbol{\varepsilon}_{OI}$.
- The tracking windows include Orbit Determination (OD) campaigns, which estimate the spacecraft state and, in order to simulate tracking errors, the satellite's state is altered with $\boldsymbol{\varepsilon}_{OD}$.
- At each maneuver required, the magnitude and direction of it is modeled taking into account the accuracy of the thrusters, altering randomly each component of the $\boldsymbol{\Delta v}_{S/K}$ with $\boldsymbol{\varepsilon}_{EX}$.

These errors are all modeled and generated with zero-mean Gaussian distributions:

$$\boldsymbol{\varepsilon}_{OI} \sim \mathcal{N}(0, \sigma_{OI}^2), \qquad \boldsymbol{\varepsilon}_{OD} \sim \mathcal{N}(0, \sigma_{OD}^2), \qquad \boldsymbol{\varepsilon}_{EX} \sim \mathcal{N}(0, \sigma_{EX}^2). \tag{3.10}$$

Where σ_{OI}^2, σ_{OD}^2, σ_{EX}^2 are the covariances of orbit insertion, orbit determination, and maneuver execution uncertainties, respectively.

Let $\boldsymbol{x}_{ref}$ be the reference trajectory (e.g. the one computed in Sec. 2.3.2), and $\boldsymbol{x}_{true}$ the true RPRnBP propagated trajectory. Assuming that the satellite is injected into the reference trajectory at the epoch t_0:

$$\boldsymbol{x}_{true}(t_0) = \boldsymbol{x}_{ref}(t_0) + \boldsymbol{\varepsilon}_{OI} \tag{3.11}$$

The station-keeping maneuver computed with the Eq. (3.8) and Eq. (3.9) is perturbed as follows:

$$\Delta\boldsymbol{v}_{S/K}(t_v) = \Delta\boldsymbol{v}_{S/K}(t_v) + \Delta\boldsymbol{v}_{S/K}(t_v) \circ \boldsymbol{\varepsilon}_{EX}, \tag{3.12}$$

where $\circ$ represents the Hadamard product. Similarly to the Floquet Mode Approach, several constraints are needed [11]:

- The time between successive maneuvers must be greater than a minimum time.
- The deviation with respect to the reference trajectory must be greater than a minimum value.
- The computed $\Delta \boldsymbol{v}_{S/K}$, to be executed must be greater than a minimum ΔV_{min} to avoid too small maneuvers.

A geometrical overview of the TPA simulation process is given in Fig. 3.1:

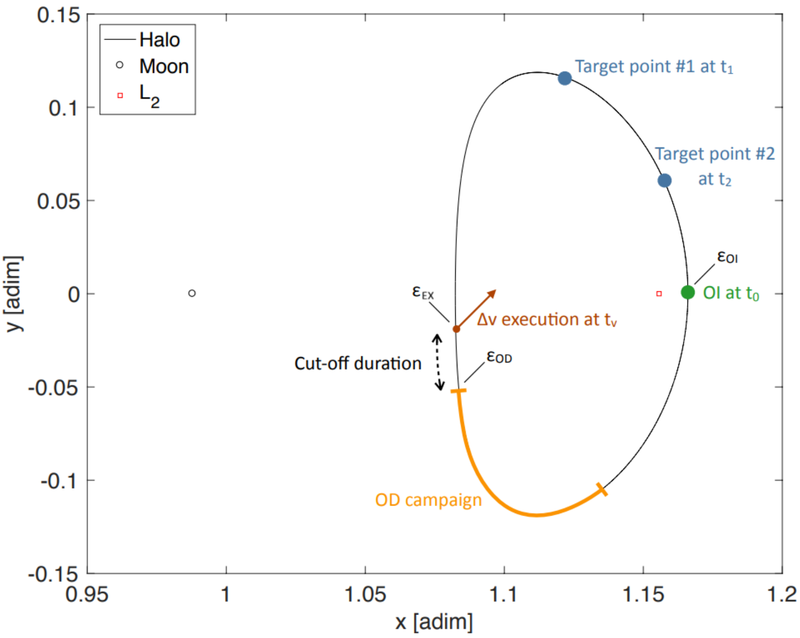

Figure 3.1: TPA geometry of station-keeping simulation process @ EMB centered adimensional rotating frame [15, 61].

Maintaining the real trajectory in proximity to the reference one is of fundamental importance, because of the nature of the station-keeping strategy. In particular, since the method is based on the linearization through the STMs of the reference trajectory, allowing high deviations from it do not ensure the validity of the approximation yielding to divergence and, as a consequence, failure of the station-keeping.

This does not necessarily arise in all mission scenarios, as certain quasi-periodic trajectories can be maintained within acceptable bounds, depending on the magnitude of navigation and injection errors. The implementation of the adopted strategy is presented in Sec. 4.1.2, together with a corresponding statistical analysis.

3.3. Eclipse Avoidance Strategies

The cislunar environment is characterized by two primary sources of shadow, generated by the occultation of the Sun caused by the Earth and the Moon. In this context, eclipses represent a critical constraint for small spacecrafts, particularly due to their limited power availability. In recent years, CubeSats have expanded their capabilities and operational domains, becoming important platforms especially for scientific missions. Eclipses become a serious problem when the application domain gets further from the Earth. Indeed, a CubeSat orbiting the Earth in a typical LEO can experience, in the worst case scenario, shadow periods of 30-35 minutes [37]. On the other hand, the eclipses durations in the Quasi-Halo L_2 environment go up to 4.5-5 hours, which is higher than the threshold supported. In order to ensure continuous operations and to increase mission safety, eclipse mitigation strategies are being developed.

3.3.1. Passive Avoidance

The problem can be approached with passive strategies. These rely on the natural dynamics of the system and orbital geometry, without requiring dedicated maneuvers for eclipse avoidance. In particular, following certain methodologies during the mission design phase can lead to orbits that are naturally free from eclipse events or orbits where these events are limited. The primary degrees of freedom that these strategies exploit are geometric in nature, such as the type of orbit, size and phase, and temporal such as the initial epoch of the operative phase.

The work of S. Wishnek et al. [64] faces this problem by applying a grid search with which are found trajectories that remain eclipse-free for a two years example mission, as well as orbits that remain long-term eclipse-free. The grid search studies the full domain of the problem. Two independent variables are discretized for this scenario: the initial position of the satellite and its phase within the periodic orbit. By varying these two, the possible trajectories at the sampled points are computed and among all of them, and it has been demonstrated that eclipse-free trajectories exist among the solutions.

Other studies are instead based on the resonance phenomenon. The time between successive conjunctions of the Earth-Moon-Sun system is defined by the synodic period of the Moon, which is 29.5306 days. By choosing a certain ratio $n : m$ between the n revolutions along the orbit and the m synodic cycles of the Moon, the shadow generated by the Moon won't surely intersect the orbit. This is achieved in the work of C. Davis et al. [14], where it is studied a baseline trajectory for the Gateway Mission which exploits the resonance with the lunar synodic period to avoid long eclipses by setting up a repeating geometry. Then, the careful epoch and phase selection also allows to avoid Earth eclipses by orienting the NRHO such that the ecliptic plane crossings do not occur when the Earth lies between the spacecraft and the Sun. These results must be integrated with a station-keeping technique that performs accurate phase control. Without the latter, the spacecraft would drift from the baseline and the eclipse-free characteristic would be lost.

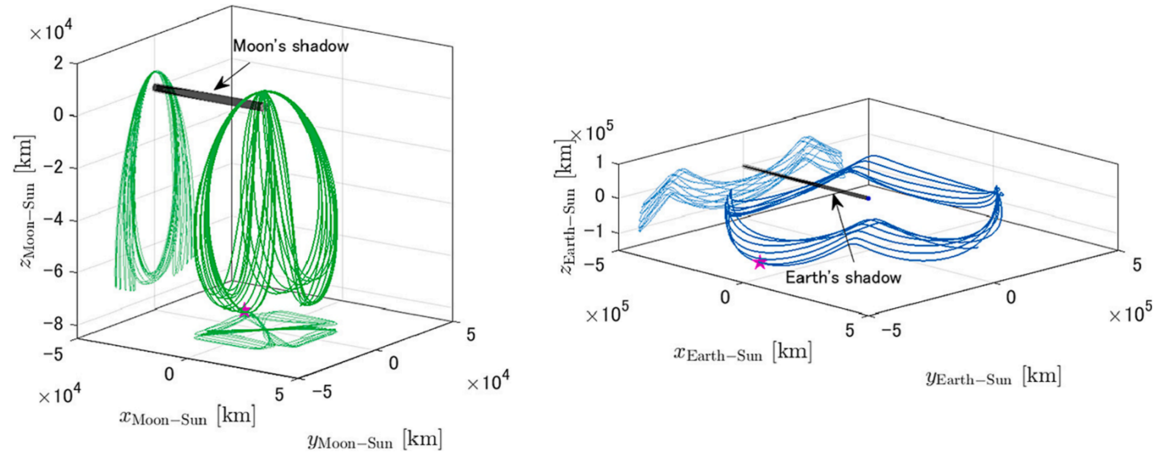

Figure 3.2: A 4:1 synodic resonant NRHO in the Moon-Sun rotating frame (left) and the same in the Earth-Sun rotating frame (right) [9].

In a related study [11], it has been investigated the refinement of high-fidelity Quasi-Halo trajectories into eclipse-free configurations by modifying the standard differential correction procedure, in particular through the introduction of an eclipse constraint. The results demonstrated that eclipse-free solutions can be obtained for multiple injection epochs while preserving the nominal orbital geometry and satisfying the station-keeping requirements, without altering the underlying correction technique.

These passive strategies are advantageous because of the absence of additional propellant consumption, simplicity of operations and overall reduced computational requirements. On the other hand, the eclipse-free condition is always based on specific epochs selection and narrow time windows that, in practical applications, are often difficult to respect. Moreover, when a spacecraft is launched as a secondary payload, both the launch date and the deployment epoch are constrained by the primary mission design and are therefore not selectable a priori. An active, robust, initial epoch independent avoidance strategy must be developed.

3.3.2. Active Avoidance

The eclipse problem can also be approached with active strategies. These rely on ad-hoc maneuvers that are composed of a certain number of burns that actively change momentarily the trajectory of the spacecraft, deviating on purpose from the reference, avoiding shadow regions. An active shadow avoidance procedure offers greater flexibility in mission design, and serves as a secure backup in case potential passive strategies adopted fail.

To this aim, the work of Y. Shang et al. [49] proposes a closed-loop, three-impulse orbital maneuvering strategy to mitigate the risks of eclipse events in DRO. This methodology is composed of three sequential steps: (*i*) shadow events are forecasted and detected; (*ii*) solar eclipse avoidance maneuver is executed; (*iii*) spacecraft is returned to its nominal orbit. The eclipse avoidance maneuver is composed by three burns $\delta\boldsymbol{v}_1, \delta\boldsymbol{v}_2, \delta\boldsymbol{v}_3$. Even though a closed analytical formula is obtained for the computation of the magnitude and direction of the burn, the maneuver time remains a control variable to be determined, thus, to be optimized through an optimization process. In particular, since three burns are required, three separate optimizations must be carried out to determine the execution epochs that minimize the avoidance maneuver in terms of the total $\Delta\boldsymbol{v}$. The numerical results show that a stable DRO orbit would frequently encounter eclipse events which can be actively avoided with this strategy. The average annual velocity impulse needed for Earth's and Moon's shadow avoidance are respectively 34.988 m/s and 19.786 m/s.

In mission scenarios characterized by stringent operational constraints, this approach represents a suitable solution. However, any optimization-based process should be avoided due to the limited time available between orbit determination cut-off and maneuver execution; therefore, a deterministic procedure is preferable. The active avoidance concept respects typical mission constraints and represents a realistic solution from an operational standpoint. On the other hand, the propellant cost associated with such strategies (based on the previously presented work of Y. Shang et al. [49]) may be significant when applied to CubeSat platforms. Moreover, since the referenced analysis was performed on a DRO, which is inherently stable, it can be expected that in an unstable Quasi-Halo environment the associated cost could be higher. This constitutes one of the central objectives of this thesis: as stated in the research question, the impact of the formulated active avoidance strategy on the overall ΔV budget will be quantitatively assessed.

4 | The LUMIO Mission

The Lunar Meteoroid Impacts Observer (LUMIO) is a CubeSat mission to a Halo orbit at Earth-Moon L_2 that shall observe, quantify and characterize meteoroid impacts on the Lunar far side by detecting their flashes. The 12U spacecraft incorporates state-of-the-art technologies, serving as a pioneer in demonstrating how CubeSats can be viable platforms for deep-space science and exploration.

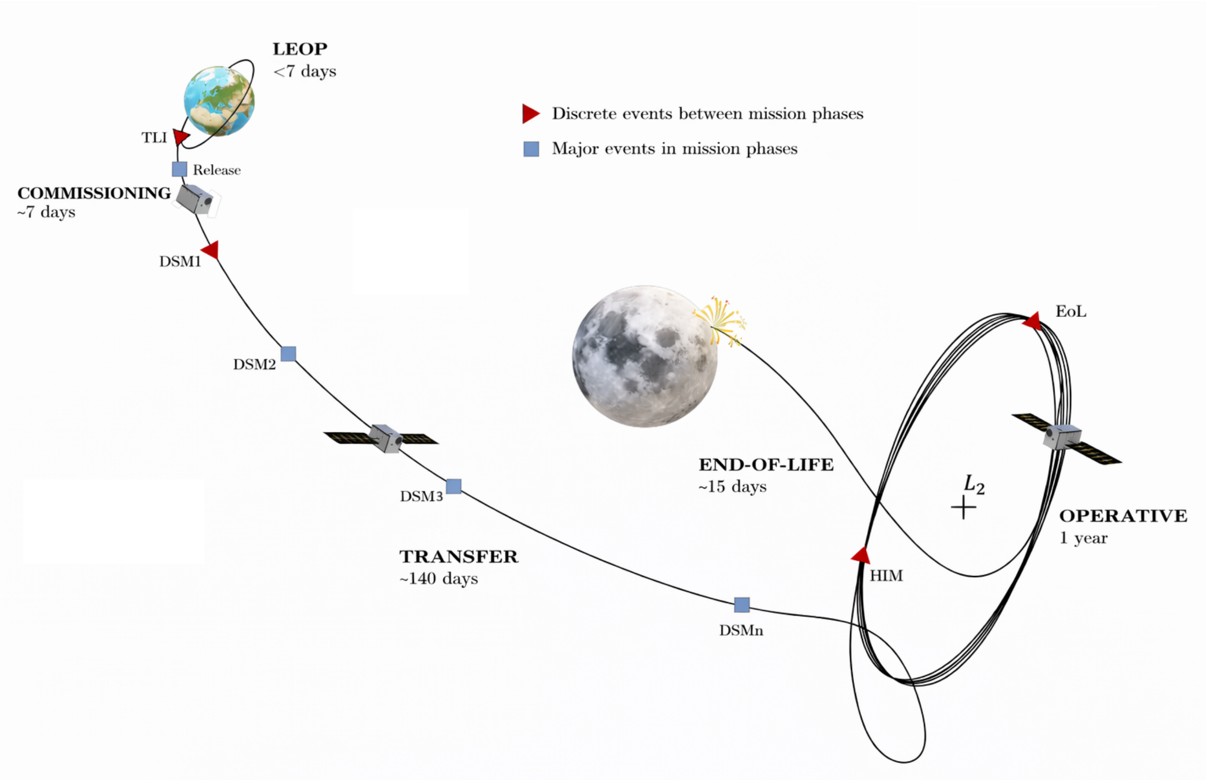

Figure 4.1: LUMIO design reference mission [61].

4.1. Mission Overview

Observing lunar impacts directly from space yields several benefits over ground-based observations. In particular, ground observers are biased by the atmosphere that reduces the intensity of the light flashes and the lack of good weather conditions makes the observation impossible. Ground based telescopes can only operate during the Earth's night, reducing the observation periods. Moreover, the Moon can be observed only when it is 10-50% illuminated since the flash created by the meteoroid cannot be detected in full-disk illumination. Observing the lunar far side using space-based assets provides a direct solution to these issues, enabling observations that are complementary in both space and time, while also significantly increasing the available observation duration. The objectives of the mission are briefly reported here [61]:

- To perform remote sensing of the lunar far side surface, performing astronomical observations not achieved yet.
- To demonstrate deployment and autonomous operation of CubeSats in lunar environment.
- To demonstrate miniaturization of optical instrumentation and associated technology in the lunar environment.
- To conduct observation of the lunar surface to detect meteoroid flashes, characterizing their flux, energies and sizes.
- To complement observations achievable via ground-based facilities, providing a better understanding of the meteoroid environment.

The LUMIO satellite is switched on after the deployment by the carrier, which occurs after the Trans-Lunar Injection (TLI) that places it into a WSB transfer toward the Moon. After de-tumbling, deployment of the solar arrays and the commissioning of all subsystems, the spacecraft has a controlled attitude. During the transfer, several Deep Space Maneuvers (DSMs) and a final Halo Injection Maneuver (HIM) are performed. The operative orbit is a Quasi-Halo one, obtained from the CRTBP Halo with a $C_j = 3.09$. For the interested reader, a detailed analysis of the orbit design for LUMIO is carried out in the work of D. A. Dei Tos and F. Topputo [10]. The operative phase is expected to last 1 year in which Science Cycle and the Navigation&Engineering Cycle are repeated continuously every 2 orbits. The Science Cycle has the aim to process science images and calibration images, compressing them. During the Navigation&Engineering Cycle the link for communication, orbit determination and downlink of the scientific product shall be established. This link serves also for the uplink of commands and maneuver planning. After the 1-year operations period, the decommission of all subsystems and the end of life maneuver are performed.

As anticipated in Sec. 3.2, the baseline station-keeping strategy chosen is the TPA. In the next sections, the assumptions and modeling choices adopted for the station-keeping analysis are first introduced, followed by the detailed implementation of the TPA within a Monte Carlo framework.

4.1.1. Knowledge Analysis

The knowledge represents the difference between the estimated trajectory and the real one and is of paramount importance for the station-keeping analysis. The state estimates are updated in a sequential fashion, up to the final epoch of the OD phase. In order to account for flight dynamics and maneuver planning operations, a 48 hours Turn-Around Time (TAT) is considered. During this time gap data are sent from LUMIO to ground, an OD solution is produced, commands for the spacecraft are generated and, eventually, the data are uploaded to LUMIO.

The assumptions considered are [61]:

- The OD is performed exclusively on the nominal trajectory.
- The cut-off time considered before maneuvers is 2 days.
- The OI error and the OD error are selected in accordance with existing applications, relatable to LUMIO.
- A component-wise thrust error of 1% in magnitude is considered.
- The value of 5 mm/s is the lowest possible impulse given by the thrusters, therefore, under this threshold, the maneuver is not executed.

The value of these parameters, implemented in the station-keeping analysis are:

Orbit Injection Error:	
Position total error:	0.7 km
Velocity total error:	0.7 cm/s
Orbit Determination Error:	
Position total error:	0.7 km
Velocity total error:	0.7 cm/s
Manoeuvre Execution Error:	
Δv component error	1%

Table 4.1: Standard deviation of LUMIO's operation errors.

4.1.2. TPA implementation: Monte Carlo Analysis

This section describes the implementation of the Target Point Approach (TPA) adopted for the station-keeping of the reference orbit. The strategy is implemented within a Monte Carlo framework in order to account for navigation uncertainties and maneuver execution errors to assess the robustness of the approach under realistic operational conditions.

The algorithm implemented is based on the Algorithm 4.1:

Algorithm 4.1 Target Point Approach (TPA) for station-keeping cost estimation along a reference Quasi-Halo orbit.

```
function DVSK($t_0, t_f, \Delta t_v, \Delta t_c, \Delta t_i, \sigma_{OI}^2, \sigma_{OD}^2, \sigma_{EX}^2, Q, R$)
    $t \leftarrow t_0$
    $\boldsymbol{\varepsilon}_{OI} \sim \mathcal{N}(0, \sigma_{OI}^2)$                              ▷ Generate OI error
    $\delta \boldsymbol{x}_{\text{true}} \leftarrow \boldsymbol{\varepsilon}_{OI}$
    while $t \leq t_f$ and $\|\delta \boldsymbol{x}_{\text{true}}\| \leq 10\,000$ km do
        $t_v \leftarrow t + \Delta t_v$
        $t_c \leftarrow t_v - \Delta t_c$
        $t_i \leftarrow t + \Delta t_i$
        $\boldsymbol{x}_{c,\text{true}} \leftarrow$ Propagation($t \rightarrow t_c$)
        $\delta \boldsymbol{x}_{\text{true}} \leftarrow \boldsymbol{x}_{c,\text{true}} - \boldsymbol{x}_{c,\text{ref}}$
        $\boldsymbol{\varepsilon}_{OD} \sim \mathcal{N}(0, \sigma_{OD}^2)$                          ▷ Generate OD error
        $\delta \boldsymbol{x}_c \leftarrow \delta \boldsymbol{x}_{\text{true}} + \boldsymbol{\varepsilon}_{OD}$
        $\delta \boldsymbol{x}_c \leftarrow [\delta \boldsymbol{r}_c;\ \delta \boldsymbol{v}_c]$
        $\Delta \boldsymbol{v} \leftarrow \sum_{i=1}^{N_{PT}} (\alpha_i\, \delta \boldsymbol{r}_c + \beta_i\, \delta \boldsymbol{v}_c)$          ▷ Maneuver planning Eq. (3.8)
        if $\|\Delta \boldsymbol{v}\| \leq \Delta V_{\min}$ then
            $\Delta \boldsymbol{v} \leftarrow \mathbf{0}_{3\times 1}$
        end if
        $\boldsymbol{x}_{v,\text{true}} \leftarrow$ Propagation($t_c \rightarrow t_v$)
        $\delta \boldsymbol{x}_{\text{true}} \leftarrow \boldsymbol{x}_{v,\text{true}} - \boldsymbol{x}_{v,\text{ref}}$
        $\boldsymbol{\varepsilon}_{EX} \sim \mathcal{N}(0, \sigma_{EX}^2)$                     ▷ Generate execution error
        $\Delta \boldsymbol{v} \leftarrow \Delta \boldsymbol{v} + \Delta \boldsymbol{v} \circ \boldsymbol{\varepsilon}_{EX}$                  ▷ Hadamard product
        $\delta \boldsymbol{x}_{\text{true}} \leftarrow \delta \boldsymbol{x}_{\text{true}} + [\mathbf{0}_{3\times 1};\ \Delta \boldsymbol{v}]$
        $t \leftarrow t_v$
    end while
end function
```

Fig. 4.2 illustrates the reference timeline adopted for the station-keeping operations along the orbit. The maneuvers are scheduled at regular intervals of 7 days. Each maneuver is preceded by an OD cut-off, occurring 2 days before the execution.

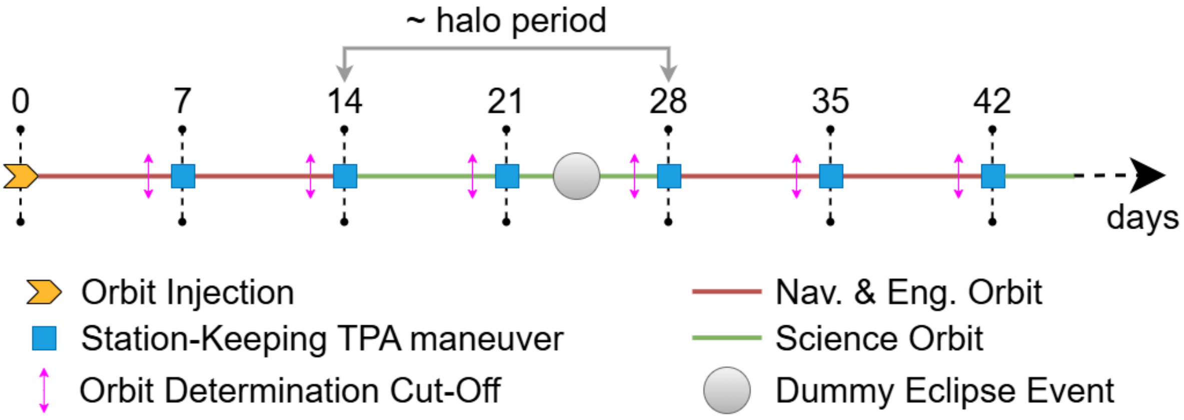

Figure 4.2: Disposition of the station-keeping maneuvers for LUMIO.

The fine-tuned parameter values for the station-keeping analysis are shown in Table 4.2. The target points are located at 35 and 42 days after OI and any subsequent station-keeping maneuver. Eventually, having the eigenspectrum of Q a larger magnitude of R_i's one, the optimization gives more importance to the position error with respect to the $\boldsymbol{\Delta v}$ cost.

Parameter	**Symbol**	**Value**
1^{st} target point location	Δt_1	35 [days]
2^{nd} target point location	Δt_2	42 [days]
$\boldsymbol{\Delta v}$ weight matrix	Q	$10^{-1} I_{3\times3}$ [~]
$\delta \boldsymbol{r_1}$ weight matrix	R_1	$10^{-2} I_{3\times3}$ [~]
$\delta \boldsymbol{r_2}$ weight matrix	R_2	$10^{-2} I_{3\times3}$ [~]

Table 4.2: TPA parameters.

The following results summarize the outcomes of a Monte Carlo campaign, aimed at validating the TPA. The analysis, based on 1000 runs, quantifies the impact of injection, navigation and execution errors, providing statistical results on the expected operational performances.

Table 4.3 displays the 1-year statistics in terms of $\boldsymbol{\Delta v}$ mean cost, μ, standard deviation, σ and 99.73% confidence value, 3σ. Figure 4.3 gives a visual representation of the Monte Carlo results.

μ [m/s]	σ [m/s]	3σ value [m/s]	fails [%]
14.6557	1.9709	20.9642	0

Table 4.3: Monte Carlo results.

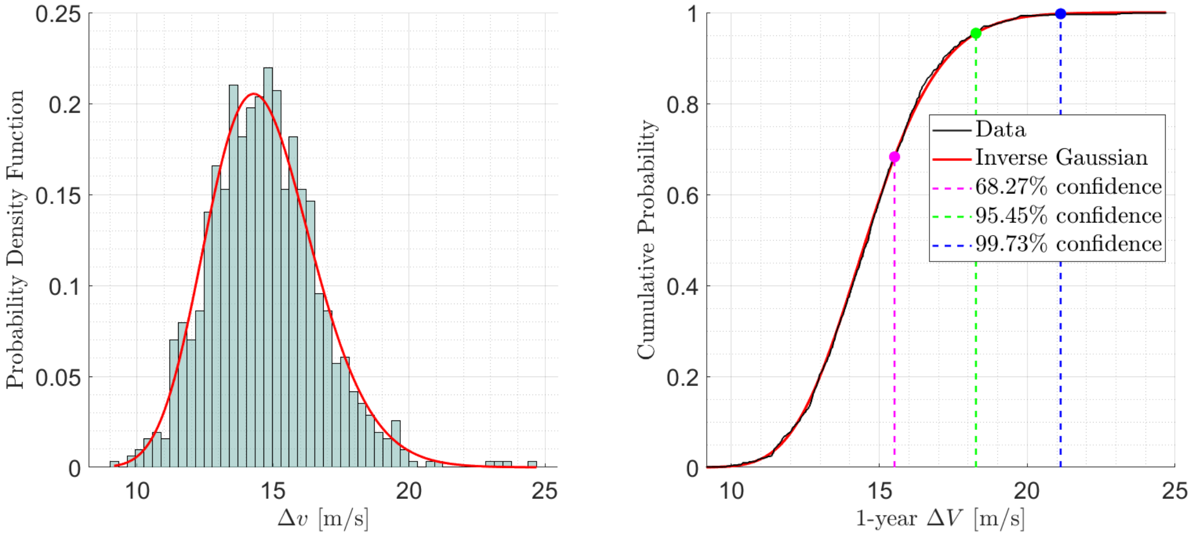

Figure 4.3: One year TPA station-keeping Monte Carlo results. On the left the $\boldsymbol{\Delta v}$ distribution, on the right the cumulative probability.

4.2. Geometric Analysis

In this section, the geometric characteristics of the LUMIO operational orbit are presented, with the purpose of better understanding and detecting eclipse events. In particular, eclipse occurrences are highly variable in both timing and duration, and their depth strongly depends on the relative geometry between the spacecraft, the primaries, and the Sun. Eclipses may occur at different epochs depending on the selected orbit injection date, making their prediction a critical aspect for avoidance techniques.

4.2.1. Body-Centered Sun–Body Rotating Frames

Since the reference trajectory is known, it can be conveniently transformed in properly defined rotating reference frames centered on the primary bodies, the Earth and the Moon. In this way the relative geometry between the spacecraft, the osculating body, and the Sun can be described in a clear and intuitive manner. The rotation procedure is extensively reported in Appendix B. Within these frames, the Sun-body line is fixed, coincident with the x-axis, allowing eclipse conditions to be expressed through simple geometric relations

involving the spacecraft position.
The data required to perform the transformation (e.g. Sun and primary bodies position and velocity) is recovered through SPICE. The LUMIO reference trajectory obtained in Sec. 2.3.2 is transformed in Earth Centered Sun-Earth Rotating frame (ECSER) and Moon Centered Sun-Moon Rotating frame (MCSMR) and presented in Fig. 4.4.

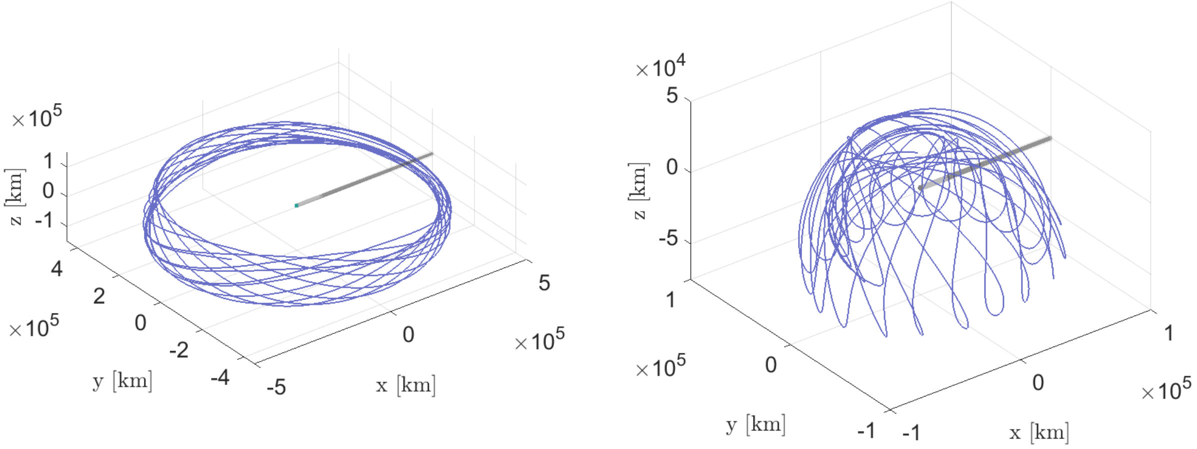

Figure 4.4: Reference trajectory @ ECSER (left) and @ MCSMR (right). The shadow generated by the primaries is represented in gray.

4.2.2. Conical Shadow Model

The Conical Shadow Model [11, 54, 57] is employed to describe the shadow effects of Earth and Moon on the LUMIO spacecraft. This simple model provides reliable results while maintaining high computational efficiency and effectively distinguishing between the umbra and penumbra regions.

A schematic representation is given in Fig. 4.5.

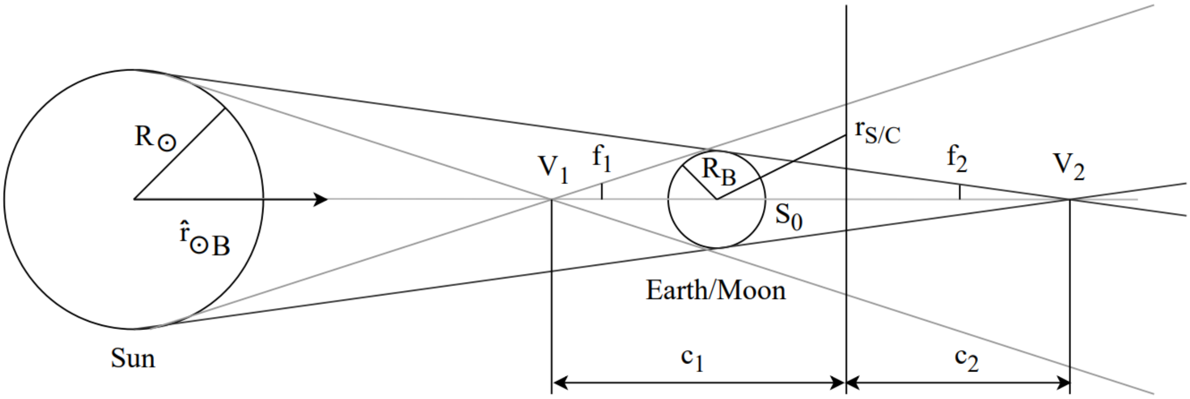

Figure 4.5: Conical Shadow Model scheme [11].

The shadow factor, defined as:

$$\nu = \frac{S}{S_\odot}, \tag{4.1}$$

describes the ratio between the visible area of the Sun S and the total apparent area $S_\odot$. Then, to define the eclipse condition:

$$S_0 = \hat{\boldsymbol{r}}_{\odot B} \cdot \boldsymbol{r}_{S/C}, \tag{4.2}$$

where $\hat{\boldsymbol{r}}_{\odot B}$ represents the unit vector that goes from the Sun to the primary body and $\boldsymbol{r}_{S/C}$ represents the position vector of the spacecraft with respect to the center of the primary body.

If the value of S_0 is less or equal than 0, the satellite lies on the sunward side hence no eclipses can occur. On the other hand, if S_0 is greater than 0 a deeper analysis must be performed to verify the eclipse condition.

The cone angle associated to penumbra f_1, and the one associated to umbra f_2 can be computed as:

$$\sin f_1 = \frac{R_\odot + R_B}{D_{B\odot}}, \qquad \sin f_2 = \frac{R_\odot - R_B}{D_{B\odot}}. \tag{4.3}$$

Where $R_\odot$ is the radius of the Sun, R_B is the radius of the primary occulting body and $D_{B\odot}$ is the distance between the primary and the Sun.

The radius of penumbra and umbra are then defined as:

$$l_1 = c_1 \tan f_1, \qquad l_2 = c_2 \tan f_2, \tag{4.4}$$

where:

$$c_1 = S_0 + \frac{R_B}{\sin f_1}, \qquad c_2 = S_0 - \frac{R_B}{\sin f_2}. \tag{4.5}$$

The radius of the spacecraft on the reference plane described by the umbra and penumbra circles is:

$$l_{S/C} = \sqrt{r_{S/C}^2 - S_0^2}. \tag{4.6}$$

The three different occulting conditions are summed up in Table 4.4.

This formulation blends perfectly with the previously rotated trajectory. By computing the radius of umbra and penumbra for each occulting body, it can be detected precisely when the spacecraft intersects the umbra or penumbra region by simply analyzing the position vector of the spacecraft.

Condition	**Zone**	**Description**
$l_{S/C} < l_2$, $\nu = 0$	Umbra	Satellite completely in shadow
$l_2 \leq l_{S/C} < l_1$, $0 < \nu < 1$	Penumbra	Satellite partially illuminated
$l_1 \leq l_{S/C}$, $\nu = 1$	Illuminated	Satellite fully illuminated

Table 4.4: Eclipse condition cases for a satellite.

4.2.3. Eclipses Detection and Validation

The methodology formulated in Sec. 4.2.2 is applied to the LUMIO reference trajectory computed in Sec. 2.3.2. The spacecraft state is propagated along the nominal trajectory and expressed in the appropriate Sun–body rotating frames, allowing the eclipse conditions to be evaluated. For each occulting body, eclipse events are detected by verifying whether the spacecraft position lies within the umbra or penumbra regions.

The eclipse events, with their duration, are represented in Fig. 4.6 while, in Fig. 4.7, a close-up view of the passage of the spacecraft near the shadow regions is displayed.

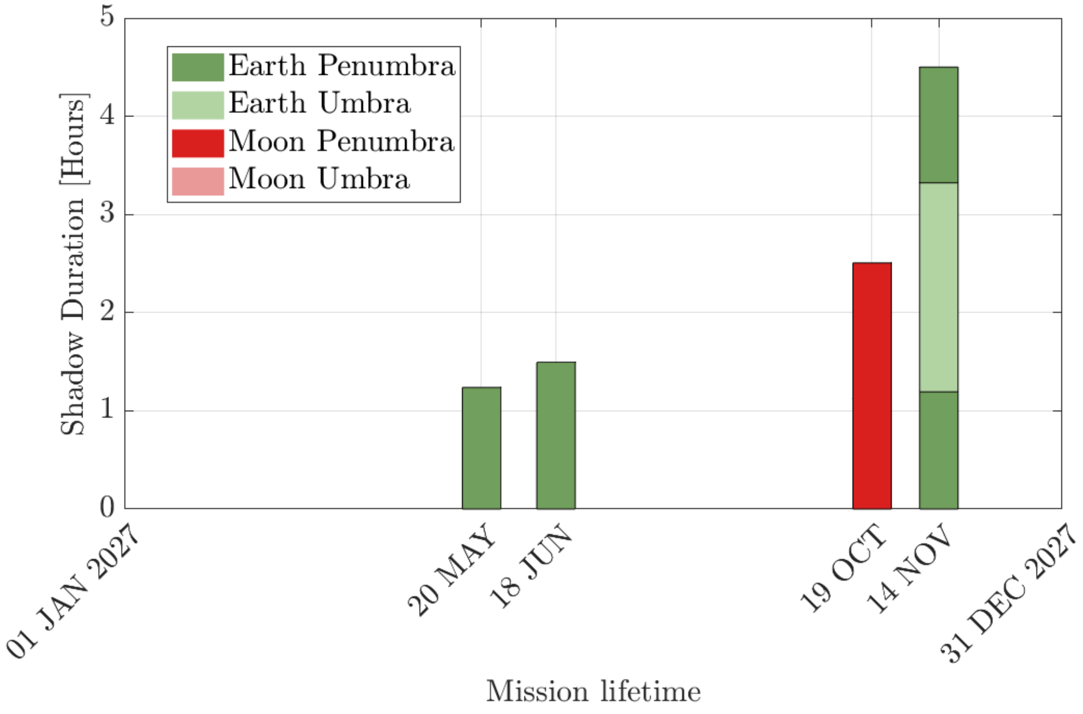

Figure 4.6: Lighting condition of LUMIO Quasi-Halo reference trajectory.

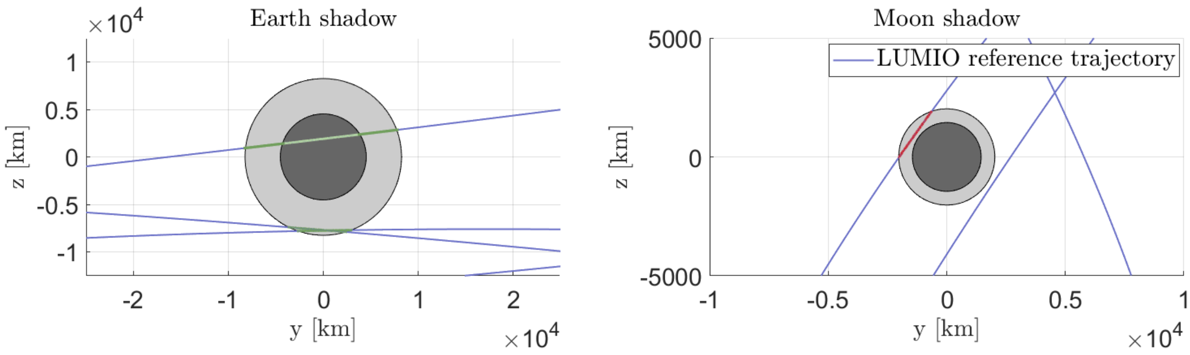

Figure 4.7: Eclipses close-up views @ ECSER (left) and @ MCSMR (right).

Eventually, the detected eclipse events are validated through comparison with the results obtained using the SPICE `gfoclt` function, which is designed to identify occultation events between celestial bodies. The comparison results are reported in Table 4.5.

Event	**Start (UTC)**	**End (UTC)**	Δt_{start} [s]	Δt_{end} [s]	Δt_{dur} [s]	Δt_{dur} [%]
E01.cs	May 20 10:15:07	May 20 11:28:48	–	–	–	–
E01	May 20 10:14:54	May 20 11:29:11	−13	+23	+36	+0.81
E02.cs	Jun 18 15:09:44	Jun 18 16:38:50	–	–	–	–
E02	Jun 18 15:09:29	Jun 18 16:39:11	−15	+21	+36	+0.67
M01.cs	Oct 19 06:52:33	Oct 19 09:22:56	–	–	–	–
M01	Oct 19 06:52:34	Oct 19 09:22:55	+1	−1	−2	−0.02
E03.cs	Nov 14 12:28:51	Nov 14 16:59:10	–	–	–	–
E03	Nov 14 12:28:59	Nov 14 16:59:08	+8	−2	−10	−0.06

Table 4.5: Comparison between SPICE `gfoclt` and ECSER/MCSMR–based eclipse detections (penumbra–umbra combined). In the table the events labelled as XXX.cs are related to the `gfoclt` function results. The first letter of the label indicates the occulting body (Earth or Moon).

The results highlight the effectiveness and robustness of the methodology followed, whose results differ from the SPICE `gfoclt` output by just a few seconds.

Eclipse events differ in occurrence, duration, and depth depending on the orbit insertion epoch and, consequently, on the selected Quasi-Halo reference trajectory. Additional cases are reported in Appendix A.

5 | Methodology

In this chapter, the methodology formulated to achieve an active eclipse avoidance station-keeping technique for Quasi-Halo orbits is mathematically and conceptually presented. To address the challenges posed by eclipse mitigation in the cislunar environment, this work adopts a constraint-based analytical framework rather than global optimization procedures: the purpose is to build a systematic and deterministic procedure, capable of enforcing eclipse avoidance requirements without relying on extensive parameter searchers and a priori trajectory design. This choice is driven by the strong dependence of eclipse occurrence and depth on the actual injection conditions, fixed by launch constraints. Moreover, traditional optimization techniques are not well-suited because of their sensitivity to initial guesses and long computational costs. Within this context, the KKT framework provides a convenient mathematical tool to enforce hard physical constraints, while retaining computational efficiency and direct controllability on the maneuver schedule.

5.1. KKT Mathematical Framework

Many problems in space mission analysis can be formulated as optimization problems, in which a performance index is minimized while a set of constraints must be respected. Such problems can be expressed in a finite-dimensional setting, for example as a result of a discretization or linearization process. In this case, they assume the form of a Non-Linear Programming (NLP) problem which is characterized by a non-linear objective function and a combination of equality and inequality constraints. The KKT conditions arise in this context as the fundamental mathematical tool that characterizes optimality for constrained NLP problems. The KKT conditions provide a set of algebraic relations that any locally-optimal solution must satisfy [2].

The general NLP problem can be stated as the task of finding the n-vector $\boldsymbol{x} = (x_1, \ldots, x_n)^T$ that minimizes the scalar objective function [2]:

$$\min_{\boldsymbol{x}} F(\boldsymbol{x}), \tag{5.1}$$

subject to the m constraints:

$$\boldsymbol{c}_L \leq \boldsymbol{c}(\boldsymbol{x}) \leq \boldsymbol{c}_U, \tag{5.2}$$

and the simple bounds:

$$\boldsymbol{x}_L \leq \boldsymbol{x} \leq \boldsymbol{x}_U. \tag{5.3}$$

The KKT necessary conditions for $\boldsymbol{x}^*$ to be an optimal point require that [2]:

- $\boldsymbol{x}^*$ is feasible, which means that it respects Eq. (5.2) and Eq. (5.3).
- The Lagrange multipliers $\boldsymbol{\lambda}$ of Eq. (5.2) and $\boldsymbol{\nu}$ of Eq. (5.3) satisfy:

  $$\boldsymbol{g} = \boldsymbol{G}^T\boldsymbol{\lambda} + \boldsymbol{\nu} \tag{5.4}$$

  where $\boldsymbol{g} = \nabla F(\boldsymbol{x}^*)$ is the gradient of the objective function and $\boldsymbol{G} = \nabla \boldsymbol{c}(\boldsymbol{x}^*)$ is the Jacobian of the constraints, both at the optimal point. The latter is defined as KKT stationarity condition.
- The Lagrange multipliers for the inequalities must be non-positive for active upper bounds, zero for strictly satisfied constraints, non-negative for active lower bounds.
- The Jacobian $\boldsymbol{G}$ corresponding to the active constraints must have full row rank.

At the solution $\boldsymbol{x}^*$, some of the constraints are satisfied as equalities, that is:

$$c_i(\boldsymbol{x}^*) = 0 \qquad \text{for} \qquad i \in \mathcal{A}, \tag{5.5}$$

where $\mathcal{A}$ is called the active set. Some constraints, instead, are strictly satisfied, that is:

$$c_i(\boldsymbol{x}^*) > 0 \qquad \text{for} \qquad i \in \mathcal{A}', \tag{5.6}$$

where $\mathcal{A}'$ is called the inactive set. The KKT conditions define first-order optimality for constrained non-linear programs and naturally lead to active-set methods, where only binding constraints are enforced.

Then, following the classical approach, the Lagrangian is defined [2, 60]:

$$\mathcal{L}(\boldsymbol{x}, \boldsymbol{\lambda}) = F(\boldsymbol{x}) - \boldsymbol{\lambda}^T\boldsymbol{c}(\boldsymbol{x}) = F(\boldsymbol{x}) - \sum_{i=1}^{m} \lambda_i \nabla c_i(\boldsymbol{x}) \tag{5.7}$$

Optimality requires that the derivatives of $\mathcal{L}$ with respect to $\boldsymbol{x}$ and $\boldsymbol{\lambda}$ are zero. Thus:

$$\nabla_x \mathcal{L}(\boldsymbol{x}^*, \boldsymbol{\lambda}^*) = \boldsymbol{0}, \tag{5.8}$$

$$\nabla_{\lambda}\mathcal{L}(\boldsymbol{x}^{*},\boldsymbol{\lambda}^{*}) = \mathbf{0}. \tag{5.9}$$

The gradient of $\boldsymbol{\mathcal{L}}$ with respect to $\boldsymbol{x}$ and $\boldsymbol{\lambda}$ can be retrieved:

$$\nabla_{x}\boldsymbol{\mathcal{L}} = \boldsymbol{g} - \boldsymbol{G}^{T}\boldsymbol{\lambda} = \nabla F - \sum_{i=1}^{m}\lambda_i \nabla c_i, \tag{5.10}$$

$$\nabla_{\lambda}\boldsymbol{\mathcal{L}} = -\boldsymbol{c}(\boldsymbol{x}). \tag{5.11}$$

These conditions do not distinguish between a point that is a maximum, minimum, or simply a stationary point. The conditions on the curvature of the objective are needed. The Hessian of the Lagrangian is defined as [2, 60]:

$$\boldsymbol{H}_{\mathcal{L}} = \nabla_{x}^{2}\boldsymbol{\mathcal{L}} = \nabla_{x}^{2}F - \sum_{i=1}^{m}\lambda_i \nabla_{x}^{2} c_i, \tag{5.12}$$

and the sufficient condition is:

$$\boldsymbol{v}^{T}\boldsymbol{H}_{\mathcal{L}}\boldsymbol{v} > \mathbf{0}, \tag{5.13}$$

for any vector $\boldsymbol{v}$ in the constraint tangent space.

The final step consists in applying Newton's method to find the values of $(\boldsymbol{x},\boldsymbol{\lambda})$ such that the necessary conditions in Eq. (5.8) and Eq. (5.9) are satisfied. Expanding Eq. (5.10) and Eq. (5.11) with Taylor series yields:

$$\mathbf{0} = \boldsymbol{g} - \boldsymbol{G}^{T}\boldsymbol{\lambda} + \boldsymbol{H}_{\mathcal{L}}\Delta\boldsymbol{x} - \boldsymbol{G}^{T}\Delta\boldsymbol{\lambda}, \tag{5.14}$$

$$\mathbf{0} = -\boldsymbol{c} - \boldsymbol{G}\Delta\boldsymbol{x}. \tag{5.15}$$

After simplification, these equations lead to the linear system called KKT system [2, 60]:

$$\begin{bmatrix} \boldsymbol{H}_{\mathcal{L}} & -\boldsymbol{G}^{T} \\ \boldsymbol{G} & \mathbf{0} \end{bmatrix} \begin{bmatrix} \Delta\boldsymbol{x} \\ \Delta\boldsymbol{\lambda} \end{bmatrix} = \begin{bmatrix} -\boldsymbol{g} \\ -\boldsymbol{c} \end{bmatrix}. \tag{5.16}$$

In this formulation, the Newton's method is based on a linear approximation of the constraints and of the gradients. It can be demonstrated that the system is equivalent to constructing a quadratic model for the quantity that is being optimized [2]. It is important to note that the quadratic approximation is made for the Lagrangian function and not the objective one. Because of the quadratic-linear model the Newton's method converges in one step. The alternative and equivalent formulation of the quadratic objective is then:

$$\mathcal{F}(\boldsymbol{x}) = \boldsymbol{g}^T \Delta\boldsymbol{x} + \frac{1}{2}\Delta\boldsymbol{x}^T \boldsymbol{H}_{\mathcal{L}} \Delta\boldsymbol{x}, \tag{5.17}$$

subject to the active linear constraints:

$$\boldsymbol{G}\Delta\boldsymbol{x} = -\boldsymbol{c}. \tag{5.18}$$

It is straightforward to demonstrate that the optimality conditions for this quadratic-linear optimization subproblem are given by the KKT system of Eq. (5.16) [2].

5.2. Eclipse Avoidance Formulation

The objective of the eclipse avoidance maneuver is to perform a certain number of burns before the detected eclipse event, in such a way that the spacecraft effectively deviates from the reference trajectory, exiting the shadow region. As discussed in Sec. 4.2.3, for a given injection epoch, the eclipse events are fixed over the mission lifetime. Although the actual trajectory never exactly coincides with the reference one, the occurrence and duration of the eclipse events overlap, with discrepancies on the order of a few minutes. This allows the maneuver schedule and control logic to be planned a priori, as well as the computation of all the parameters subsequently used to determine the avoidance maneuvers, including the reference STMs and the outputs of the shadow function (formulated in the next subsection), such as the epoch of the deepest eclipse point and the corresponding state vector. Out of the neighborhood of the eclipses, the choice is to maintain the nominal TPA for the station-keeping of the orbit.

The eclipse avoidance maneuver is formulated as a local two-impulse KKT-based control problem, aimed at mitigating eclipse events by introducing a controlled deviation from the reference trajectory that ensures compatibility with the spacecraft power constraints. The control vector consists of two impulsive velocity corrections applied at predefined maneuver epochs:

$$\boldsymbol{z} = \left[\Delta\boldsymbol{v}_1^T,\, \Delta\boldsymbol{v}_2^T\right]^T \quad \in \mathbb{R}^6. \tag{5.19}$$

The TPA concept is maintained in the formulation of the problem. In particular, one target point is considered. In this formulation, the eclipse constraint is enforced as a hard requirement, while station-keeping is embedded within the objective function. Enforcing the reference orbit softly permits temporary deviations when necessary, enabling effective avoidance of shadow regions.

5.2.1. Shadow Function

The shadow function is introduced to correctly formulate the eclipse constraint. In particular, it aims to provide a continuous and differentiable measure of the spacecraft proximity to the shadow region. The formulation is based on the same procedure as that illustrated in Sec. 4.2.3, which exploit the geometric relationship between the spacecraft, the occulting bodies and the Sun, expressed in a Sun-body aligned reference frame.

A safety margin is explicitly introduced to set a limit to the depth of the eclipse, compatibly with the operational power constraints. The shadow function is defined such that positive values indicate sunlit conditions, while negative ones correspond to eclipse penetration: the more negative, the deeper into the shadow region. Here, no distinction between umbra and penumbra is considered, as they are both objects of mitigation. The pseudo-algorithm is:

Algorithm 5.1 Shadow function for eclipse constraint evaluation.

```
function ShadowFunction($et_0$, $\boldsymbol{x}_{S/C}$, $t$, $g_{\text{safe}}$, type)
    $DU \leftarrow 3.84405 \times 10^5$                              ▷ Distance unit [km]
    $TU \leftarrow 4.34256461$                                       ▷ Time unit [days]
    $et \leftarrow et_0 + t \cdot 86400$                             ▷ Ephemeris time [s]
    $R_E \leftarrow \text{mean}(\text{RADII}(\text{EARTH}))$
    $R_M \leftarrow \text{mean}(\text{RADII}(\text{MOON}))$
    $R_S \leftarrow \text{mean}(\text{RADII}(\text{SUN}))$
    $(\boldsymbol{r}_{\text{ECSER}}, \boldsymbol{r}_{\text{MCSMR}}, f_E, f_M) \leftarrow \dots$
        SunBody_Rot($et$, $\boldsymbol{x}_{S/C}$, $DU$, $TU$, $R_E$, $R_S$, $R_M$)    ▷ Appendix B rotations
    if type = "EARTH" then
        $x_{\text{cut}} \leftarrow \boldsymbol{r}_{\text{ECSER}}(1)$              ▷ Axial coordinate
        $r_{\text{sh}} \leftarrow R_E + x_{\text{cut}} \tan(f_E) + g_{\text{safe}} DU$    ▷ Shadow boundary [km]
        $\rho \leftarrow \sqrt{\boldsymbol{r}_{\text{ECSER}}(2)^2 + \boldsymbol{r}_{\text{ECSER}}(3)^2}$
        $g \leftarrow (\rho - r_{\text{sh}})/DU$
    else if type = "MOON" then
        $x_{\text{cut}} \leftarrow \boldsymbol{r}_{\text{MCSMR}}(1)$
        $r_{\text{sh}} \leftarrow R_M + x_{\text{cut}} \tan(f_M) + g_{\text{safe}} DU$
        $\rho \leftarrow \sqrt{\boldsymbol{r}_{\text{MCSMR}}(2)^2 + \boldsymbol{r}_{\text{MCSMR}}(3)^2}$
        $g \leftarrow (\rho - r_{\text{sh}})/DU$
    end if
    return $g$
end function
```

The function is numerically differentiable with respect to the spacecraft state, using finite differences. The local gradient information is exploited within the formulation of the eclipse constraint in the KKT framework.

5.2.2. Eclipse Constraint

The eclipse constraint is formulated through the scalar output of the shadow function $\boldsymbol{g}$, which quantifies the signed distance of the spacecraft from the penumbra boundary. The eclipse avoidance requirement is therefore imposed as a hard inequality constraint of the form:

$$g(\boldsymbol{x}_e, t_e) \geq g_{\text{safe}} \tag{5.20}$$

The choice of the enforcement epoch t_e and the adopted safety margin is critical. The epoch t_e is defined as the time instant at which the eclipse constraint is imposed. A natural and conservative choice is to select the deepest point of the eclipse event, corresponding to the minimum value obtained by the shadow function output, the $\boldsymbol{g}$ vector. The choice of the g_{safe} factor must ensure that the total eclipse duration is below a certain threshold. The maximum amount of energy that the batteries of LUMIO spacecraft can deliver in shadow conditions is 86.8 Wh. An empirical relationship, provided by the battery manufacturer, is used to correlate the durations of umbra and penumbra phases with the associated energy consumption:

$$42[\text{W}] \cdot t_{\text{penumbra}}[\text{h}] + 71[\text{W}] \cdot t_{\text{umbra}}[\text{h}] < 86.8[\text{Wh}]. \tag{5.21}$$

Assuming to avoid completely umbra regions, the maximum duration of penumbra that the batteries withstand is 2 hours, 4 minutes, and 1 second. As a consequence, the value of g_{safe} can be tuned to respect this threshold.

The eclipse constraint as defined in Eq. (5.20) is intrinsically non-linear, as it depends on non-linear geometry and ephemeris-based position of the primaries. However, in order to be consistent with the KKT framework, the maneuver must be designed locally using linearized dynamics expressed through the STM. Therefore, the constraint is linearized about the reference state at the enforcement epoch, allowing to represent it as a linear inequality in the maneuver variables. In particular, at the i-th maneuver epoch $t_{m,i}$:

$$\delta\boldsymbol{x}(t_{m,i}^-) = \delta\boldsymbol{x}_{m,i}^-, \tag{5.22}$$

and after the impulse:

$$\delta \boldsymbol{x}(t_{m,i}^{+}) = \delta \boldsymbol{x}_{m,i}^{-} + G\Delta \boldsymbol{v}_i, \qquad \text{with} \qquad G := \begin{bmatrix} \boldsymbol{0}_{3\times3} \\ \boldsymbol{I}_{3\times3} \end{bmatrix}. \tag{5.23}$$

Since two impulses are performed, for $t \geq t_{m,2}$:

$$\delta \boldsymbol{x}(t) = \boldsymbol{\Phi}(t_{m,1}, t)\delta \boldsymbol{x}_{m,1}^{-} + \boldsymbol{\Phi}(t_{m,1}, t)G\Delta \boldsymbol{v}_1 + \boldsymbol{\Phi}(t_{m,2}, t)G\Delta \boldsymbol{v}_2. \tag{5.24}$$

The eclipse constraint is then:

$$g(\boldsymbol{x}_e, t_e) \approx g_0 + \nabla \boldsymbol{g}_e^T \delta \boldsymbol{x}(t_e) \geq g_{\text{safe}}. \tag{5.25}$$

Substituting Eq. (5.24) in Eq. (5.25):

$$g_0 + \nabla \boldsymbol{g}_e^T \left[\boldsymbol{\Phi}(t_{m,1}, t_e)\delta \boldsymbol{x}_{m,1}^{-} + \boldsymbol{\Phi}(t_{m,1}, t_e)G\Delta \boldsymbol{v}_1 + \boldsymbol{\Phi}(t_{m,2}, t_e)G\Delta \boldsymbol{v}_2 \right] \geq g_{\text{safe}}. \tag{5.26}$$

Defining:

$$\text{Known term} \qquad \rightarrow \qquad d_{\text{err}} := \nabla \boldsymbol{g}_e^T \boldsymbol{\Phi}(t_{m,1}, t_e)\delta \boldsymbol{x}_{m,1}^{-}, \tag{5.27}$$

$$\text{Sensitivity rows} \qquad \rightarrow \qquad \begin{cases} \boldsymbol{c}_1^T := \nabla \boldsymbol{g}_e^T \boldsymbol{\Phi}(t_{m,1}, t_e)G, \\ \boldsymbol{c}_2^T := \nabla \boldsymbol{g}_e^T \boldsymbol{\Phi}(t_{m,2}, t_e)G, \end{cases} \tag{5.28}$$

the constraint is:

$$\boldsymbol{c}_1^T \Delta \boldsymbol{v}_1 + \boldsymbol{c}_2^T \Delta \boldsymbol{v}_2 \geq g_{\text{safe}} - g_0 - d_{\text{err}}, \tag{5.29}$$

which, in a compact form is:

$$\boldsymbol{a}^T \boldsymbol{z} \geq \psi \qquad \text{with} \qquad \begin{cases} \boldsymbol{a}^T := \left[\boldsymbol{c}_1^T, \boldsymbol{c}_2^T \right] \\ \psi := g_{\text{safe}} - g_0 - d_{\text{err}} \end{cases} \tag{5.30}$$

5.2.3. KKT System

The objective function of the minimization is divided into two parts: one considers and minimizes the deviation at the target point, improving the station-keeping, while the second part directly minimizes the cost of the maneuver.

$$J_{\text{avoid}}(\boldsymbol{z}) = J_{S/K}(\boldsymbol{z}) + J_c(\boldsymbol{z}). \tag{5.31}$$

The first contribution to the cost function is designed to preserve proximity to the reference trajectory, without enforcing exact re-centering during the avoidance phase. One target point is considered: $T_1 = 12$ days. Its position deviation, being included in the objective function, is minimized and can be expressed as a function of the control vector $\boldsymbol{z}$:

$$\delta\boldsymbol{r}(T_1) = \boldsymbol{b}_r + \boldsymbol{A}_1\Delta\boldsymbol{v}_1 + \boldsymbol{A}_2\Delta\boldsymbol{v}_2, \tag{5.32}$$

where:

$$\begin{aligned} \boldsymbol{b}_r &:= \boldsymbol{\Phi}_{rr}(t_{m,1}, T_1)\delta\boldsymbol{r}^-_{m,1} + \boldsymbol{\Phi}_{rv}(t_{m,1}, T_1)\delta\boldsymbol{v}^-_{m,1}, \\ \boldsymbol{A_1} &:= \boldsymbol{\Phi}_{rv}(t_{m,1}, T_1), \\ \boldsymbol{A_2} &:= \boldsymbol{\Phi}_{rv}(t_{m,2}, T_1). \end{aligned} \tag{5.33}$$

The soft station-keeping objective is then written in least-squares form as:

$$J_{S/K} = w_T \left\|\boldsymbol{A}_{S/K}\boldsymbol{z} - \boldsymbol{b}_{S/K}\right\|^2, \qquad \text{with} \qquad \begin{cases} \boldsymbol{A}_{S/K} = \left[\boldsymbol{A}_1,\ \boldsymbol{A}_2\right], \\ \boldsymbol{b}_{S/K} = -\boldsymbol{b}_r. \end{cases} \tag{5.34}$$

Here, w_T is a tuning parameter used to modulate the importance of the target point re-centering during avoidance.

The second part of the objective function directly includes the minimization of the cost of the maneuvers. It also serves as regularizer, improving the numerical conditioning:

$$J_c = \lambda_c \left\|\boldsymbol{z}^2\right\|, \tag{5.35}$$

where $\lambda_c > 0$ is a small coefficient. By construction, this objective function aims to keep the spacecraft close to the reference trajectory at the target and limit the applied $\Delta\boldsymbol{v}$. The overall least-squares problem can be written by stacking the terms of the two contributions to the cost function:

$$\begin{aligned} \boldsymbol{A}_{qp} &:= \left[\sqrt{w_T}\boldsymbol{A}_{S/K},\ \sqrt{\lambda_c}\boldsymbol{I}_{6\times6}\right]^T, \\ \boldsymbol{b}_{qp} &:= \left[\sqrt{w_t}\boldsymbol{b}_{S/K},\ \boldsymbol{0}_{6\times1}\right]^T. \end{aligned} \tag{5.36}$$

Which leads to:

$$J_{\text{avoid}}(\boldsymbol{z}) = \left\|\boldsymbol{A}_{qp}\boldsymbol{z} - \boldsymbol{b}_{qp}\right\|^2. \tag{5.37}$$

Expanding it:

$$J_{\text{avoid}}(\boldsymbol{z}) = \boldsymbol{z}^T\boldsymbol{H}\boldsymbol{z} - 2\boldsymbol{f}^T\boldsymbol{z}, \qquad \text{with} \qquad \begin{cases} \boldsymbol{H} := \boldsymbol{A}_{qp}^T\boldsymbol{A}_{qp}, \\ \boldsymbol{f} := \boldsymbol{A}_{qp}^T\boldsymbol{b}_{qp}. \end{cases} \tag{5.38}$$

Introducing the linearized eclipse constraint this quadratic structure allows to efficiently solve the problem using the KKT system. Re-writing the formulated eclipse avoidance problem in its final form:

$$\min_{\boldsymbol{z}\in\mathbb{R}^6} \quad \boldsymbol{z}^T\boldsymbol{H}\boldsymbol{z} - 2\boldsymbol{f}^T\boldsymbol{z} \qquad \text{such that} \qquad \boldsymbol{a}^T\boldsymbol{z} \geq \psi \tag{5.39}$$

Introducing the Lagrange multiplier, μ, defined later, the KKT system is:

$$\begin{bmatrix} 2\boldsymbol{H} & -\boldsymbol{a} \\ \boldsymbol{a}^T & 0 \end{bmatrix} \begin{bmatrix} \boldsymbol{z} \\ \mu \end{bmatrix} = \begin{bmatrix} 2\boldsymbol{f} \\ \psi \end{bmatrix}. \tag{5.40}$$

5.2.4. Active-Set Logic

In the implemented solver, the hard eclipse constraint is handled through an active-set logic that exploits the analytical KKT conditions. The candidate solutions are constructed by considering the two possible active sets: no active constraint, and active eclipse constraint.

In the first case, the solution $\boldsymbol{z}_{a,0}$ is the unconstrained minimizer of the quadratic cost:

$$\boldsymbol{z}_{a,0} = \boldsymbol{H}^{-1}\boldsymbol{f}, \tag{5.41}$$

which is feasible if it satisfies the linearized eclipse constraint $\boldsymbol{a}^T\boldsymbol{z}_0 \geq \psi$.

If the unconstrained solution violates the eclipse requirement, the constraint is enforced as active and the KKT stationarity condition is imposed with one multiplier μ:

$$2\boldsymbol{H}\boldsymbol{z} - 2\boldsymbol{f} - \mu\boldsymbol{a} = 0, \qquad \text{with} \qquad \mu \geq 0. \tag{5.42}$$

Solving for $\boldsymbol{z}$ yields the closed-form solution:

$$\boldsymbol{z}_{a,1} = \boldsymbol{H}^{-1}\boldsymbol{f} + \frac{1}{2}\mu\boldsymbol{H}\boldsymbol{a} \tag{5.43}$$

The value of μ is obtained by enforcing the feasibility condition:

$$\mu = \frac{2\left(\psi - \boldsymbol{a}^T\boldsymbol{H}^{-1}\boldsymbol{f}\right)}{\boldsymbol{a}^T\boldsymbol{H}^{-1}\boldsymbol{a}} \tag{5.44}$$

This candidate is accepted if μ is non-negative, while the constraint is satisfied by construction.

Eventually, among the feasible candidates, the algorithm selects the one that yields the minimum of the objective function $J_{\text{avoid}}(\boldsymbol{z})$. If no feasible candidate is found, the algorithm falls back on the unconstrained solution and flags the non-feasibility of the problem.

5.2.5. Maneuver Scheduling

The avoidance maneuver is formulated as a two-impulse correction, applied at two predefined times. In particular, the idea behind this selection is to act a certain amount of time before the known eclipse's epoch, in order to gradually deviate from the reference trajectory. Acting too close to the eclipse event results in very large impulsive maneuvers that may destabilize the trajectory, whereas acting too early generally leads to an ineffective avoidance. This happens because of the linearized constraint and the linearized implementation of the dynamics through STMs which for long time spans are not accurate. Acting too far from the eclipse may lead to the satisfaction of the linearized constraint, but in the non-linear high-fidelity propagation the spacecraft still falls into the shadow region. Moreover, during the avoidance phase, the nominal TPA station-keeping is not operational: maintaining it active would cancel the sought deviation from the nominal trajectory.

With a trial-and-error approach, the two maneuver epochs are chosen as 6 and 12 days before the deepest eclipse epoch. A schematic representation of the avoidance schedule is given in Fig. 5.1.

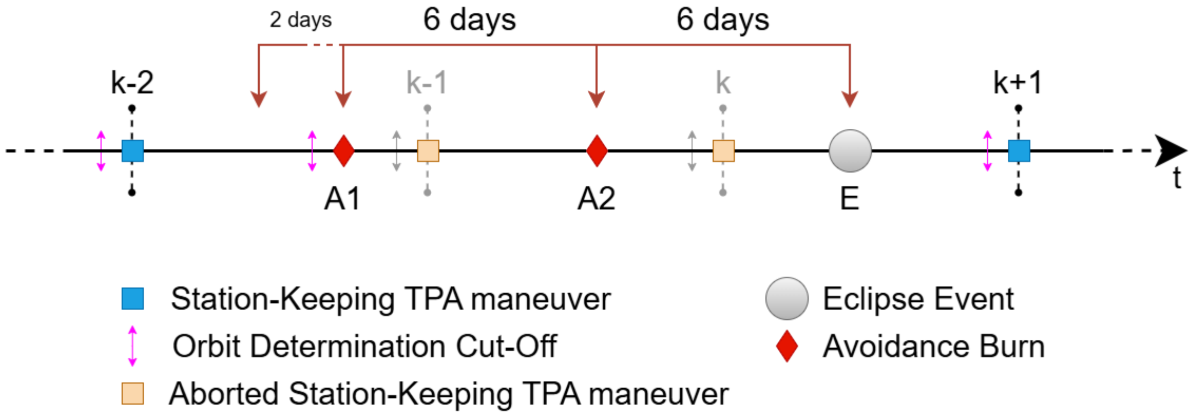

Figure 5.1: Avoidance maneuvers schedule.

As can be appreciated in Fig. 5.1, in the range between the eclipse event epoch (E) and the 14 days before it, nominal station-keeping maneuvers are aborted (e.g. maneuver k and $k-1$ in the figure).

5.3. Recovery Nominal Orbit Formulation

As a consequence of the intended effect of the avoidance maneuvers, the spacecraft deviates in both position and velocity from the reference trajectory, allowing the exit from the shadow region. The resulting state deviation naturally increases with the depth of the eclipse event. Being the dynamic environment intrinsically unstable, this deviation will surely increase if not treated immediately, pushing the satellite even further from the nominal orbit. Recovery maneuvers are therefore designed to steer the spacecraft back to the vicinity of the reference trajectory, ensuring the effectiveness of the nominal station-keeping TPA strategy for subsequent maneuvers.

Rather than enforcing an exact return to the nominal orbit, the formulated constraint requires a future point along the trajectory to lie within a bounded neighborhood of the reference orbit, which resembles a tube-shaped region: inside it, the linearized dynamics hold. This is the condition necessary to ensure the proper functioning of the TPA-based station-keeping strategy. Moreover, enforcing a complete cancellation of the state deviation would result in a higher control cost.

To retain computational efficiency and avoid iterative optimization algorithms, recovery maneuvers are designed in the same KKT framework as the avoidance ones. The control variable is $\boldsymbol{z}$ of Eq. (5.19) and following the same logic, the cost function penalizes both the residual position error at the target and the overall control effort. The linearity tube constraint, if necessary, is imposed as a hard constraint providing a strict safety bound. The active-set strategy is employed to evaluate whether the tube constraint is binding the solution, or the unconstrained one is sufficient to ensure the trajectory to lie inside the linear validity region.

5.3.1. Linearity Tube Constraint

The linearity tube defines a bounded region in the vicinity of the reference trajectory within which the STM remains a reliable approximation of the evolution of the flow. This region is characterized by a scalar radius $\rho(t^*)$, where t^* is the target time. The tube therefore defines the set of admissible position deviations:

$$\left\|\delta\boldsymbol{r}(t^*)\right\| \leq \rho(t^*). \tag{5.45}$$

The value of the tube radius is not arbitrarily chosen. In particular, along the nominal orbit, this boundary region shrinks and expands as function of the local dynamical environment. Such behavior is influenced by the local stability characteristics of the flow and non-linear dynamics, making the tube size intrinsically nonuniform and not known in advance. An idealized representation of the linearity tube is given in Fig. 5.2.

The value of the tube radius is determined statistically through an offline Monte Carlo procedure. In particular, since the epoch of interest t^* is known, an a priori analysis can be performed. At the recovery maneuver epoch, random perturbations are applied to the state of the spacecraft, which is then propagated with both non-linear dynamics and the linear STM model. By comparing the two outcomes at the target time t^*, a statistical estimate of the linearization error is obtained. The largest admissible deviation for which a prescribed percentile ($2\sigma \approx 95.45\%$) of the linearization error remains below a given tolerance defines the tube radius. This tolerance is chosen in accordance to the residuals of the TPA: since the latter is a STM-based method, it is assumed that its residuals are a good measure of the linearity threshold which is eventually set at $\varepsilon \approx 10^{-5}$ in dimensionless unit. The pseudo-algorithm for the tube radius computation is reported here.

Algorithm 5.2 Linearity tube radius computation at t^*.

```
function TubeRadius($\boldsymbol{x}_v^{\text{ref}}$, $\boldsymbol{x}_{t^*}^{\text{ref}}$, $\boldsymbol{\Phi}(t_v, t^*)$, $\{\rho_i\}_{i=1}^{N}$, $N_{\text{MC}}$, $\varepsilon$, $p$)
    for $i = 1$ to $N$ do                                                        ▷ Candidate radii
        for $k = 1$ to $N_{\text{MC}}$ do
            $\boldsymbol{u} \leftarrow \text{randn}(3)$                          ▷ Random direction
            $\boldsymbol{u} \leftarrow \boldsymbol{u}/\|\boldsymbol{u}\|$        ▷ Unit vector
            $\delta\boldsymbol{r}_{t^*} \leftarrow \rho_i\,\boldsymbol{u}$      ▷ Target position deviation
            $\boldsymbol{B} \leftarrow \boldsymbol{\Phi}_{rv}(t_v, t^*)$        ▷ Position–velocity STM block
            $\delta\boldsymbol{v}_0 \leftarrow \boldsymbol{B}^{-1}\delta\boldsymbol{r}_{t^*}$   ▷ Required initial velocity deviation
            $\delta\boldsymbol{x}_0 \leftarrow [\,\boldsymbol{0};\, \delta\boldsymbol{v}_0\,]$  ▷ Initial state perturbation
            $\delta\boldsymbol{r}_{t^*}^{\text{nl}} \leftarrow \text{rnbpOrbit}(\boldsymbol{x}_v^{\text{ref}} + \delta\boldsymbol{x}_0)$   ▷ Nonlinear propagation
            $\delta\boldsymbol{r}_{t^*}^{\text{lin}} \leftarrow \Big(\boldsymbol{\Phi}(t_v, t^*)\delta\boldsymbol{x}_0\Big)_{1:3}$   ▷ Linear prediction
            $e_k \leftarrow \|\delta\boldsymbol{r}_{t^*}^{\text{nl}} - \delta\boldsymbol{r}_{t^*}^{\text{lin}}\|$   ▷ Linearization error
        end for
        $e_p(\rho_i) \leftarrow \text{percentile}_p(\{e_k\})$                   ▷ $p$-th percentile error
    end for
    $\rho_{t^*} \leftarrow \max\{\rho_i : e_p(\rho_i) \leq \varepsilon\}$        ▷ Admissible tube radius
    return $\rho_{t^*}$
end function
```

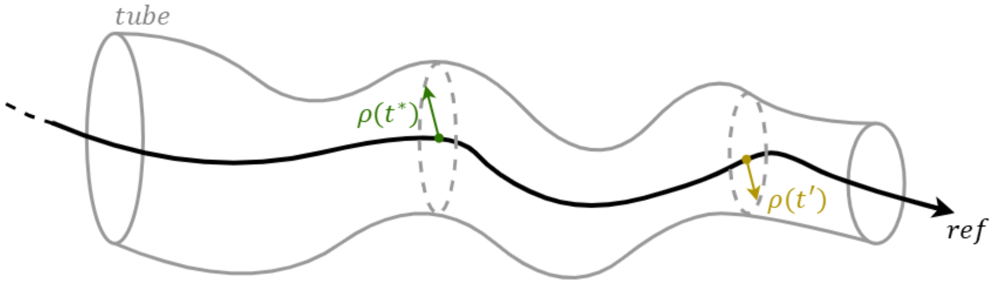

Figure 5.2: Linearity tube representation.

When enforcing the linearity tube constraint within the computation of the recovery burns, the exact nonlinear inequality in Eq. (5.45) cannot be used in the KKT framework because it is written as a nonconvex constraint. To preserve analytical tractability, the tube constraint is therefore projected on one direction only. Specifically, let:

$$P_r := [\boldsymbol{I}_{3\times3}, \boldsymbol{0}_{3\times3}]^T, \qquad \text{so that} \qquad \delta\boldsymbol{r} = P_r\delta\boldsymbol{x}. \tag{5.46}$$

Then, the position deviation at the epoch t^*:

$$\delta\boldsymbol{r}_{t^*} = P_r\boldsymbol{\Phi}(t_{m,1}, t^*)\delta\boldsymbol{x}_{m,1}^- + P_r\boldsymbol{\Phi}(t_{m,1}, t^*)G\Delta\boldsymbol{v}_1 + P_r\boldsymbol{\Phi}(t_{m,2}, t^*)G\Delta\boldsymbol{v}_2, \tag{5.47}$$

where G is the same as in Eq. (5.23). Defining:

$$\begin{aligned} \boldsymbol{A}_1 &:= P_r\boldsymbol{\Phi}(t_{m,1}, t^*)G, \\ \boldsymbol{A_2} &:= P_r\boldsymbol{\Phi}(t_{m,2}, t^*)G, \\ \boldsymbol{b}_r &:= P_r\boldsymbol{\Phi}(t_{m,1}, t^*)\delta\boldsymbol{x}_{m,1}^-, \end{aligned} \tag{5.48}$$

yields:

$$\delta\boldsymbol{r}_{t^*} = \boldsymbol{b}_r + \boldsymbol{A}_1\Delta\boldsymbol{v}_1 + \boldsymbol{A}_2\Delta\boldsymbol{v}_2 = \boldsymbol{b}_r + [\boldsymbol{A}_1, \boldsymbol{A}_2]\,\boldsymbol{z}, \tag{5.49}$$

with $\boldsymbol{z}$ the same control vector, as in Eq. (5.19). The unconstrained recovery solution is first computed and the corresponding predicted deviation direction at the epoch t^* is evaluated. The unit vector, aligned with this unconstrained expansion of the flow, is the direction onto which the tube is projected. Let $\boldsymbol{z}_{r,0}$ be the unconstrained solution, the corresponding deviation is:

$$\delta\boldsymbol{r}_{t^*}^{\text{unc}} = \boldsymbol{b_r} + [\boldsymbol{A}_1, \boldsymbol{A}_2]\,\boldsymbol{z}_{r,0} \tag{5.50}$$

Then, the projection direction:

$$\hat{\boldsymbol{n}} = \frac{\delta \boldsymbol{r}_{t^*}^{\text{unc}}}{||\delta \boldsymbol{r}_{t^*}^{\text{unc}}||}. \tag{5.51}$$

The projected linearity tube constraint is:

$$\hat{\boldsymbol{n}}^T (\boldsymbol{b}_r + \boldsymbol{A}_1 \Delta \boldsymbol{v}_1 + \boldsymbol{A}_2 \Delta \boldsymbol{v}_2) \leq \rho_{t^*}, \tag{5.52}$$

and defining:

$$\boldsymbol{d}_1^T := \hat{\boldsymbol{n}}^T \boldsymbol{A}_1, \qquad \boldsymbol{d}_2^T := \hat{\boldsymbol{n}}^T \boldsymbol{A}_2, \qquad \beta := \rho_{t^*} - \hat{\boldsymbol{n}}^T \boldsymbol{b}_r, \tag{5.53}$$

it can be written in the compact form:

$$\boldsymbol{b}^T \boldsymbol{z} \leq \beta \qquad \text{with} \qquad \boldsymbol{b}^T := \left[\boldsymbol{d}_1^T, \boldsymbol{d}_2^T\right]. \tag{5.54}$$

This approximation guarantees that the recovered state remains inside the linearity region while preserving the framework of the optimization problem.

5.3.2. KKT System

The objective function for the recovery maneuvers is defined in the same way of the avoidance ones. In particular, it penalizes the residual position deviation at the recovery target epoch t^* in a soft manner, together with the minimization of the maneuver magnitudes. The cost function is written as:

$$J_{\text{rec}}(\boldsymbol{z}) = J_{S/K} + J_c, \tag{5.55}$$

where:

$$J_{S/K} = w_T \left\| \boldsymbol{A}_{S/K} \boldsymbol{z} - \boldsymbol{b}_{S/K} \right\|^2, \qquad \text{with} \qquad \begin{cases} \boldsymbol{A}_{S/K} = [\boldsymbol{A}_1,\ \boldsymbol{A}_2], \\ \boldsymbol{b}_{S/K} = -\boldsymbol{b}_r. \end{cases} \tag{5.56}$$

And:

$$J_c = \lambda_c \left\| \boldsymbol{z}^2 \right\|. \tag{5.57}$$

By stacking the terms and following the same procedure of Sec. 5.2.3, the cost function assumes the least-squared formulation:

$$J_{\text{rec}}(\boldsymbol{z}) = \boldsymbol{z}^T \boldsymbol{W} \boldsymbol{z} - 2\boldsymbol{p}^T \boldsymbol{z}, \qquad \text{with} \qquad \begin{cases} \boldsymbol{W} := \boldsymbol{A}_{qp}^T \boldsymbol{A}_{qp}, \\ \boldsymbol{p} := \boldsymbol{A}_{qp}^T \boldsymbol{b}_{qp}. \end{cases} \tag{5.58}$$

Again, thanks to the formulation of the linearity tube constraint, this quadratic structure can efficiently be solved with the aid of the KKT system. The final form of the recovery problem is:

$$\min_{\boldsymbol{z}\in\mathbb{R}^6} \quad \boldsymbol{z}^T\boldsymbol{W}\boldsymbol{z} - 2\boldsymbol{p}^T\boldsymbol{z} \qquad \text{such that} \qquad \boldsymbol{b}^T\boldsymbol{z} \leq \beta. \tag{5.59}$$

Introducing the Langrange multiplier, ν, defined later, the KKT system is:

$$\begin{bmatrix} 2\boldsymbol{W} & \boldsymbol{b} \\ \boldsymbol{b}^T & 0 \end{bmatrix} \begin{bmatrix} \boldsymbol{z} \\ \nu \end{bmatrix} = \begin{bmatrix} 2\boldsymbol{p} \\ \beta \end{bmatrix}. \tag{5.60}$$

5.3.3. Active-Set Logic

The active-set logic is again exploited to determine the optimal solution. The formulation involves two candidate solutions, the unconstrained one and the linearity-tube enforced one. The unconstrained solution $\boldsymbol{z}_{r,0}$ represents the minimum control effort that re-centers the spacecraft in the nominal orbit. It is computed as:

$$\boldsymbol{z}_{r,0} = \boldsymbol{W}^{-1}\boldsymbol{p}, \tag{5.61}$$

which is considered feasible if it satisfies the tube constraint $\boldsymbol{b}^T\boldsymbol{z}_{r,0} \leq \beta$.

If the unconstrained solution violates the linearity tube constraint, the inequality becomes active at the optimum. In this case, the solution lies at the boundary of the admissible region. Exploiting the KKT stationarity condition:

$$2\boldsymbol{W}\boldsymbol{z} - 2\boldsymbol{p} + \nu\boldsymbol{b} = 0, \qquad \text{with} \qquad \nu \geq 0. \tag{5.62}$$

Solving for $\boldsymbol{z}$ yields the closed-form solution:

$$\boldsymbol{z}_{r,1} = \boldsymbol{W}^{-1}\boldsymbol{p} - \frac{1}{2}\nu\boldsymbol{W}^{-1}\boldsymbol{b}, \tag{5.63}$$

with ν obtained enforcing the feasibility condition:

$$\nu = \frac{2\left(\boldsymbol{b}^T\boldsymbol{W}^{-1}\boldsymbol{p} - \beta\right)}{\boldsymbol{b}^T\boldsymbol{W}^{-1}\boldsymbol{b}}. \tag{5.64}$$

The constrained candidate is feasible only if ν is non-negative.

The final choice between the feasible candidates, is based on the minimum value of the objective function $J_{\text{rec}}(\boldsymbol{z})$. Even here, if no feasible candidate is found, the unconstrained solution is the output, together with the non-feasibility flag.

5.3.4. Maneuver Scheduling

The recovery strategy is implemented through a sequence of impulsive maneuvers whose execution epochs are fixed a priori and selected according to dynamical considerations. Each recovery is composed by two burns, analytically obtained with the KKT problem.

The first burn is applied at the epoch corresponding to the deepest penetration point into the shadow region. At this instant, the deviation from the nominal trajectory reaches its maximum value, as required for the mitigation of the eclipse event. Acting at this point represents the optimal recovery condition, since the locally unstable dynamical environment would otherwise cause a further growth of the deviation. Delaying the control action would therefore require a significantly greater corrective effort, in terms of $\Delta \boldsymbol{v}$, to steer the spacecraft back to the reference orbit. The second burn is performed two days after the first one, a timing selected through a trial-and-error process. In particular, closely spaced corrective maneuvers are required to rapidly recover the nominal orbit and to prevent the growth of deviations along the unstable dynamical directions.

A second two-burn recovery maneuver is performed after the first one, since numerical analyses have shown that a single two-burn correction is generally insufficient to fully restore the reference trajectory. Relying on only one recovery action typically leads to residual deviations that require subsequent costly TPA station-keeping maneuvers and may ultimately result in divergence. For this reason, the recovery strategy is completed through an additional two-burn sequence, with the maneuvers again spaced by two days.

As can be appreciated in Fig. 5.3, in the range between the eclipse event and 8 days after it, the nominal station-keeping maneuvers are not performed (e.g. maneuver $k+1$) to ensure an effective recovery. After this period, the TPA schedule is restarted.

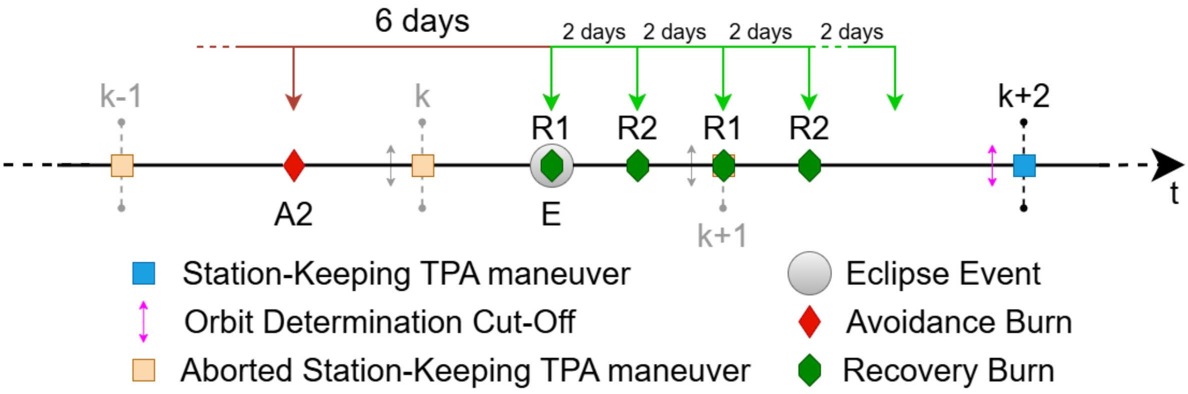

Figure 5.3: Recovery maneuvers schedule.

6 | Results

This chapter presents the results of the numerical simulations by applying the proposed eclipse avoidance and recovery strategy to different possible reference Quasi-Halo orbits for the LUMIO Mission. The analysis aims to assess the effectiveness of the methodology, giving a comprehensive overview of the proposed solution, together with trade-off considerations and statistical results.

The performance of the formulated approach is quantified in terms of eclipse mitigation capability, trajectory deviation control, and ΔV expenditure. Eventually, a statistical assessment based on Monte Carlo analyses is presented.

The Test Case 1 adopted for the simulation is the reference trajectory introduced in Sec. 2.3.2, analyzed throughout Chapter 4. Subsequently, the methodology is also applied to additional Quasi-Halo orbits (Test Case 2, 3) reported in Appendix A, which present different kinds of eclipse events, with different characteristics.

The purpose of this chapter is not to achieve global optimality, but to assess the practical effectiveness and robustness of the proposed strategy under realistic operational assumptions. All simulations are conducted consistently with the modeling assumptions introduced in the previous chapters.

6.1. Test Case 1: *01 Jan 2027 00:00:00 UTC*

The reference Quasi-Halo orbit considered in this section is the one introduced in Sec. 2.3.2. This case is presented first, as its dynamical and eclipse characteristics are well understood and have been extensively analyzed in the previous chapters. The trajectory is characterized by recurrent eclipse events with moderate duration, in particular, three Earth eclipses and one Moon eclipse over the mission lifetime. The duration of the eclipse events along the reference trajectory is reported in Fig. 4.6.

Before the execution of the station-keeping and eclipse-avoiding simulations, the shadow function and the linearity tube radius are computed, together with all the STMs required to apply the methodology of Chapter 5. These quantities depend solely on the nominal reference trajectory and can therefore be evaluated once and reused throughout the simulation campaign.

Figure 6.1 reports the time history of the shadow function margin $g(t) - g_{\text{safe}}$ for the eclipse events encountered along the reference trajectory. Negative values correspond to violation of the safety margin, with the depth of the curve providing a direct measure of the eclipse severity.

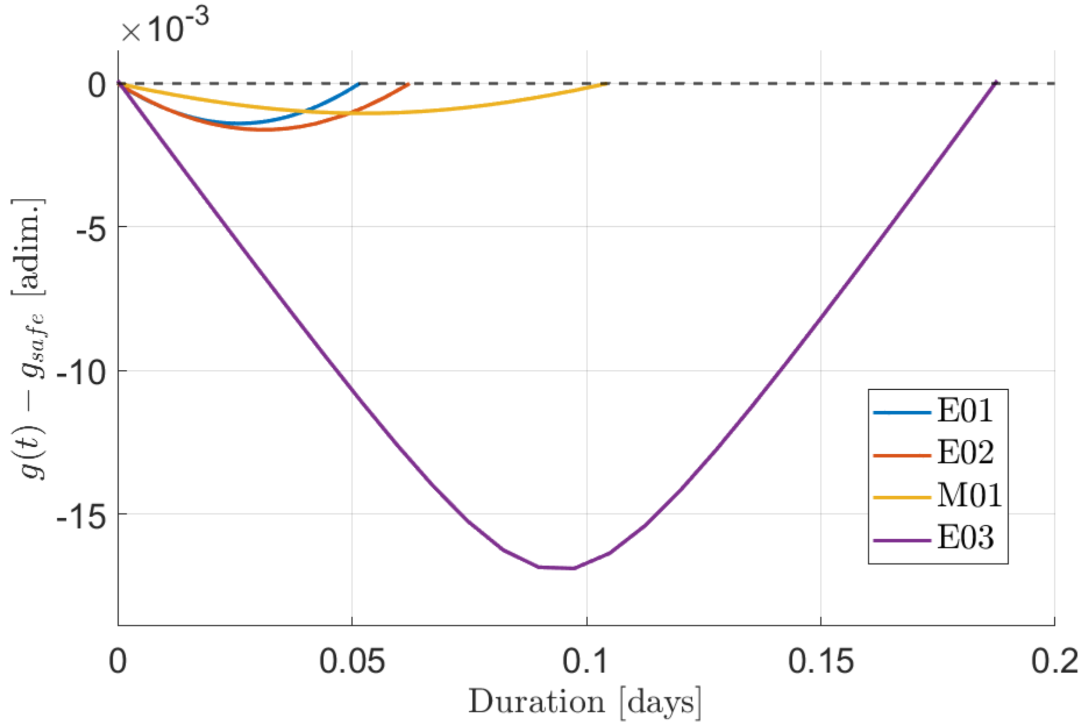

Figure 6.1: Values of the shadow function for Test Case 1.

Among the events, $E03$ is noticeably deeper and longer than the others, thus it is the most critical in terms of power depletion risk. On the other hand, events $E01$, $E02$ and $M01$ show shallower penetrations and shorter durations. This directly guides the selection of t_e for each eclipse event, which is chosen at the minimum of the corresponding curve, representing the most critical condition.

Figure 6.2 illustrates the growth of the linearization error associated to the STM propagation at the tube enforcement epoch t^* in the first recovery maneuver computation for $E01$. For each candidate radius, created as a logarithmic set between 10^{-6} and 10^{-3} in dimensionless units, the statistical analysis on the violation of the linearity is performed, and the 2σ error is considered.

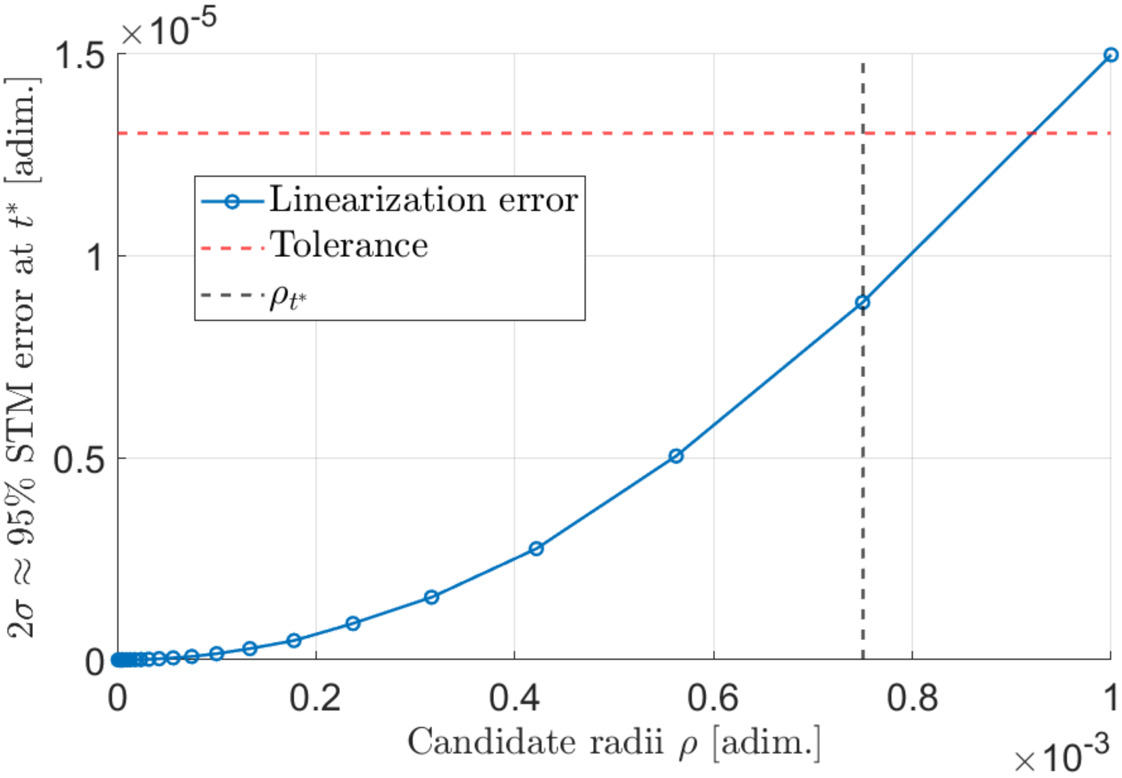

Figure 6.2: Linearity tube radius computation for the first recovery maneuver of Test Case 1.

As expected the STM error exhibits a monotonic and non-linear increase with the deviation amplitude. Beyond a certain threshold, the STM error grows and exceeds the prescribed tolerance of 1.3×10^{-5} in dimensionless units, which corresponds to almost 5 km. The maximum candidate radius under the tolerance line identifies the adopted radius for the linearity tube ρ_{t^*}, representing the largest deviation for which the linear dynamics can be safely exploited. Deviations beyond this bound would invalidate the linear approximation yielding ineffective subsequent TPA maneuvers.

Since four eclipse events are considered and two recovery maneuvers (each consisting of a double-burn) are planned for each event (see Fig. 5.3), a total of eight tube radii must be computed. Their values, for the Test Case 1, are reported in Table 6.1.

Radii	**E01**	**E02**	**M01**	**E03**
$\rho_{t^*,1}$ [adim.]	$7.498942 \cdot 10^{-4}$	$1.000000 \cdot 10^{-3}$	$1.778279 \cdot 10^{-4}$	$1.000000 \cdot 10^{-5}$
$\rho_{t^*,2}$ [adim.]	$1.000000 \cdot 10^{-3}$	$1.000000 \cdot 10^{-3}$	$1.000000 \cdot 10^{-3}$	$5.623413 \cdot 10^{-4}$

Table 6.1: Radii of the linearity tubes in each recovery maneuver for the Test Case 1.

The core outcomes of the proposed eclipse avoidance and recovery strategy are presented hereafter. The figures collectively illustrate how the introduction of the eclipse-avoidance strategy interacts with the nominal station-keeping policy and how these actions affect the trajectory deviation and the mitigation of shadow periods.

Figure 6.3 represents the time history of the corrective maneuvers. Outside eclipse seasons, the station keeping cost remains low, confirming the expected values of the TPA method. In contrast, during eclipse passages (red dashed lines), both the avoidance and recovery maneuvers lead to localized higher $\|\Delta \boldsymbol{v}\|$. The most demanding corrections occur at the last eclipse event, $E03$, as expected. This long and deep eclipse induces large deviations from the nominal trajectory, thus requiring more energetic recovery maneuvers.

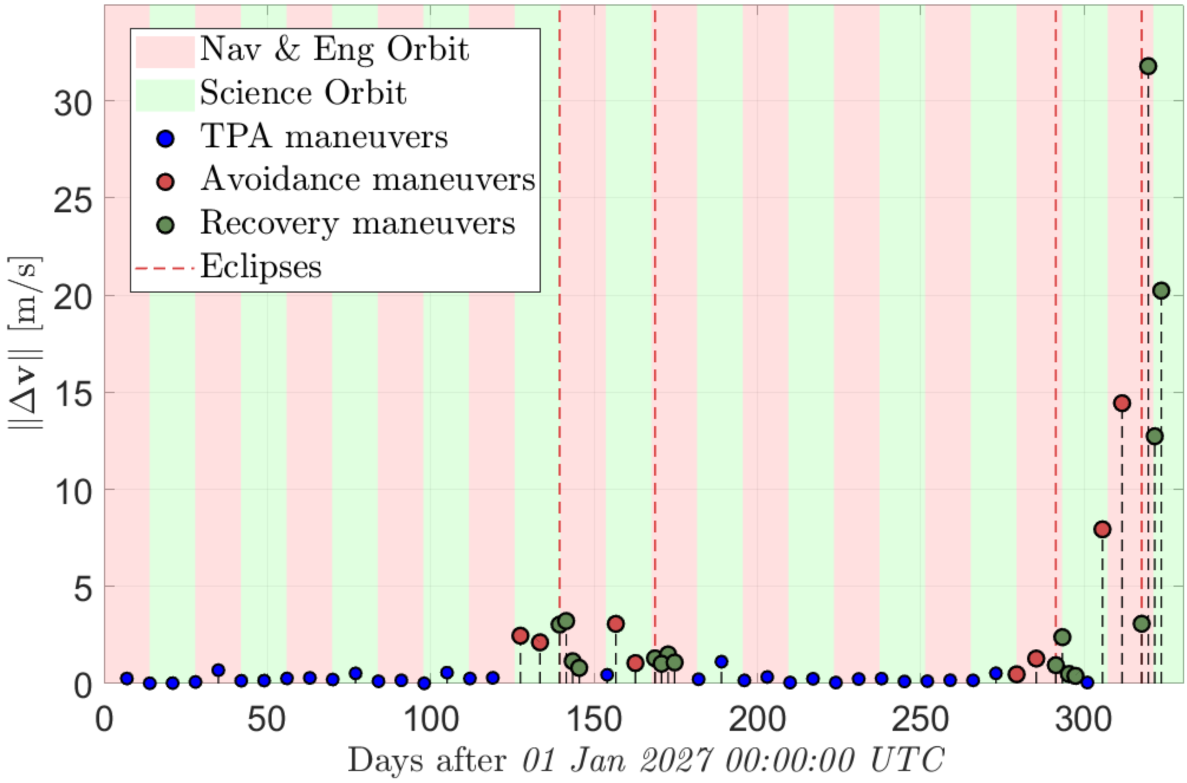

Figure 6.3: $\Delta \boldsymbol{v}$ magnitude of the maneuvers in Test Case 1.

Figure 6.4 shows the lighting conditions experienced along the simulated trajectory. The dashed contours represent the eclipse durations predicted on the reference trajectory, while the filled bars indicate the residual shadow exposure after the mitigation strategy. Early season eclipses are either significantly shortened or fully avoided, whereas the longest event is mitigated in such a way that the threshold withstood by the power requirements in Eq. (5.21) is not violated.

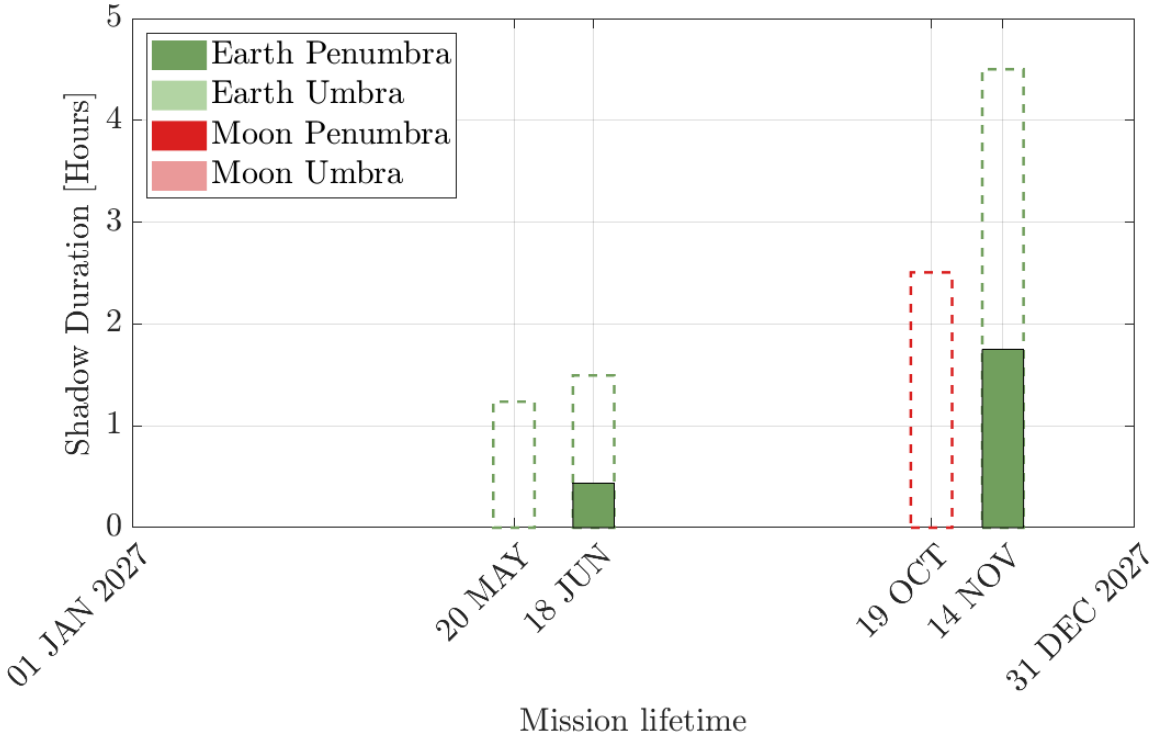

Figure 6.4: Lighting condition of LUMIO simulated trajectory 1.

Overall, the results confirm the effectiveness of the mitigation approach in substantially limiting the duration and severity of the event. In Fig. 6.5 close-up views of the shadow regions are presented. The deviation of several thousand kilometers justifies the magnitude of the avoidance and recovery maneuvers of the $E03$ eclipse event.

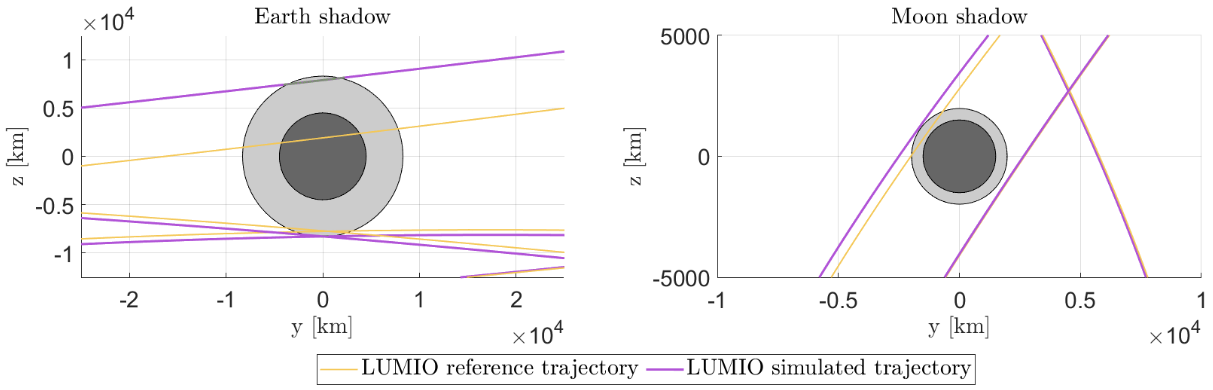

Figure 6.5: Resulting eclipses 1 close-up views @ ECSER (left) and @ MCSMR (right).

Figure 6.6 reports the time evolution of the position and velocity deviations with respect to the reference trajectory. Outside the eclipse intervals, the deviations remain bounded to very low levels, while, during eclipse events, localized increases in both position and velocity can be observed. This is the sought-after that mitigates eclipses: getting further from the nominal orbit and then steering back to it. The last event is extremely severe even in terms of state deviation, justifying the magnitude of the maneuvers.

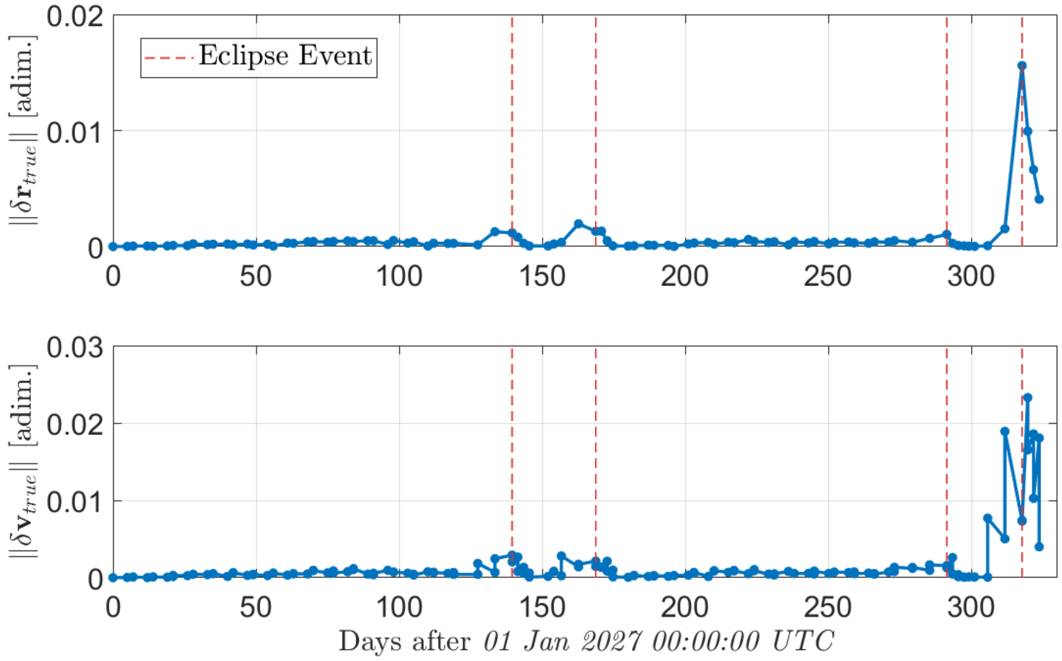

Figure 6.6: State deviation along the simulated trajectory of Test Case 1.

Table 6.2 summarizes the $\Delta \boldsymbol{v}$ budgets associated with avoidance and recovery maneuvers for each event, and the total values. The results are relative to one Monte Carlo run and are therefore subject to variability induced by the random errors in Table 4.1.

Event	$\mathbf{A}_1^{(1)}$ [m/s]	$\mathbf{A}_2^{(1)}$ [m/s]	$\mathbf{A}_{tot}$ [m/s]	$\mathbf{R}_{1+2}^{(1)}$ [m/s]	$\mathbf{R}_{1+2}^{(2)}$ [m/s]	$\mathbf{R}_{tot}$ [m/s]
E01	2.4644	2.1228	4.5873	6.2576	1.9566	8.2143
E02	3.0750	1.0552	4.1302	2.3216	2.5878	4.9094
M01	0.4780	1.2880	1.7660	3.3388	0.8934	4.2322
E03	7.9400	14.4349	22.3749	34.8652	32.9627	67.8279
Total:			**32.8584**			**85.1838**

Table 6.2: Magnitude of the avoidance and recovery maneuvers in Test Case 1. The letter $\boldsymbol{A}$ stands for avoidance burn, and $\boldsymbol{R}$ stands for recovery burn. The subscript refers to the burn of the maneuver, while the apex refers to the number of the maneuver.

The control effort is dominated by the last and most critical eclipse event which necessitates a large corrective action as a consequence of the intrinsically great deviation needed. On the other hand, the overall cost related to the nominal station-keeping TPA maneuvers of $\Delta v_{S/K} = 8.4116$ m/s remains low, comparable to the nominal case.

The overall cost $\Delta V_{tot} = \Delta v_{avoid} + \Delta v_{recovery} + \Delta v_{S/K} = 126.4539$ m/s exceeds the nominal value of LUMIO's ΔV budget. This is a direct consequence of the conservative design adopted in this analysis, which prioritizes robust avoidance, recovery, and strict containment of the state deviation. The resulting ΔV_{tot} should therefore be interpreted as an upper-bound estimate for an eventual trade-off analysis.

6.2. Test Case 2: *10 Jan 2027 00:00:00 UTC*

The reference Quasi-Halo considered in this section is the one reported in Appendix A.1. This time, the reference trajectory is characterized by only one Moon eclipse event. As a result, a lower overall control effort is expected with respect to Test Case 1, since the mitigation strategy is required to operate only on one Moon event, which is intrinsically easier to face due to the smaller deviations needed. Applying the same procedure and algorithm, the following results are obtained.

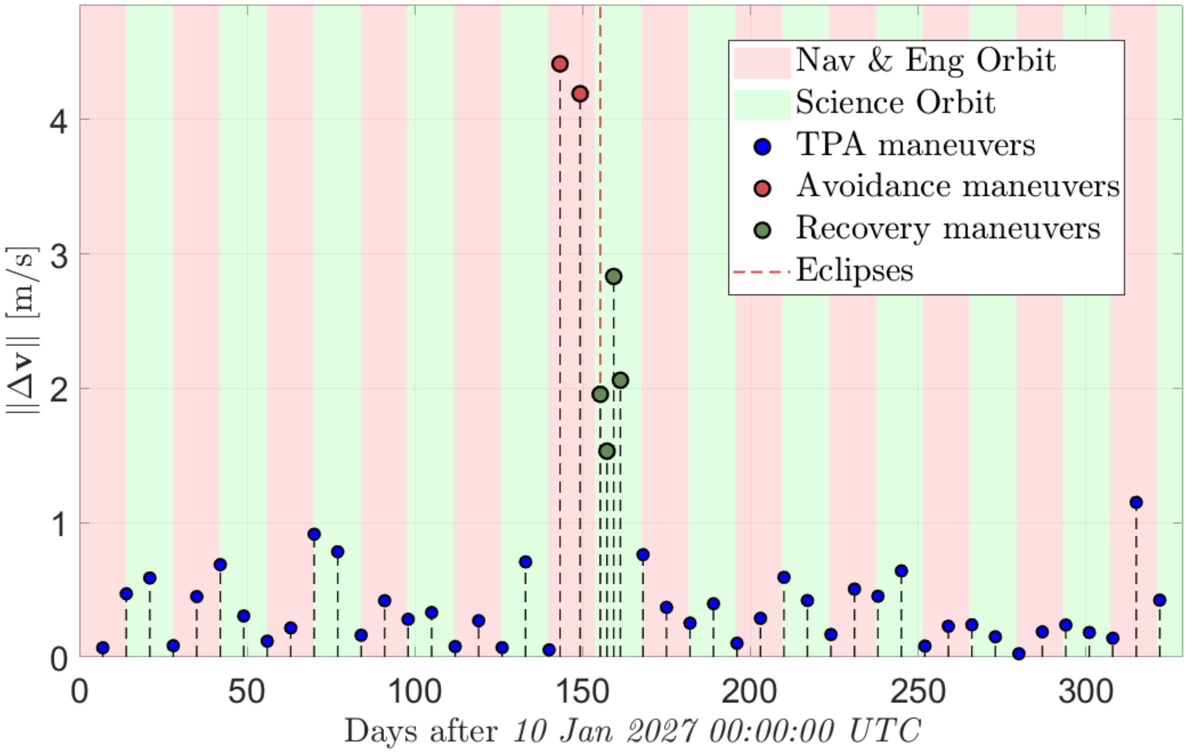

Figure 6.7: $\Delta \boldsymbol{v}$ magnitude of the maneuvers in Test Case 2.

Figure 6.7 confirms that the control effort is largely concentrated around the single Moon eclipse event. Outside the eclipse window, only small TPA maneuvers are performed, resulting in a substantially reduced overall ΔV_{tot} with respect to Test Case 1.

As can be seen from Fig. 6.8, in this case shadow regions are completely avoided, resulting in an eclipse-free operational Quasi-Halo for LUMIO. Drifting the satellite from the Moon's shadow is indeed easier because of the lower size of the shadow cones.

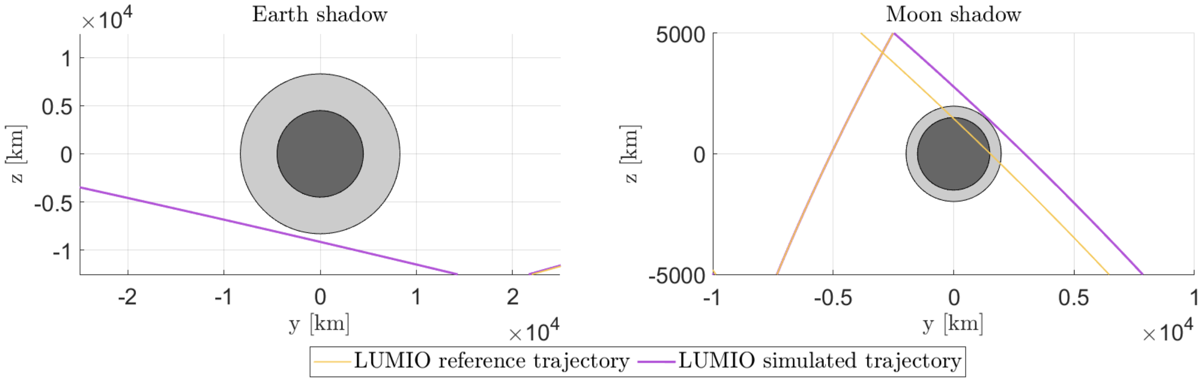

Figure 6.8: Resulting eclipses 2 close-up views @ ECSER (left) and @ MCSMR (right).

The desired localized increase in the state deviation is shown in Fig. 6.9, for the achievement of the eclipse avoidance.

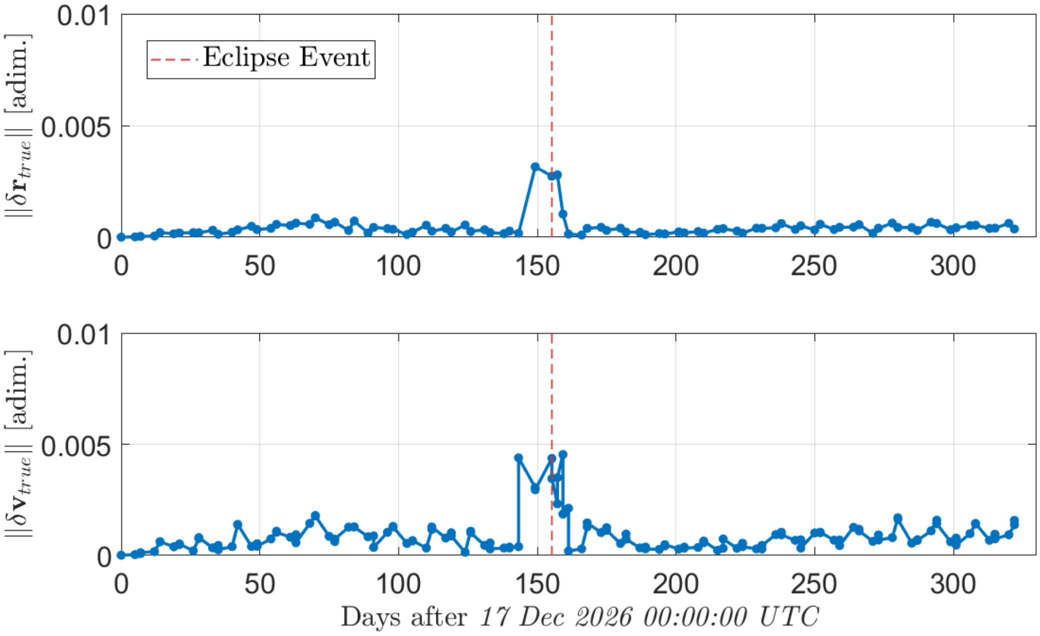

Figure 6.9: State deviation along the simulated trajectory of Test Case 2.

Table 6.3 resumes the values of the avoidance and recovery maneuvers for this case.

Event	$\mathbf{A}_1^{(1)}$ [m/s]	$\mathbf{A}_2^{(1)}$ [m/s]	$\mathbf{A}_{tot}$ [m/s]	$\mathbf{R}_{1+2}^{(1)}$ [m/s]	$\mathbf{R}_{1+2}^{(2)}$ [m/s]	$\mathbf{R}_{tot}$ [m/s]
M01	4.1169	3.9243	8.0412	3.1473	4.7712	7.9185
Total:			**8.0412**			**7.9185**

Table 6.3: Magnitude of the avoidance and recovery maneuvers in Test Case 2.

Considering the nominal $\Delta v_{S/K} = 14.9412$ m/s, again aligned with the nominal case, the overall cost $\Delta V_{tot} = 30.9009$ m/s remains dominated by the eclipse mitigation maneuvers. Compared to Test Case 1, complete avoidance of the eclipse is performed with a feasible expense, highlighting the problem of deep Earth eclipses.

6.3. Test Case 3: *17 Dec 2026 00:00:00 UTC*

The last test case is based on the Quasi-Halo trajectory reported in Appendix A.2. This case is characterized by one long Moon eclipse and one shorter Earth eclipse. As such, it represents an intermediate scenario between Test Case 1 and Test Case 2, providing a balanced trade-off between eclipse severity and overall control effort.

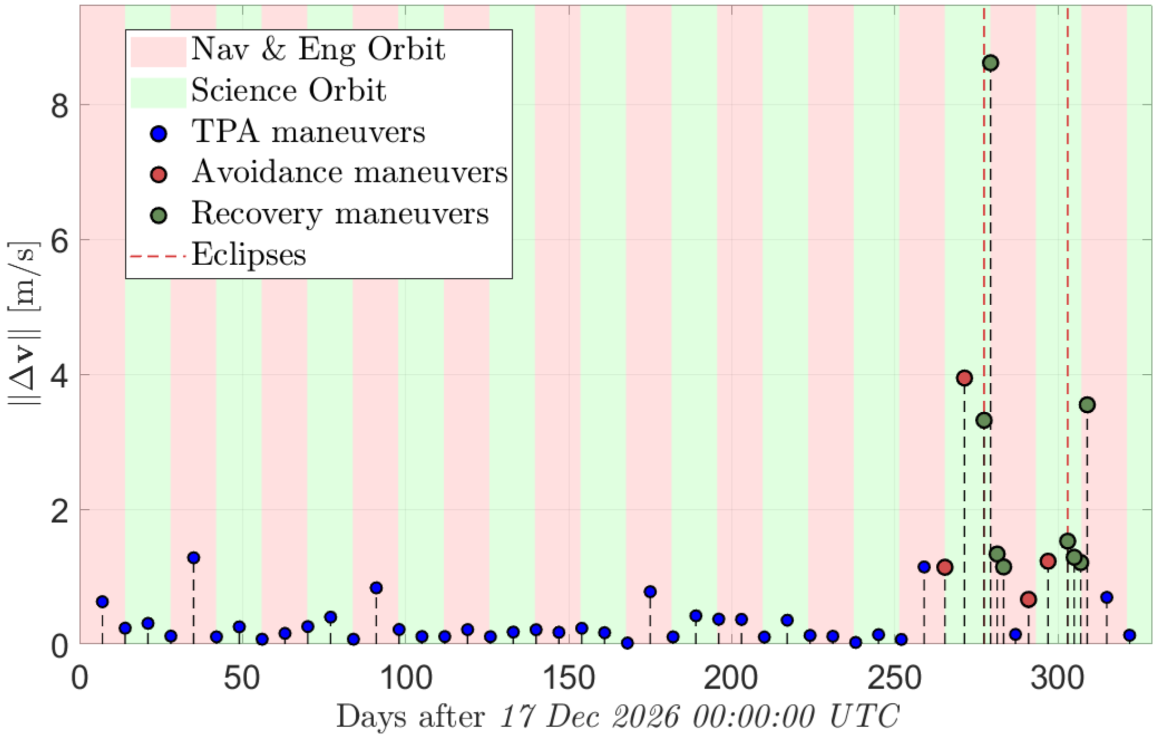

Figure 6.10: $\Delta \boldsymbol{v}$ magnitude of the maneuvers in Test Case 3.

As can be seen in Fig. 6.10, the maneuver profile of Test Case 3 reflects the combined effect of the lunar and terrestrial eclipse events, with localized peaks in $\|\Delta \boldsymbol{v}\|$ occurring in correspondence with the eclipse windows. As shown in Fig. 6.11, this allows the complete avoidance of umbra regions and the mitigation of the penumbra ones under the limit imposed by the power requirements, accomplishing the objective.

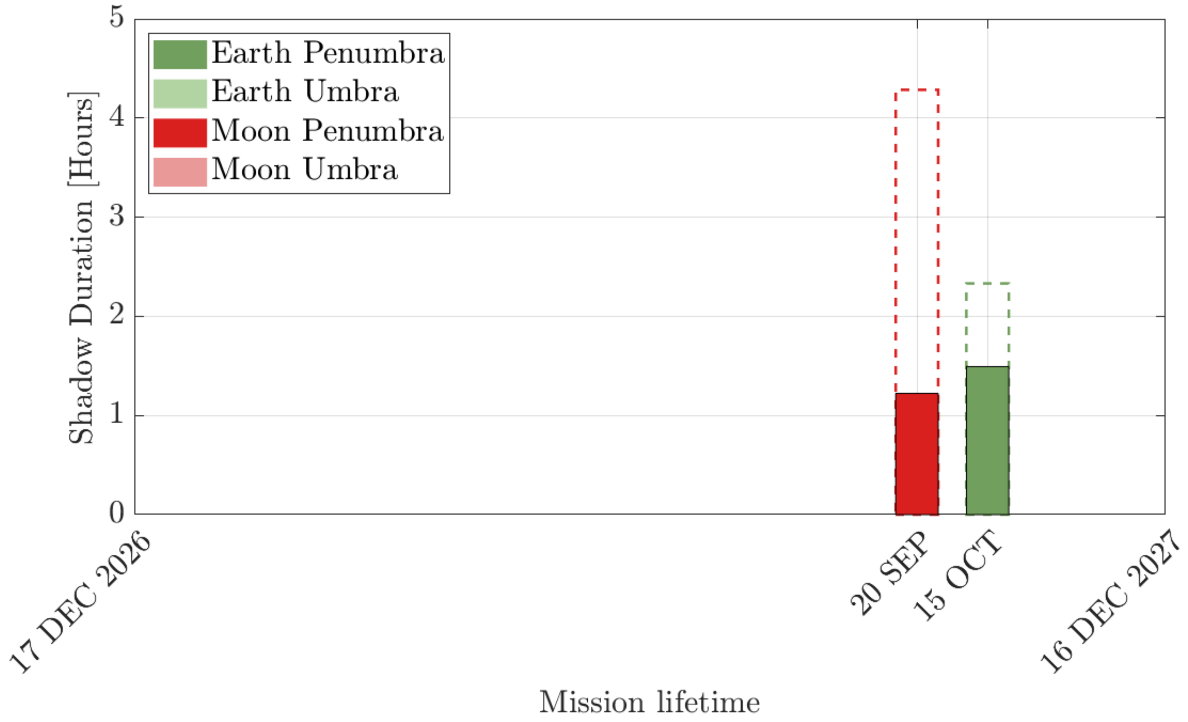

Figure 6.11: Lighting condition of LUMIO simulated trajectory 3.

The two intersections with the shadow cones can be appreciated in Fig. 6.12. Their almost-tangent behavior leads to manageable penumbra passages for LUMIO.

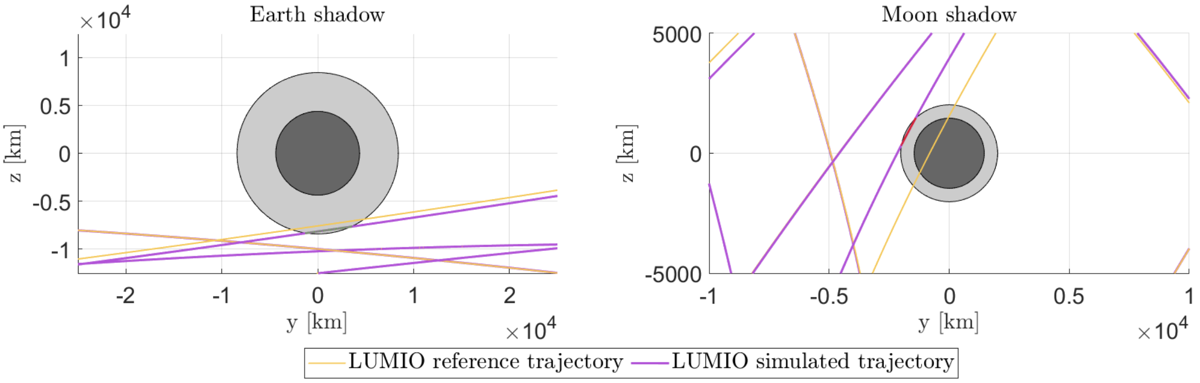

Figure 6.12: Resulting eclipses 3 close-up views @ ECSER (left) and @ MCSMR (right).

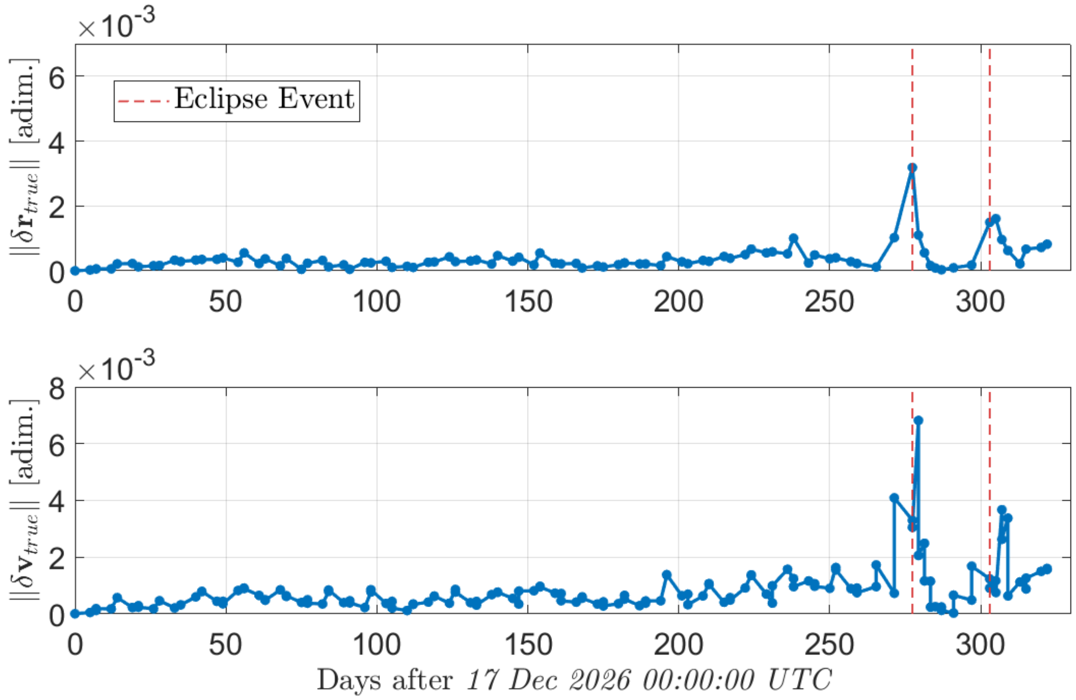

Figure 6.13: State deviation along the simulated trajectory of Test Case 3.

Small, localized increases in deviations are observed in correspondence with the eclipse events, while the state remains well bounded over the entire mission, confirming the moderate perturbation level of this trajectory.

Table 6.4 shows the expense related to the avoidance and recovery strategy.

Event	$\mathbf{A}_1^{(1)}$ [m/s]	$\mathbf{A}_2^{(1)}$ [m/s]	$\mathbf{A}_{tot}$ [m/s]	$\mathbf{R}_{1+2}^{(1)}$ [m/s]	$\mathbf{R}_{1+2}^{(2)}$ [m/s]	$\mathbf{R}_{tot}$ [m/s]
M01	1.1407	3.8406	4.9812	11.2261	2.6747	13.9008
E01	0.6606	1.2510	1.9115	2.9272	4.7549	7.6821
Total:			**6.8927**			**21.5829**

Table 6.4: Magnitude of the avoidance and recovery maneuvers in Test Case 3.

The station-keeping cost $\Delta v_{S/K} = 11.5232$ m/s cumulates to the avoidance and recovery ones, resulting in a total $\Delta V_{tot} = 39.9989$ m/s which guarantees operational feasibility of LUMIO. Overall, the expense remains within a manageable range, despite the presence of large maneuvers.

6.4. Monte Carlo Analysis

In order to asses the robustness of the proposed eclipse avoidance and recovery strategy, a Monte Carlo analysis is conducted for each test case. For each reference trajectory, 1000 samples are generated to account for uncertainties in the Orbit Injection (OI), Orbit Determination (OD) and in the maneuver execution (Table 4.1), allowing a statistical evaluation of the resulting ΔV_{tot} expense. This analysis provides insight into the dispersion of the system response and counts the failed simulated trajectories.

For each test case, the required parameters that depend only on the reference trajectory are computed a priori. Then, the Monte Carlo loop is iterated in a parallel fashion guaranteeing computational efficiency. The results are shown in the following table.

Test Case	μ [m/s]	σ [m/s]	3σ value [m/s]	fails [%]
1	125.5736	3.7955	136.2553	0
2	32.1684	2.9359	41.0219	0
3	41.9428	4.0183	58.5653	0.8

Table 6.5: Monte Carlo analysis results.

For the analyzed test cases the total control effort remains bounded with limited dispersion along the samples. The near absence of failures indicates that the mitigation strategy consistently satisfies the imposed constraints under the considered uncertainties, supporting the robustness of the methodology at a statistical level.

7 Conclusions

This final chapter provides a summary of the research carried out in this work together with final thoughts on the method's applicability.

The thesis addressed the problem of eclipse management for CubeSats operating on Quasi-Halo orbits in the cislunar environment, with specific application to LUMIO Mission. Given the intrinsic instability of libration point dynamics and the critical power limitations of CubeSats, eclipse events represent a severe operational constraint that must be faced to ensure the right illumination conditions. The main objective of this work was to investigate whether eclipse avoidance requirements can be integrated into station-keeping strategies preserving compatibility, robustness and limited fuel expenditure.

To this aim, a constraint-based analytical framework was developed to actively mitigate eclipse events without relying on global optimization techniques. The proposed methodology formulates eclipse avoidance and recovery maneuvers as linearized control problems solved through the Karush-Kuhn-Tucker (KKT) conditions. This approach enables deterministic closed-form solutions, which are well suited for this scenario due to their computational efficiency.

Firstly, a continuous and differentiable shadow function was introduced to quantify the spacecraft proximity to the shadow regions generated by the two primaries, the Earth and the Moon. The function provides a scalar margin that allows eclipse avoidance to be enforced as hard constraint within the KKT framework. Moreover, validation through the SPICE `gfoclt` function demonstrated excellent agreement in eclipse detection, confirming the accuracy of the geometric model.

Eclipse avoidance maneuvers were designed as two-impulse corrections applied before each detected eclipse event. The enforcement of the eclipse constraint at the deepest penetration point proved to be a conservative and effective strategy. Numerical results showed that it is possible to deviate from the reference trajectory to successfully prevent the shadow regions. However, this comes with a non-negligible cost.

Eclipse avoidance inevitably introduces deviations: thus, a recovery strategy is needed to steer back the satellite to nominal orbit. This requirement is expressed through a linearity tube constraint, ensuring that the subsequent station-keeping maneuvers based on the Target Point Approach (TPA) remain valid under the linearized dynamics. Recovery maneuvers, also formulated within the KKT framework, effectively re-center the trajectory. However, even in this case, this comes with a relatively high cost.

The numerical simulations demonstrated that, for the LUMIO Mission, the proposed strategy is effective in terms of eclipse avoidance and recovery. On the other hand, the propellant expense to achieve such maneuvers is typically higher than the available one. This is particularly evident for long and deep Earth eclipses (as in Test Case 1), which define the worst case scenarios. Indeed, the high deviations needed to avoid the shadow region affect both the avoidance maneuvers and the recovery ones, demanding large burns to accomplish the objective. The strategy behaved better when dealing with Moon eclipses and short Earth eclipses, as highlighted by Test Case 2 and 3. The critical eclipses were avoided with a limited and reasonable expense, which could become a valid argument for an eventual trade-off analysis. Monte Carlo analyses further confirmed the robustness of the approach with almost null failure percentage.

Overall, concerning LUMIO Mission, this work shows that the active eclipse avoidance technique developed is effective and robust within the high-fidelity dynamics employed. In particular, it can be considered a valid method to avoid short Earth eclipses and all types of Moon eclipses. Instead, when it comes to deep and long Earth eclipses, the response of the strategy is still robust but the propellant cost becomes too demanding.

The generality with which this technique has been formulated, allows other CubeSat missions to test and assess to which point an active, linearized, closed form, KKT-based, station-keeping compatible, and computationally-efficient avoidance/recovery technique can be employed to overcome the critical power requirements that affect them.

7.1. Future Developments

The problem addressed in this work concerns a mission scenario that is still only partially explored in the current literature. As CubeSats are progressively extending their operational domain beyond low-Earth orbit, the need for an efficient, deterministic and fuel-aware station-keeping strategy that embed eclipse avoidance becomes clear. The methodology formulated represents a step toward the mitigation of this problem with an active (maneuver-based) approach.

The possible future developments ideas in this direction are:

- **Linearity tube constraint formulation**: The offline Monte Carlo analysis performed in this work to define it, can be improved with a deeper analytical and numerical investigation on the relationship between local dynamical properties and non-linear effects.
- **Exploitation of stable and unstable invariant manifolds**: Rather than counteracting the natural dynamics, future strategies could leverage unstable directions to efficiently move the spacecraft away from the shadow regions, and subsequently exploit stable manifolds to steer back toward the previous reference trajectory with a significantly reduced ΔV expense.
- **Relaxing the requirement to return to the original reference trajectory**: Instead of enforcing recovery toward the same Quasi-Halo orbit, the spacecraft could be transferred to another, nearby, Quasi-Halo that is not affected by the eclipse event at that epoch. By allowing controlled transitions between reference trajectories of the same family, it may be possible to avoid eclipses without incurring in high-cost maneuvers.

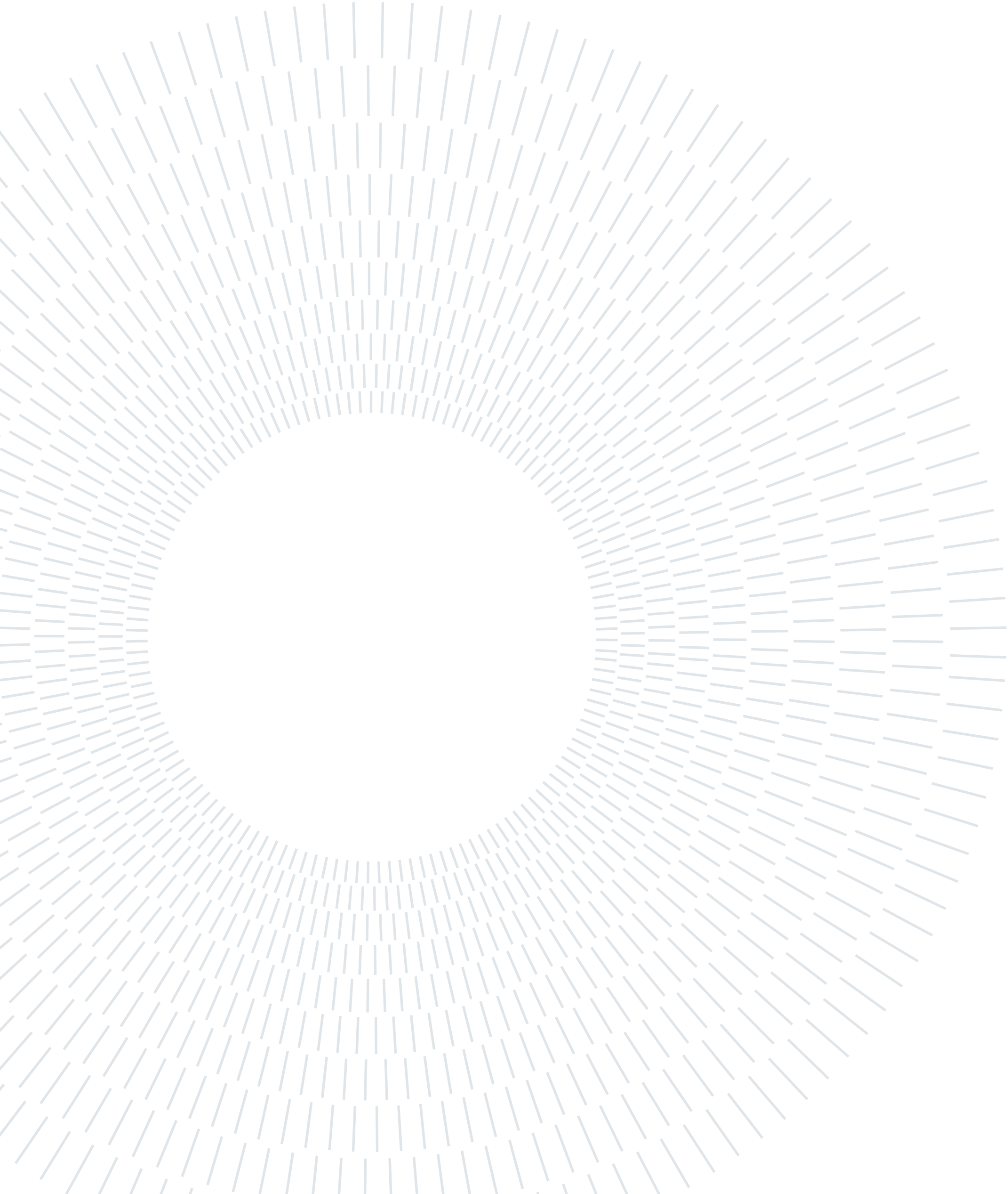

Bibliography

[1] R. R. Bate, D. D. Mueller, and J. E. White. *Fundamentals of Astrodynamics*. Dover Publications, 1971.

[2] J. T. Betts. *Practical Methods for Optimal Control and Estimation Using Nonlinear Programming*. SIAM, 2010.

[3] M. J. Boliger. Cislunar mission design: Transfers linking near rectilinear halo orbits and the butterfly family.

[4] C. Bottiglieri, F. Piccolo, C. Giordano, F. Ferrari, and F. Topputo. Applied trajectory design for cubesat close-proximity operations around asteroids: The Milani case. *Aerospace*, May 2023. doi: 10.3390/aerospace10050464.

[5] J. V. Breakwell. Investigation of halo satellite orbit control. Technical Report TR CR-132858, NASA, 1973.

[6] J. V. Breakwell, A. A. Kamel, and M. J. Ratner. Station-keeping for a translunar communication station. *Celestial Mechanics*, 10(3):357–373, 1974. doi: 10.1007/BF01586864.

[7] R. H. Byrd, J. C. Gilbert, and J. Nocedal. A trust region method based on interior point techniques for nonlinear programming. *Mathematical Programming*, 89(1):149–185, 2000.

[8] J. Cheetham et al. Capstone mission: Cislunar navigation and operations in a near-rectilinear halo orbit. *Acta Astronautica*, 2023.

[9] T. Chikazawa, N. Baresi, S. Campagnola, N. Ozaki, and Y. Kawakatsu. Minimizing eclipses via synodic resonant orbits with applications to EQUULEUS and MMX. Jan. 2021.

[10] A. M. Cipriano, D. A. Dei Tos, and F. Topputo. Orbit design for LUMIO: The lunar meteoroid impacts observer. *Frontiers in Astronomy and Space Sciences*, Sept. 2018. doi: 10.3389/fspas.2018.00029.

[11] A. Costa. Eclipse-free quasi-halo orbits design with applications to the LUMIO mission, 2024.

[12] S. Cravedi. Orbit maintenance strategy for libration point orbits, July 2019.

[13] G. H. Darwin. Periodic orbits. *Acta Mathematica*, 21(1):99–242, 1897.

[14] D. C. Davis, F. S. Khoury, K. C. Howell, and D. J. Sweeney. Phase control and eclipse avoidance in near rectilinear halo orbits. 2020. AAS Paper 20-047.

[15] D. A. Dei Tos and N. Baresi. Genetic optimization for the orbit maintenance of libration point orbits with applications to EQUULEUS and LUMIO. *AIAA SciTech Forum*, Jan. 2020. doi: 10.2514/6.2020-0466.

[16] D. A. Dei Tos and F. Topputo. On the advantages of exploiting the hierarchical structure of astrodynamical models. *Acta Astronautica*, Feb. 2017. doi: 10.1016/j.actaastro.2017.02.025.

[17] D. A. Dei Tos and F. Topputo. Trajectory refinement of three-body orbits in the real solar system model. *Advances in Space Research*, Feb. 2017. doi: 10.1016/j.asr.2017.01.039.

[18] D. A. Dei Tos and F. Topputo. High-fidelity trajectory optimization with application to saddle-point transfers. *Journal of Guidance, Control, and Dynamics*, June 2019. doi: 10.2514/1.G003838.

[19] L. Euler. *Theoria Motuum Lunae Nova Methodo Pertractata*, volume 22. Springer Science & Business Media, 1772.

[20] R. W. Farquhar. Far libration point of mercury. *Astronautics and Aeronautics*, 5(8), 1967.

[21] R. W. Farquhar. Station-keeping in the vicinity of collinear libration points with an application to a lunar communications problem. In *Space Flight Mechanics Specialist Symposium*, volume 11, pages 519–535, New York, 1967. American Astronautical Society.

[22] R. W. Farquhar. The control and use of libration-point satellites. Technical Report TR R-346, NASA, 1970.

[23] R. W. Farquhar. The utilization of halo orbits in advanced lunar operations. Technical Report X-551-70-449, NASA, 1970.

[24] R. W. Farquhar. Limit-cycle analysis of a controlled libration-point satellite. *Journal of the Astronautical Sciences*, 17:267–291, 1970.

[25] R. W. Farquhar. Comments on optimal controls for out-of-plane motion about the translunar libration point. *Journal of Spacecraft and Rockets*, 8(7):815–816, 1971. doi: 10.2514/3.59728.

[26] R. W. Farquhar, D. P. Muhonen, C. R. Newman, and H. S. Heuberger. The first libration-point satellite mission: Overview and flight history. In *AAS/AIAA Astrodynamics Specialist Conference*, number AAS Paper 79-126, Provincetown, MA, 1979. American Astronautical Society.

[27] D. Freesland, S. Napora, E. Harvie, C. Wheeler, and A. Krimchansky. Autonomous maneuver planning and execution for GeoXO station keeping and momentum management. 2023. AAS Paper 23-082.

[28] K. M. Getzandanner, K. E. Berry, P. G. Antreasian, J. M. Leonard, C. D. Adam, and D. R. Wibben. Small-body proximity operations and TAG: Navigation experiences and lessons learned from the OSIRIS-REx mission. 2021.

[29] C. Giordano and F. Topputo. Analysis, design, and optimization of robust trajectories in cislunar environment for limited-capability spacecraft. *Journal of the Astronautical Sciences*, Nov. 2023. doi: 10.1007/s40295-023-00413-8.

[30] C. Giordano and F. Topputo. Target-based guidance method for trajectories with multiple flybys. Sept. 2025.

[31] G. Gómez, K. C. Howell, J. J. Masdemont, and C. Simó. Station-keeping strategies for translunar libration point orbits. Jan. 1998.

[32] S. C. Gordon. Comparison of station-keeping algorithms for an interior libration point orbit in the sun–earth+moon elliptic restricted three-body problem. Technical Report USAFA-TR-91-13, United States Air Force Academy, Colorado Springs, CO, 1991.

[33] D. Guzzetti, E. M. Zimovan, K. C. Howell, and D. C. Davis. Stationkeeping analysis for spacecraft in lunar near rectilinear halo orbits. 2017. AAS Paper 17-395.

[34] G. W. Hill. Researches in the lunar theory. *American Journal of Mathematics*, 1(1): 5–26, 1878.

[35] K. C. Howell and S. C. Gordon. Orbit determination error analysis and a station-keeping strategy for sun–earth l_1 libration point orbits. *Journal of the Astronautical Sciences*, 42(2):207–228, 1994.

[36] K. C. Howell and H. J. Pernicka. Station-keeping method for libration point tra-

jectories. *Journal of Guidance, Control, and Dynamics*, 16(1):151–159, 1993. doi: 10.2514/3.11440.

[37] M. N. Ismail, A. Bakry, H. H. Selim, and M. H. Shehata. Eclipse intervals for satellites in circular orbit under the effects of earth's oblateness and solar radiation pressure. *NRIAG Journal of Astronomy and Geophysics*, 4(1):117–122, 2015. doi: 10.1016/j.nrjag.2015.06.001.

[38] C. G. J. Jacobi. Sur le mouvement d'un point et sur un cas particulier du problème des trois corps. *Comptes Rendus*, 3:59–61, 1836.

[39] T. M. Keeter. Station-keeping strategies for libration point orbits: Target point and Floquet modes approaches, Aug. 1994.

[40] A. Klesh and J. Krajewski. Marco: Early operations of the first deep-space cubesats. *Acta Astronautica*, 159:332–343, 2019.

[41] A. Y. Kogan. An optimal program of impulse corrections of unstable periodic orbits. *Kosmicheskie Issledovaniya*, 30(5):712–714, 1992. In Russian.

[42] W. S. Koon, M. W. Lo, J. E. Marsden, and S. D. Ross. *Dynamical Systems, the Three-Body Problem and Space Mission Design.* Springer, New York, 2006. ISBN 978-0387209711.

[43] J.-L. Lagrange. Essai sur le problème des trois corps. *Prix de l'Académie Royale des Sciences de Paris*, 9:292, 1772.

[44] M. Lara and J. Peláez. On the numerical continuation of periodic orbits: An intrinsic, 3-dimensional, differential, predictor-corrector algorithm. *Astronomy & Astrophysics*, 389:692–701, 2002. doi: 10.1051/0004-6361:20020598.

[45] A. Martinelli, C. Giordano, and F. Topputo. Deterministic and stochastic optimization of station-keeping policies for libration-point orbits.

[46] N. Michelotti, A. Rizza, C. Giordano, and F. Topputo. Comparison of uncertainty propagation techniques in small-body environment. Aug. 2024.

[47] T. A. Pavlak. Mission design applications in the earth–moon system: Transfer trajectories and station-keeping, May 2010.

[48] H. Poincaré. Sur le problème des trois corps et les équations de la dynamique. *Acta Mathematica*, 13(1):A3–A270, 1890.

[49] Y. Shang, C. Wen, Y. Sun, H. Zhang, and Y. Gao. Active solar eclipse avoidance on

the distant retrograde orbit of the earth–moon system. *Advances in Space Research*, Nov. 2024. doi: 10.1016/j.asr.2024.11.027.

[50] Y. Shimane, K. Ho, and A. Weiss. Optimization-based phase-constrained station-keeping control on libration point orbit. 2024. AAS Paper 24-499.

[51] M. Shirobokov, S. Trofimov, and M. Ovchinnikov. Survey of station-keeping techniques for libration point orbits. *Journal of Guidance, Control, and Dynamics*, May 2017. doi: 10.2514/1.G001850.

[52] C. Simó, G. Gómez, J. Llibre, and R. Martínez. Station keeping of a quasiperiodic halo orbit using invariant manifolds. In *Second International Symposium on Spacecraft Flight Dynamics*, pages 65–70. European Space Agency, 1986.

[53] C. Simó, G. Gómez, J. Llibre, R. Martínez, and J. Rodríguez. On the optimal station keeping control of halo orbits. *Acta Astronautica*, 15(6):391–397, 1987. doi: 10.1016/0094-5765(87)90175-5.

[54] V. K. Srivastava, S. M. Yadav, B. N. Ramakrishna, et al. Earth conical shadow modeling for LEO satellite using reference frame transformation technique: A comparative study with existing earth conical shadow models. Oct. 2014.

[55] Y. Sun, M. Wang, and H. Zhang. Distant retrograde orbit baseline generation considering solar eclipse mitigation. June 2024.

[56] V. Szebehely. *Theory of Orbits: The Restricted Problem of Three Bodies*. Academic Press, 1967.

[57] Y. Tang, W. Wu, D. Qiao, and X. Li. Effect of orbital shadow at an Earth–Moon lagrange point on relay communication mission. Nov. 2017.

[58] F. Topputo. Three-body problem, Mar. 2018. Lecture slides.

[59] F. Topputo and the LUMIO Team. Phase B design of LUMIO: A Lunar CubeSat Mission at Earth–Moon L2. In *ASI CubeSat Workshop*, Rome, Italy, July 2024. Presentation given at the ASI CubeSat Workshop, 2–4 July 2024.

[60] F. Topputo and C. Zhang. Survey of direct transcription for low-thrust space trajectory optimization with applications. *Mathematical Problems in Engineering*, June 2014. doi: 10.1155/2014/851720.

[61] F. Topputo, C. Giordano, A. Martinelli, C. Buonagura, G. Merisio, F. Piccolo, A. Rizza, and P. Panicucci. LUMIO Phase B Mission Analysis Report (MAR). Nov. 2023.

[62] D. Villegas-Pinto, N. Baresi, S. Locoche, and D. Hestroffer. Resonant quasi-periodic near-rectilinear halo orbits in the elliptic–circular earth–moon–sun problem. Aug. 2022.

[63] W. Wiesel and W. Shelton. Modal control of an unstable periodic orbit. *Journal of the Astronautical Sciences*, 31:63–76, 1983.

[64] S. Wishnek et al. Eclipse-free three-body periodic orbits in cislunar space. 2022.

[65] B. Ye, X. Zhang, Y. Ding, and Y. Meng. Eclipse avoidance in TianQin orbit selection. Feb. 2021.

[66] Y. Yin, Y. Sun, and H. Zhang. Eclipse mitigation maneuver strategy for earth–moon 3:2 resonant orbits. Oct. 2024.

[67] W. Yu and K. Richon. Libration orbit eclipse avoidance maneuver study for the James Webb Space Telescope mission. 2020.

[68] F. Zanellati. Station-keeping strategies for libration point orbits with applications to the LUMIO mission, 2022.

[69] E. M. Zimovan, K. C. Howell, and D. C. Davis. Near rectilinear halo orbits and their application in cis-lunar space. 2019. IAA-AAS-DyCoSS3-125.

A | Appendix A

For the sake of completeness and generality, this Appendix presents additional Quasi-Halo orbit solutions beyond the one discussed in the main body of the thesis. For each trajectory, the associated eclipse events are identified. Furthermore, the correctness and consistency of the eclipse detection methodology are validated by cross-checking with the results of SPICE `gfoclt` function. The same procedure of Sec. 2.3.2 is performed with different starting epochs in order to find other Quasi-Halos and, with the procedure of Sec. 4.2.3, eclipse events are detected and validated. In the following sections the results are reported.

A.1. Starting Epoch: *10 Jan 2027 00:00:00 UTC*

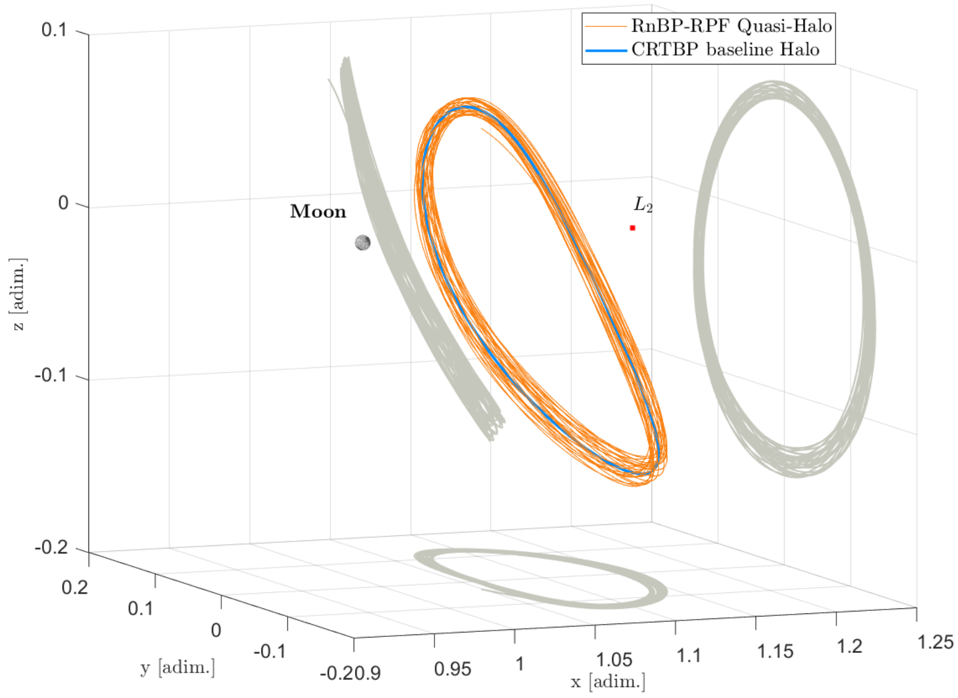

Figure A.1: LUMIO Quasi-Halo orbit 2 @ EMB centered adimensional rotating frame. Solution obtained from the baseline Halo orbit in CRTBP in blue.

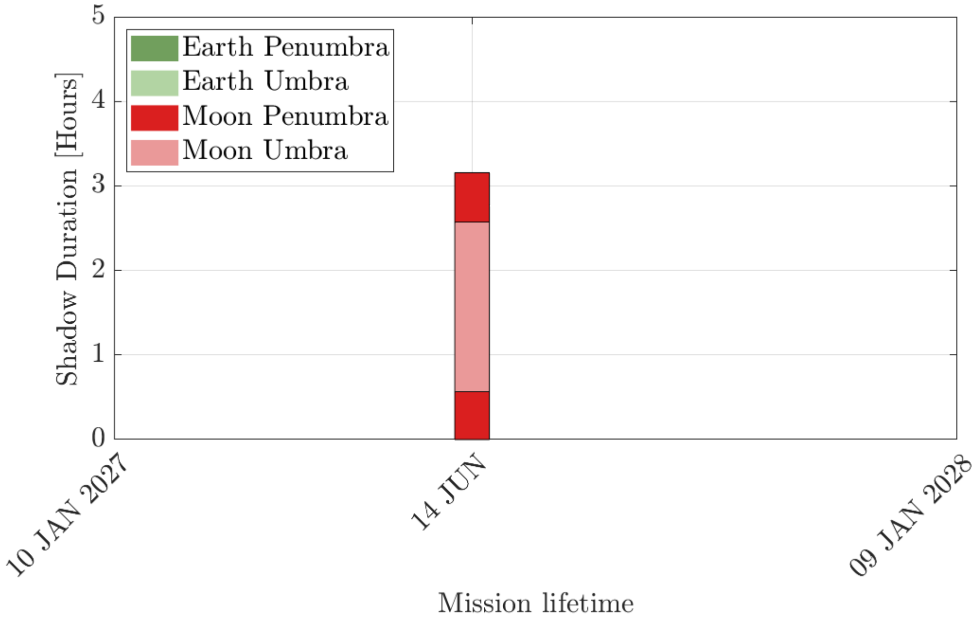

Figure A.2: Lighting condition of LUMIO Quasi-Halo reference trajectory 2.

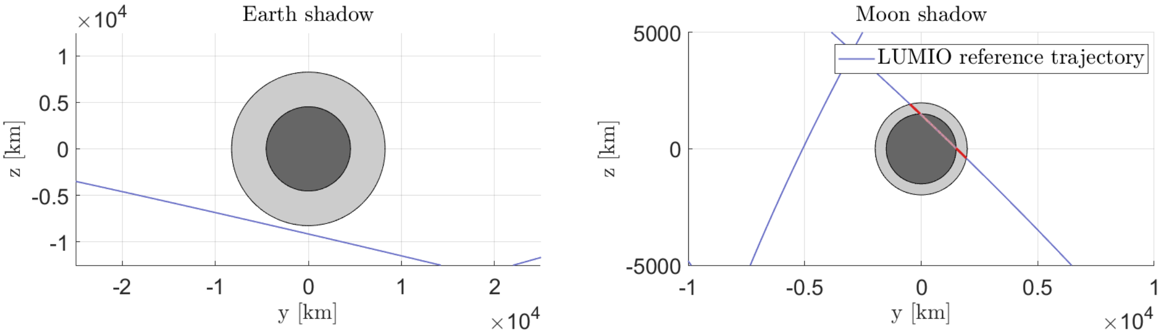

Figure A.3: Eclipses 2 close-up views @ ECSER (left) and @ MCSMR (right).

Event	**Start (UTC)**	**End (UTC)**	Δt_{start} [s]	Δt_{end} [s]	Δt_{dur} [s]	Δt_{dur} [%]
M01.cs	Jun 14 04:42:10	Jun 14 07:51:37	–	–	–	–
M01	Jun 14 04:42:11	Jun 14 07:51:35	$+1$	-2	-3	-0.03

Table A.1: Comparison between SPICE `gfoclt` and ECSER/MCSMR–based eclipse detections (penumbra–umbra combined) Quasi-Halo 2.

A.2. Starting Epoch: *17 Dec 2026 00:00:00 UTC*

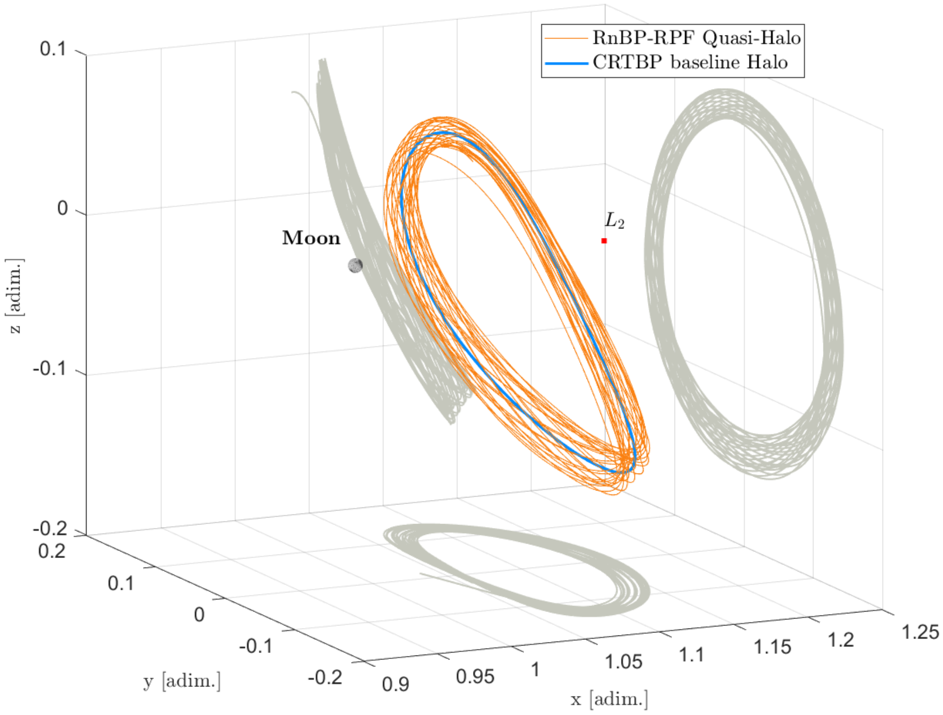

Figure A.4: LUMIO Quasi-Halo orbit 3 @ EMB centered adimensional rotating frame. Solution obtained from the baseline Halo orbit in CRTBP in blue.

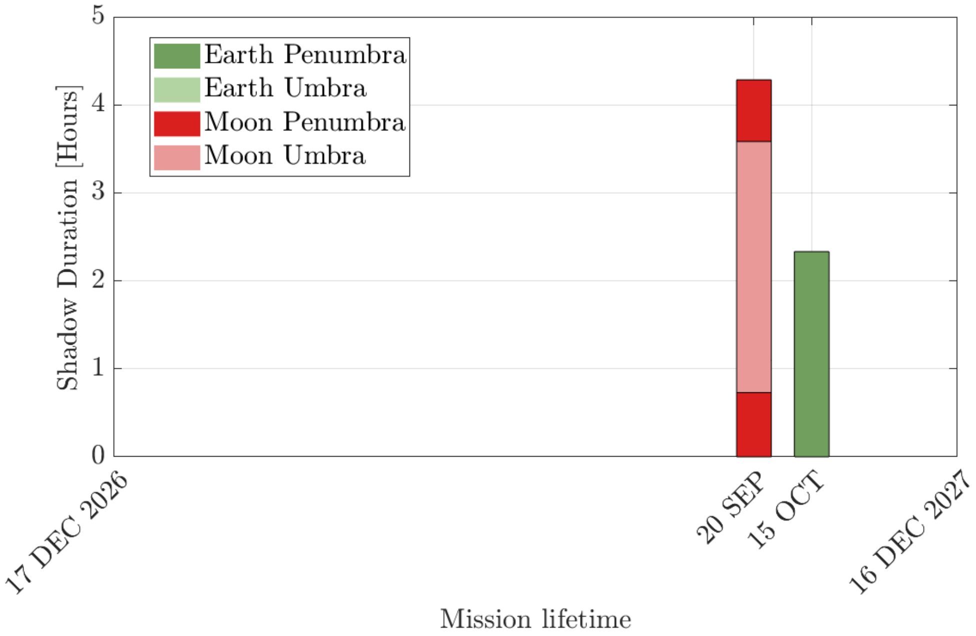

Figure A.5: Lighting condition of LUMIO Quasi-Halo reference trajectory 3.

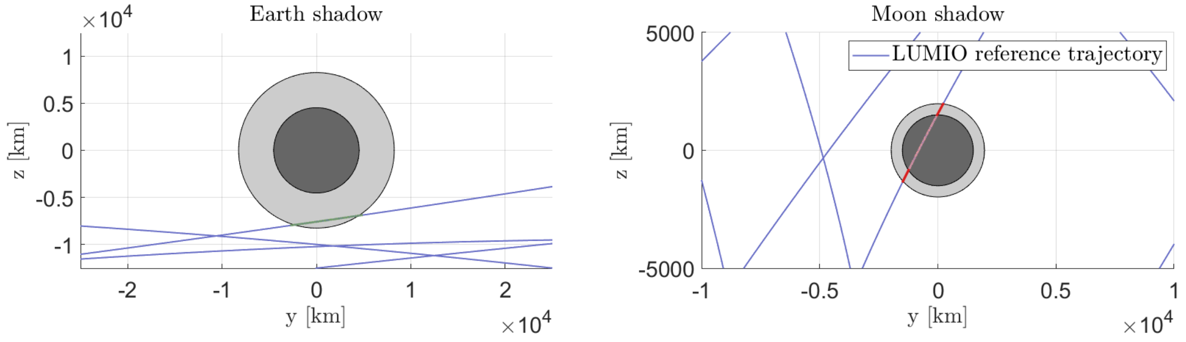

Figure A.6: Eclipses 3 close-up views @ ECSER (left) and @ MCSMR (right).

Event	**Start (UTC)**	**End (UTC)**	Δt_{start} [s]	Δt_{end} [s]	Δt_{dur} [s]	Δt_{dur} [%]
M01.cs	Sep 20 06:40:46	Sep 20 10:57:58	–	–	–	–
M01	Sep 20 06:40:47	Sep 20 10:57:57	$+1$	-1	-2	-0.01
E01.cs	Oct 15 22:54:02	Oct 16 01:13:28	–	–	–	–
E01	Oct 15 22:53:30	Oct 16 01:13:24	-32	-4	$+28$	$+0.33$

Table A.2: Comparison between SPICE `gfoclt` and ECSER/MCSMR–based eclipse detections (penumbra–umbra combined) Quasi-Halo 3.

B | Appendix B

The spacecraft state is initially defined in the EMB centered adimensional rotating frame, associated with the CRTBP. Let the adimensional state vector be:

$$\boldsymbol{x}_{\mathrm{EMB}} = \begin{bmatrix} \boldsymbol{r}_{\mathrm{EMB}} \\ \boldsymbol{v}_{\mathrm{EMB}} \end{bmatrix}, \qquad \boldsymbol{r}_{\mathrm{EMB}}, \boldsymbol{v}_{\mathrm{EMB}} \in \mathbb{R}^3. \tag{B.1}$$

Scaling to physical units

The adimensional coordinates are first converted into physical units using the characteristic distance unit $DU = 3.84405 \times 10^5$ km and time unit $TU = 4.34256461$ days:

$$\boldsymbol{r}^{\mathrm{km}}_{\mathrm{EMB}} = DU\, \boldsymbol{r}_{\mathrm{EMB}}, \qquad \boldsymbol{v}^{\mathrm{km/s}}_{\mathrm{EMB}} = \frac{DU}{TU \cdot 86400}\, \boldsymbol{v}_{\mathrm{EMB}}. \tag{B.2}$$

EMB to inertial (J2000) transformation

The EMB centered adimensional rotating frame is defined by the instantaneous Earth–Moon geometry. Its axes are constructed as:

$$\hat{\boldsymbol{x}}_{\mathrm{EMB}} = \frac{\boldsymbol{r}_M - \boldsymbol{r}_E}{\|\boldsymbol{r}_M - \boldsymbol{r}_E\|}, \tag{B.3}$$

$$\hat{\boldsymbol{z}}_{\mathrm{EMB}} = \frac{(\boldsymbol{r}_M - \boldsymbol{r}_E) \times (\boldsymbol{v}_M - \boldsymbol{v}_E)}{\|(\boldsymbol{r}_M - \boldsymbol{r}_E) \times (\boldsymbol{v}_M - \boldsymbol{v}_E)\|}, \tag{B.4}$$

$$\hat{\boldsymbol{y}}_{\mathrm{EMB}} = \hat{\boldsymbol{z}}_{\mathrm{EMB}} \times \hat{\boldsymbol{x}}_{\mathrm{EMB}}. \tag{B.5}$$

The rotation matrix from the EMB frame to the inertial J2000 frame is then defined:

$$\mathbf{R}_{\mathrm{EMB}\to\mathrm{IN}} = \begin{bmatrix} \hat{\boldsymbol{x}}_{\mathrm{EMB}} & \hat{\boldsymbol{y}}_{\mathrm{EMB}} & \hat{\boldsymbol{z}}_{\mathrm{EMB}} \end{bmatrix}. \tag{B.6}$$

The angular velocity of the EMB frame is given:

$$\omega_{EM} = \frac{\|\boldsymbol{h}_{EM}\|}{\|\boldsymbol{r}_{ME}\|^2}, \qquad \boldsymbol{h}_{EM} = \boldsymbol{r}_{ME} \times \boldsymbol{v}_{ME}, \tag{B.7}$$

where $\boldsymbol{r}_{ME} = \boldsymbol{r}_M - \boldsymbol{r}_E$. The angular velocity vector expressed in the inertial frame is

$$\boldsymbol{\omega}_{\text{EMB}}^{\text{IN}} = \mathbf{R}_{\text{EMB}\to\text{IN}} \begin{bmatrix} 0 \\ 0 \\ \omega_{\text{EM}} \end{bmatrix}. \tag{B.8}$$

The inertial position and velocity of the spacecraft are therefore obtained as

$$\boldsymbol{r}_{\text{IN}} = \boldsymbol{r}_{\text{IN}}^{\text{barycenter}} + \mathbf{R}_{\text{EMB}\to\text{IN}}\, \boldsymbol{r}_{\text{EMB}}^{\text{km}}, \tag{B.9}$$

$$\boldsymbol{v}_{\text{IN}} = \boldsymbol{v}_{\text{IN}}^{\text{barycenter}} + \mathbf{R}_{\text{EMB}\to\text{IN}}\, \boldsymbol{v}_{\text{EMB}}^{\text{km/s}} + \boldsymbol{\omega}_{\text{EMB}}^{\text{IN}} \times \mathbf{R}_{\text{EMB}\to\text{IN}}\, \boldsymbol{r}_{\text{EMB}}^{\text{km}}. \tag{B.10}$$

Earth-centered Sun–Earth rotating frame (ECSER)

The Earth-centered Sun–Earth rotating frame (ECSER) is defined by aligning its axes with the instantaneous Sun–Earth direction:

$$\hat{\boldsymbol{x}}_{\text{ECSER}} = \frac{\boldsymbol{r}_E - \boldsymbol{r}_S}{\|\boldsymbol{r}_E - \boldsymbol{r}_S\|}, \tag{B.11}$$

$$\hat{\boldsymbol{z}}_{\text{ECSER}} = \frac{(\boldsymbol{r}_E - \boldsymbol{r}_S) \times (\boldsymbol{v}_E - \boldsymbol{v}_S)}{\|(\boldsymbol{r}_E - \boldsymbol{r}_S) \times (\boldsymbol{v}_E - \boldsymbol{v}_S)\|}, \tag{B.12}$$

$$\hat{\boldsymbol{y}}_{\text{ECSER}} = \hat{\boldsymbol{z}}_{\text{ECSER}} \times \hat{\boldsymbol{x}}_{\text{ECSER}}. \tag{B.13}$$

The rotation matrix from the inertial J2000 frame to the ECSER frame is then defined:

$$\mathbf{R}_{\text{IN}\to\text{ECSER}} = \begin{bmatrix} \hat{\boldsymbol{x}}_{\text{ECSER}} & \hat{\boldsymbol{y}}_{\text{ECSER}} & \hat{\boldsymbol{z}}_{\text{ECSER}} \end{bmatrix}. \tag{B.14}$$

The spacecraft position expressed in ECSER coordinates is then:

$$\boldsymbol{r}_{\text{ECSER}} = \mathbf{R}_{\text{ECI}\to\text{ECSER}} \left(\boldsymbol{r}_{\text{IN}} - \boldsymbol{r}_E \right). \tag{B.15}$$

Moon-centered Sun–Moon rotating frame (MCSMR)

Analogously, the Moon-centered Sun–Moon rotating frame (MCSMR) is defined as

$$\hat{\boldsymbol{x}}_{\text{MCSMR}} = \frac{\boldsymbol{r}_M - \boldsymbol{r}_S}{\|\boldsymbol{r}_M - \boldsymbol{r}_S\|}, \tag{B.16}$$

$$\hat{\boldsymbol{z}}_{\text{MCSMR}} = \frac{(\boldsymbol{r}_M - \boldsymbol{r}_S) \times (\boldsymbol{v}_M - \boldsymbol{v}_S)}{\|(\boldsymbol{r}_M - \boldsymbol{r}_S) \times (\boldsymbol{v}_M - \boldsymbol{v}_S)\|}, \tag{B.17}$$

$$\hat{\boldsymbol{y}}_{\text{MCSMR}} = \hat{\boldsymbol{z}}_{\text{MCSMR}} \times \hat{\boldsymbol{x}}_{\text{MCSMR}}. \tag{B.18}$$

The rotation matrix from the inertial J2000 frame to the MCSMR frame is then defined:

$$\mathbf{R}_{\text{IN}\rightarrow\text{MCSMR}} = \begin{bmatrix} \hat{\boldsymbol{x}}_{\text{MCSMR}} & \hat{\boldsymbol{y}}_{\text{MCSMR}} & \hat{\boldsymbol{z}}_{\text{MCSMR}} \end{bmatrix}. \tag{B.19}$$

The spacecraft position expressed in the Moon-centered rotating frame is

$$\boldsymbol{r}_{\text{MCSMR}} = \mathbf{R}_{\text{ECI}\rightarrow\text{MCSMR}} \left(\boldsymbol{r}_{\text{IN}} - \boldsymbol{r}_{M} \right). \tag{B.20}$$

These transformations allow the spacecraft trajectory to be consistently expressed in the rotating frames required for eclipse geometry evaluation.

All the positions and velocities of the celestial bodies are recovered through ephemeris data from SPICE toolkit.

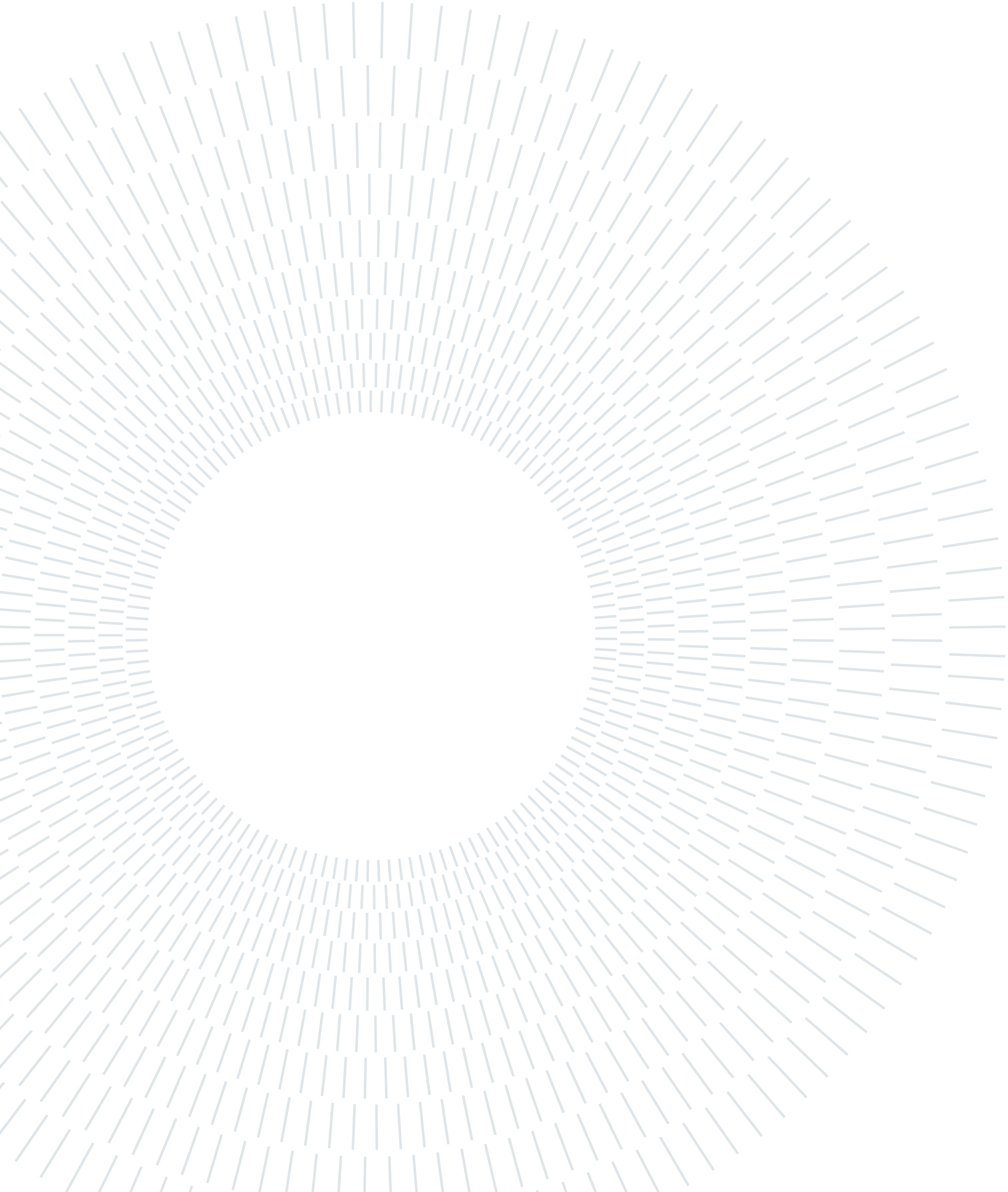

Ringraziamenti

Vorrei ringraziare il Prof. Francesco Topputo per aver supervisionato il mio lavoro, Dott. Carmine Giordano e Alessandro Martinelli per avermi seguito e aiutato nello svolgimento della tesi con professionalità, gentilezza e serenità.

Questa tesi segna la conclusione di un percorso che non avrei mai immaginato di intraprendere, iniziato senza aspettative e forse con la sola intenzione di provarci, per non avere rimpianti. Col tempo si è rivelata la scelta migliore che potessi fare: anni intensi, fatti di gioia e fatica, risate e sudore. Sono stati cinque anni in cui ho imparato ad apprezzare Milano, una città che disorienta e mette alla prova, ma che proprio nello smarrimento aiuta a fare chiarezza. È lì che emerge ciò che sei davvero, insieme alle persone giuste, e dove, alla fine, ci si sente a casa. Ringrazio quindi, Dario, Manu, Cri, Nickmill, Matte, Da, Anna, Thias, La Fra, Adri, Rkomiii, Jemmee. Un grazie speciale a Maxito, abbiamo portato up il TRTN22, non potevo desiderare coinquilino migliore. Chi prima e chi dopo, avete reso questi anni indimenticabili.

Così come non dimenticherò mai Siviglia. Ho rimandato per anni l'idea di partire per l'Erasmus, spaventato da dover uscire ulteriormente dalla comfort zone. Ho preso l'ultimo treno disponibile, e per fortuna l'ho fatto. Se questi cinque anni sono stati bellissimi, i cinque mesi in Spagna sono stati la ciliegina sulla torta. L'esperienza più bella della mia vita, una crescita personale che mi ha profondamente cambiato. Ringrazio le persone fantastiche con cui ho condiviso questa avventura in particolare, Antea, Manuelito, Reda, Ele, Ale, Andre grande e piccolo, Luca, Cate, Chiara.

Tutto questo non sarebbe comunque stato lo stesso se non fosse per i miei amici di sempre. Sapere di trovarvi in valle ad aspettarmi ogni volta che sarei tornato mi ha fatto apprezzare ogni minuto di ritardo di Trenord. Siamo cresciuti insieme e nonstante le strade quasi tutte diverse che abbiamo preso siamo sempre rimasti uniti, nei momenti belli e soprattutto in quelli di difficoltà. Sono sicuro che la nostra amicizia non sarà mai messa in dubbio da niente e nessuno. Ringrazio Lollo, Marta, Jaki, Betta, Fa, Merk, Garna. Con voi a sostenermi tutto è possibile.

Un grazie immenso non può che andare a ogni componente della mia grande famiglia. Ognuno di voi, in modi diversi, mi ha reso la persona che sono oggi. Ringrazio mio papà Fabio, mi hai insegnato che il duro lavoro viene sempre ripagato e che, a questo mondo, nessuno regala niente. Ringrazio mia mamma Isa, per l'amore giornaliero che mi hai sempre dimostrato. Ringrazio i miei fratelli Sofi, Simo, Pie: il vostro costante impegno nel sopportarmi nei momenti più stressanti dimostra quanto mi vogliate bene. Ringrazio il nonno Biagio: non poter condividere questo traguardo anche con te mi spezza il cuore; grazie per avermi trasmesso la tua infinita voglia di imparare, la porterò sempre con me. Ringrazio i nonni Rinaldo, Agnese e Alda: il grande tifo che avete sempre fatto per me è stato fondamentale. Ringrazio Luca per avermi supportato e per essersi sempre interessato a me e al mio percorso in questi cinque anni.

Antea, ti ho conosciuta tra le strade sevillane in un momento in cui la mia vita sembrava in stallo. Mi hai insegnato a sorridere di nuovo, e mi hai riempito il cuore essendo semplicemente te stessa. Grazie per avermi sostenuto in quei momenti in cui manco io credevo in me stesso. La distanza non sarà per sempre.

Infine voglio ringraziare Giovanni: il bambino che ha sognato, il ragazzo che ha sempre dato il meglio di sé, e l'uomo che è diventato.

Grazie.